공학박사학위논문

Additive Development for Extreme Bottom-up Filling of Through Silicon Via: from Inorganic Halide Leveler to Synthesized Additive Containing Quaternary Ammonium Cations and Naphthalene Ring for Single Additive System

실리콘 관통 전극(TSV)의 상향식 급속 충전을 위한 첨가제 개발:
무기 할라이드 평탄제에서부터 나프탈렌 고리와 4차 암모늄을 포함한
단일 첨가제 시스템 용 합성 첨가제에 이르기까지

2020년 8월

서울대학교 대학원
화학생물공학부
성 민 재

Additive Development for Extreme Bottom-up Filling of Through Silicon Via: from Inorganic Halide Leveler to Synthesized Additive Containing Quaternary Ammonium and Naphthalene Ring for Single Additive System

실리콘 관통 전극(TSV)의 상향식 급속 충전을 위한 첨가제 개발: 무기 할라이드 평탄제에서부터 나프탈렌 고리와 4 차 암모늄을 포함한 단일 첨가제 시스템용 합성 첨가제에 이르기까지

지도교수 김 재 정

이 논문을 공학박사 학위논문으로 제출함
2020 년 7 월

서울대학교 대학원
화학생물공학부
성 민 재

성민재의 공학박사 학위논문을 인준함
2020 년 7 월

위 원 장 김 영 규 (인)
부위원장 김 재 정 (인)
위 원 이 규 태 (인)
위 원 김 수 길 (인)
위 원 임 터 호 (인)

Abstract

Through silicon via (TSV) is one of the most important technologies in 3-dimensional wafer/chip stacking. In this study, TSVs with 60 μm deep and 5 μm in diameter were sufficiently filled without defects using various levelers, inorganic halide ions and synthesized leveler containing quaternary ammonium cations and naphthalene ring, and their filling mechanism was investigated. The working mechanism of the iodide ions in TSV filling was systemically identified by electrochemical measurements; It was found that the formation of CuI on the electrode surface is a key process for inhibiting Cu ion reduction. This inhibition effect of the iodide ions enables defect-free TSV filling. Furthermore, we achieved a defect-free TSV filling with enlarged Cu grains using a two-step filling method that effectively promotes the direct reduction of the Cu ions rather than electrochemical reduction of CuI.

However, it was found that the iodide ions considerably decreased the efficiency of Cu electrodeposition because of the formation of an unstable CuI suppression layer on top of the wafer. The CuI layer easily detached from the wafer, and

additional electrons were consumed to reestablish the suppression layer during gap-filling. The bromide ions were introduced as an alternative to the iodide ions. Although the suppression strength of bromide ions to Cu electrodeposition is weaker than that of iodide ions, bromide ions form a more stable suppression layer that does not reduce the efficiency of Cu electrodeposition, enabling high-speed TSVs filling. As a result, the filling rate with bromide ions was twice as fast as that with iodide ions at the same applied current density; thereby TSVs were completely filled in 500 s.

We also tried to perform the TSV filling in single-additive condition using synthesized organic leveler. We synthesized a polyethylene-glycol-based organic leveler having quaternary ammonium cations linked to a naphthalene ring at both ends. This leveler enabled a bottom-up TSV filling in a single-additive system. The uniformity of TSV filling was highly dependent on the chain length of the leveler controlled by the molecular weight of polyethylene glycol. The electrochemical investigation of the leveler revealed that the chain length was

related to the rate of re-adsorption during Cu electrodeposition, which is critical in TSV filling. At the optimal chain length, the uniform and defect-free bottom-up TSV filling was successfully achieved. TSV filling time was also reduced by up to 500 s.

Keywords: through-silicon-via (TSV), Cu, electrodeposition, leveler, inorganic halide levelers, synthesized leveler, single additive system, superfilling

Student number: 2015-22833

Content

List of Tables

List of Figures

CHAPTER I

Introduction

1.1. Recent trend for Cu interconnection

The Cu interconnect has been used in the semiconductor integrated circuits (ICs), introduced by IBM in 1997.[1] Microprocessors with Cu, which has lower resistivity (1.67 μΩ·cm) than bulk Al (2.66 μΩ·cm), induce faster operating speed compared to the chips composed of Al, the standard material before the Cu interconnect. Moreover, high resistance to electromigration of the Cu interconnects accelerates the replacement of Al interconnect, increasing the reliability.[2-5] Compared to Al, the Cu interconnect is fabricated by specific process, Damascene process, due to its physical properties as shown in Fig. 1.1. The process consists of dielectric deposition, patterning of dielectric, formation of barrier and seed layer, fabrication of interconnection by Cu electrodeposition, and finally planarization of the deposited Cu. For enhancing the higher performance of the interconnect, signal transmission rate should be improved, and the rate can be increased by stacking metal layer. Ultra-large-scale integration based Cu metal is achieved by repeating the process. The dimensions of Cu wires and devices

keep on decreasing to densified chips of fast operation speed and less active power. Recently, 10 nm metallization with 13 layer was fabricated by Intel as shown in Fig. 1.2,[6] and the roadmap for devices and system is shown in Fig. 1.3.[7] The device technology will continue to increase degree of integration to improve the chip performance.[8-12] However, the scaling approaches technological limitation: difficulties in patterning, insufficient area for the deposition of barrier and seed layer, and problems in metallization. As shown in Fig. 1.3., International Roadmap for Devices and Systems (IRDS) reported that it would become impossible to reduce the dimensions of device features due to its scale.[7] On these reasons, the 3D integration has been focused in order to improve the device performance, solving the scaling problem. A critical element of 3D integration is the fabrication of through silicon vias (TSVs) passing through a silicon wafer for the vertical stacking of multiple dies in shown Fig. 1.4. TSVs enable the miniaturization of integrated multi-chip systems as well as improve electrical performance, because of their short connections. Therefore, various techniques have been investigated to form defect-free TSV.

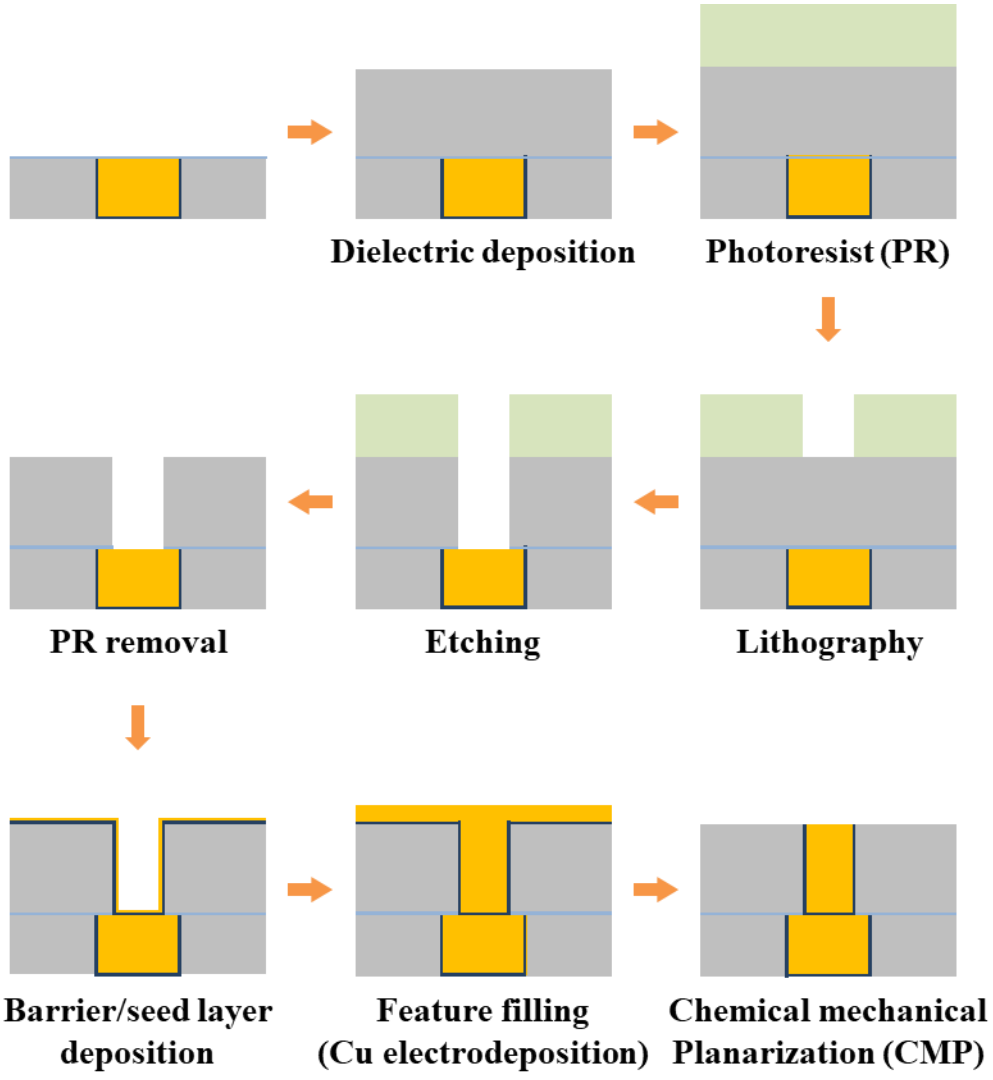

Figure 1.1. Schematic diagram of damascene process.

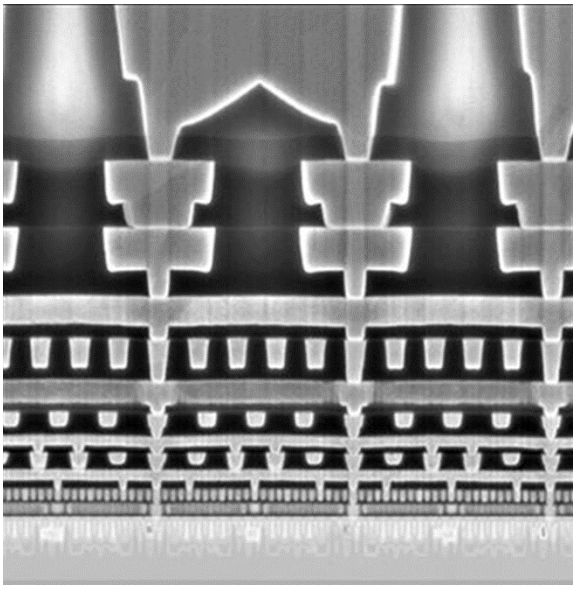

Figure 1.2. Cross-section image of 13-layer metal lines in Intel's CPU (Ref. 6).

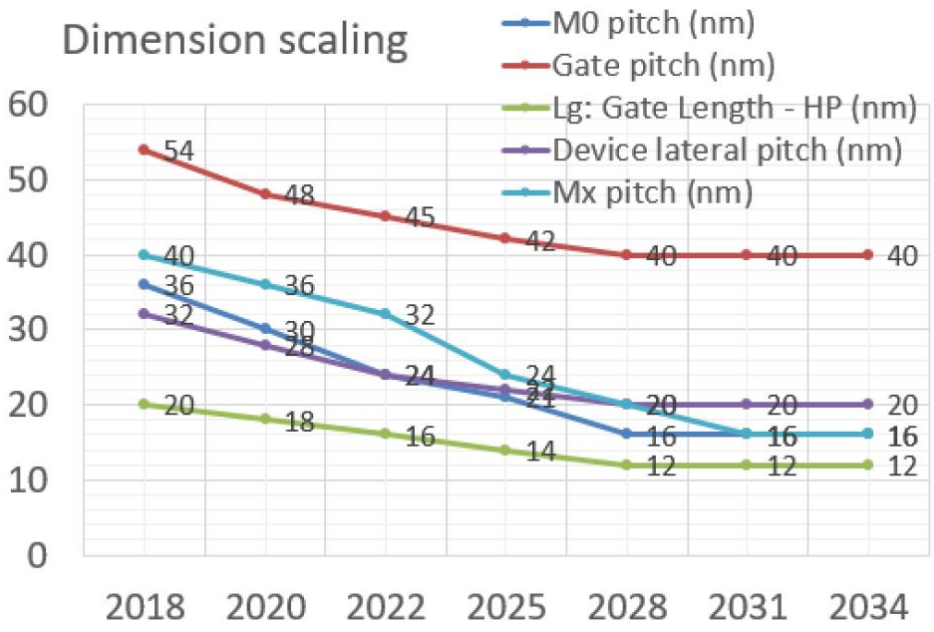

Figure 1.3. Roadmap for logic devices (IRDS) (Ref. 7).

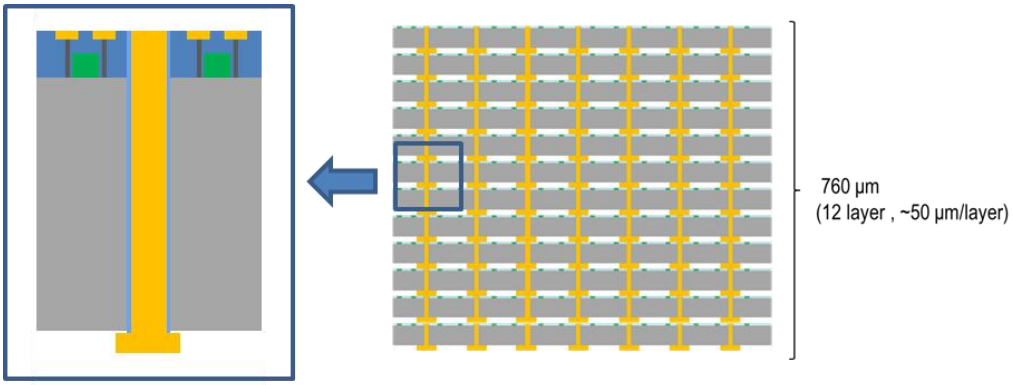

Figure 1.4. Simplified image of packaging technology using TSV.

1.2. Cu electrodeposition and Through-silicon-via (TSV) filling

Copper (Cu) is widely used as a metallization material because of its superior properties, high electromigration resistance, and a low electrical resistivity,[13-16] and it is deposited in the feature by Cu electrodeposition. Cu electrodeposition is a process to reduce Cu ions in the electrolyte on the conductive substrate by externally applying electrons as shown in Fig. 1.5. The substrate with the Cu seed layer is used as a working electrode in the electrodeposition process. After dipping both the working electrode and metal or insoluble electrode used as a counter electrode, Cu deposition occurs on the working electrode by applying current or potential. The size of features varies from tens of nanometers (e.g. Damascene features) up to hundreds of micrometers (e.g., microvias and through-holes in PCBs).[15-27] Size variability of filling features has been resolved by modifying the electrodeposition condition.

Electrodeposition profiles are classified into three modes during the feature filling as shown in Fig. 1.6. Subconformal deposition is the mode where the TSV entrance is clogged by deposit, forming voids. Cu ions are preferentially consumed for the deposition near the entrance of the TSV, not reaching the bottom of the TSV, during the Cu electrodeposition in the absence of any additives or at high applied current

densities.[17] Therefore, subconformal deposition occurs, forming voids inside the deposit. Conformal deposition with seam is obtained when the deposition rates on every surface, the top, side walls, and bottom, are the same. Because the voids and seams, formed in the via by subconformal or conformal deposition, expands during the repetitive operation of semiconductor devices after the annealing,[18, 19] void-free filling is definitely required for the device reliability. Superconformal deposition, or so-called superfilling, is caused by selective deposition on the bottom of the TSV, which induces bottom-up growth.[15-20] Concentrating metal growth at the bottom of the concave structures, defect-free filling can be achieved.

Thus, various Cu-electrodeposition methods for superconformal filling have been studied with the use of organic additives because they can control the local deposition rate through an adsorption on the deposited surface.[19-27] Polyethylene glycol (PEG) and bis-(3-sulfopropyl) disulfide (SPS) are a representative suppressor and accelerator in Cu electrodeposition, respectively, which is shown in Table 1.1. The combinations of PEG and SPS are widely used in Cu metallization for the void-free filling of features in damascene structures.[28-32]

In the Cu electrodeposition for TSV filling, additional additives, levelers, and more advanced electrodeposition methods were required due to the larger scale of tens of

micrometers of TSVs with a high aspect ratio.[33-41] Levelers, which show strong inhibition and convection dependency, are additionally added with suppressor and accelerator for the selective deposition according to feature of TSV. Levelers effectively inhibited at the entrance and sides of the TSVs, while promoting Cu deposition at the bottom to avoid occluding TSVs before bottom-up filling,[42-45] which will be discussed in detail at the next chapter.

In addition to the levelers, Cu electrodeposition methods for TSV filling are generally designed to facilitate the mass transport of Cu ions into the TSV because the depletion of Cu ions inside high-aspect-ratio TSVs during the filling is one of the main causes of voids in TSVs. Therefore, during TSV filling, waveforms may be introduced into the applied current, such as pulse current and pulse-reverse current, to provide time for diffusion of Cu ions into TSVs as shown in Fig. 1.7.[39-41] Methods of physically promoting mass transport of Cu ions are also used, such as ultrasonic sound[33-35] (Fig. 1.8) and applying convection[44-49].

Table. 1.1. Representative Accelerators and Suppressors in Cu Electrodeposition

Accelerator	Bis(3-sulfopropyl) disulfide disodium salt (SPS)	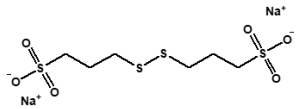
	3-Mercapto-1-propanesulfonic acid sodium salt (MPSA)	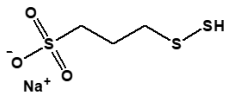
	3-*N,N*-Dimethylaminodithiocarbamoy-1-propanesulfonic acid (DPS)	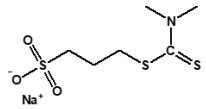
Suppressor	Polyethylene glycol (PEG)	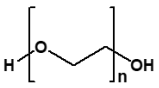
	Polypropylene glycol (PPG)	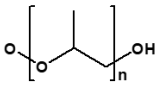
	PEG-PPG block copolymer	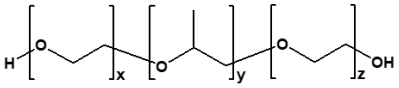
	Polyethyleneimine	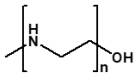

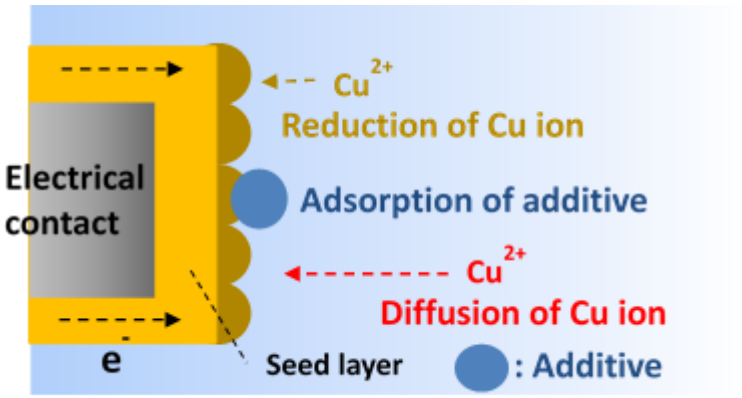

Figure 1.5. Schematic diagram of Cu electrodeposition.

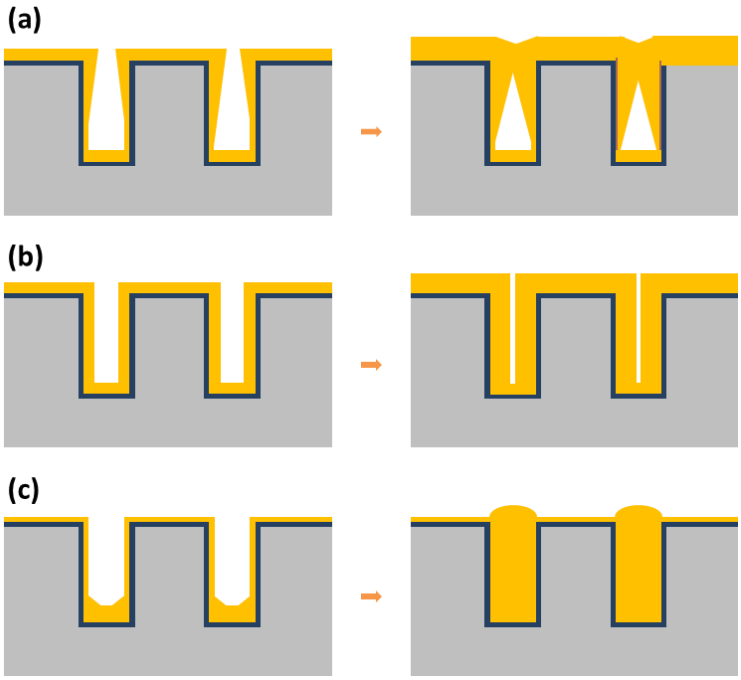

Figure 1.6. Three types of deposition profile during the TSV filling: (a) subconformal, (b) conformal, (c) superconformal deposition.

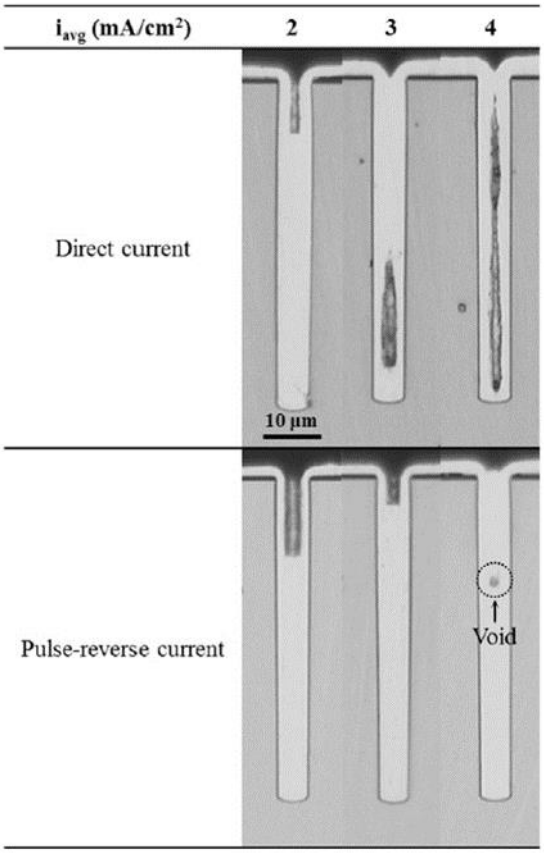

Figure 1.7. Effect of pulse-reverse current on TSV filling (Ref. 39).

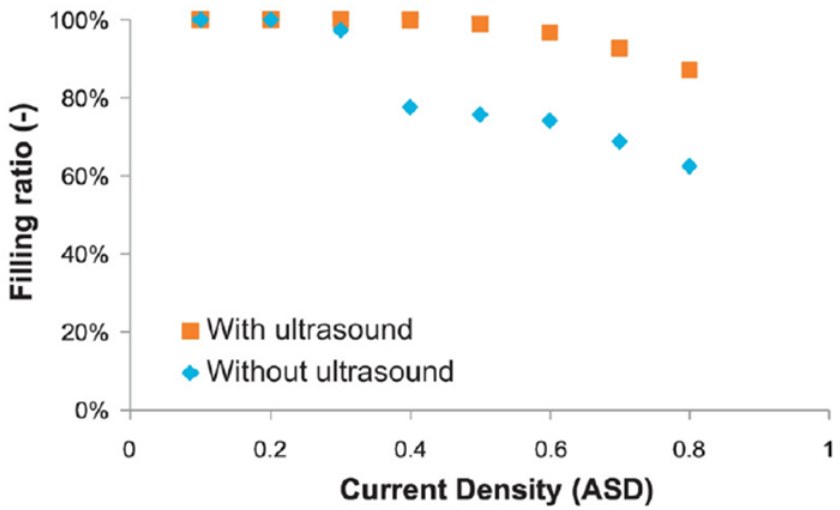

Figure 1.8. Effect of ultrasound on TSV filling (Ref. 34).

1.3. Levelers for the TSV filling and filling mechanism

For the Damascene features, a combination of an accelerator and a suppressor is sufficient to achieve defect-free filling, whereas an additional organic leveler is necessary for microvias and through-holes.[50-59] The leveler additionally inhibits Cu deposition near the opening of filling features, facilitating the bottom-up filling of Cu by suppressing the effect of accelerator[60-62] or leveling deposit surface[63-66]. The previous achievements in Cu electrodeposition and the development of organic levelers have contributed to the continuous development of the semiconductor industry. Levelers, such as sulfonated diallyl dimethyl ammonium chloride copolymer (SDDACC)[50, 67, 68], Janus Green B (JGB)[69, 70], tetronic701[54-56, 71, 72], and etc.[73-76], as shown in Fig. 1.9. along with these Cu electrodeposition methods, play a key role in defect-free TSV filling. The levelers enable selective Cu electrodeposition at the bottom of the vias by suppressing deposition at the top surface. Most of levelers, such as JGB and SDDACC, have characteristics in common: convection-dependent adsorption and suppression synergy with suppressors (Fig. 1.10). These levelers effectively suppress the Cu electrodeposition at the TSV entrance (top) through

strong adsorption under convective conditions, allowing preferential Cu deposition at the bottom where convection is relatively weak.[44-47, 49] Levelers such as Tetronic 701 show another characteristic, suppression-breakdown which shows a S-NDR (S-shaped negative differential resistance) profile after iR-compensation as shown in Fig. 1.11.[54-56, 71, 72] This leveler suppresses Cu electrodeposition with strong adsorption until the deposition potential reaches a certain level, then quickly detaches from the surface after this point, eliminating the suppression effect. Therefore, this leveler bifurcates the surface with potential distribution into active and passive regions, according to the critical potential. The formation and breakdown of this suppression effect on the deposition surface, is dependent on applied potential, and concentrations of leveler and chloride ions.[54-56, 71, 72] Due to the structural nature of TSV, these conditions vary from location to location within the via, and the resulting suppression effect occurs mainly at the top rather than the bottom. Therefore, in this case, a single leveler can be used to successfully fill TSVs larger than the micrometer scale.[71, 72, 77-80]

Levelers, inorganic[42, 43, 47, 52, 53] and synthesized organic levelers[28, 37, 44, 48], were introduced by our group for TSV filling in a three-additive system as shown in Table 1.2. Inorganic levelers, iodide ions showed convection-

dependent adsorption and suppression synergy with suppressors by forming a suppressing layer of Cu-halide complex. A tetraethylene-glycol-based synthetic organic leveler with two quaternary ammonium cations also showed the same characteristics,[44, 48] and defect-free TSV filling was successfully achieved using these levelers.[28, 44]

Table 1.2. Molecular Structures of the Synthesized Containing Quaternary Ammonium Cations

Synthesized leveler	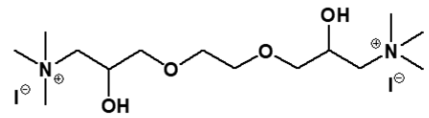 α,ω-bis(*N,N,N*-trimethylammoniomethyl)triethylene glycol diiodide)
	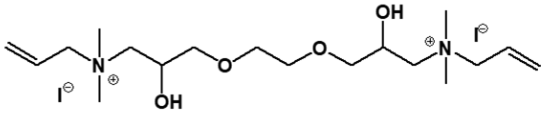 α,ω-bis(*N,N,N*-allyldimethylammoniomethyl)triethylene glycol diiodide)
	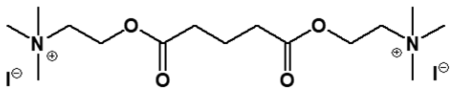 1,5-bis(2-*N,N,N*-trimethylammonioethyl)glutarate diiodide)
	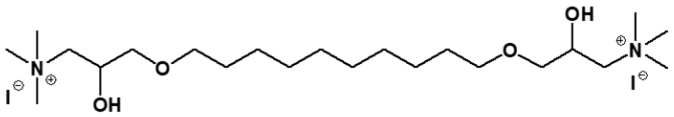 1,10-bis(3-(*N,N,N*-trimethylammonio)-2-propanol-oxy)decane diiodide)

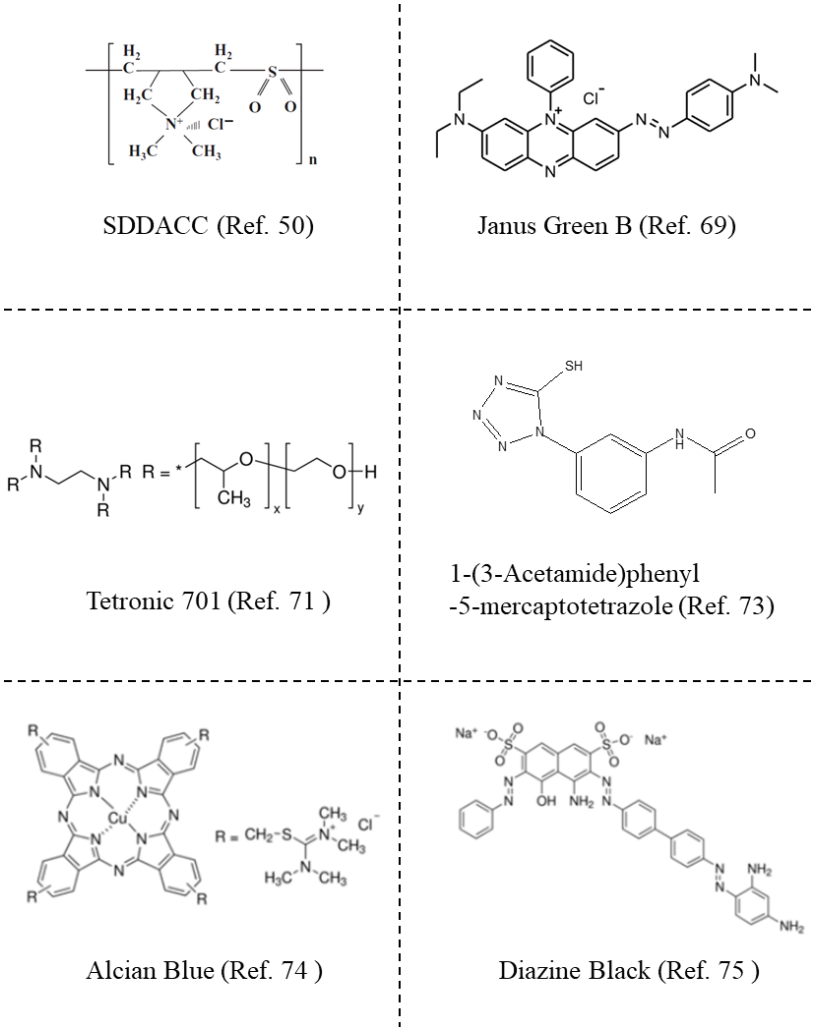

Figure 1.9. Molecular structures of the levelers reported in papers.

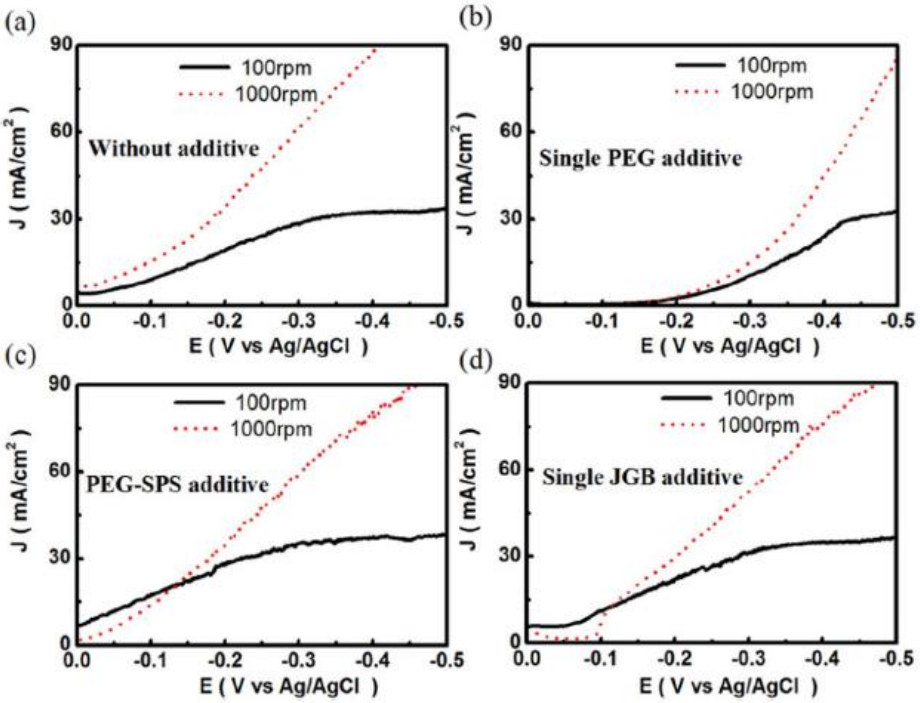

Figure. 1.10. Convection dependence of the leveler (JGB) with rotating disk electrode(RDE): (a) additives-free (b) PEG (c) PEG-SPS and (d) JGB (Ref. 69).

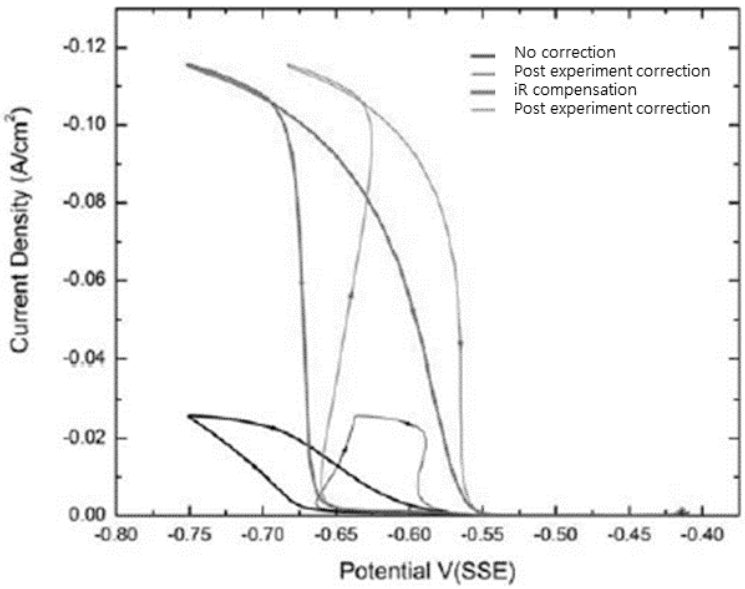

Figure. 1.11. NDR proiles with iR compensation of Tetronic 701. Post experiment correction of the voltammetry (black) for the iR losses reveals that the hysteresis is associated with a negative differential resistance (S-NDR) (Ref. 71).

1.4. Purpose of this study

It is obvious that levelers have a critical role in bottom-up filling with the strong suppression on the top accompanying the weak suppression or dominant acceleration on the bottom. In this study, new kinds of levelers for successful TSV filling are developed. At first, iodide ions were introduced. These levelers have been reported previously by our group, however, deep understanding of the working mechanism of the leveler should be required for grain sizing to minimize Cu protrusion, as well as defect-free TSV filling. We tried to understand the working mechanism of iodide ions in depth, and control the microstructure of Cu inside TSVs.

Though the iodide ions successfully induced the bottom-up filling of TSVs, however, we found that the experimental Faradic efficiency of iodide ions was only 31%. Therefore, we introduced advanced inorganic levelers, bromide ions, as an alternative to iodide ions. These inorganic halide levelers are known as inhibitors for Cu electrodeposition, which show convection dependent inhibition. We tried to investigate the effect of the bromide ions on Cu electrodeposition and filling

mechanism, comparing to the iodide ions.

After that, advanced organic levelers are synthesized and developed for TSV filling in single additive system. Effect of quaternary ammonium cations and aromatic rings was well known as functional group which shows strong inhibition. We synthesized the leveler containing these functional groups for successful TSV filling, and tried to improve the electrochemical properties by modifying the organic structure. TSV filling was conducted in single additive system, and the electrochemical behavior of the synthesized leveler was systemically investigated.

CHAPTER II

Experimental

2.1. Basic condition: electrode system, electrolyte

Electrochemical analysis and TSV filling were performed in a three-electrode system as shown in Fig. 2.1. A Cu rotating-disk electrode (RDE, 0.196 cm^2), Cu blanket wafer [Cu (physical vapor deposition (PVD), 55 nm)/Ta (PVD, 30 nm)/TaN (PVD, 50 nm)], and Cu TSV wafer [Cu (PVD, 600 nm))/Ta (PVD, 200 nm)] were used as working electrode for purpose of each experiment. The depth and diameter of the TSVs on the wafers were 60 μm and 5 μm, respectively, so aspect ratio (depth/diameter) was 12. An electronic-grade Cu rod was used as counter electrode, and Ag/AgCl (KCl saturated) or Hg/Hg_2SO_4 (K_2SO_4 saturated) was used as a reference electrode. An electrolyte composed of 1.0 M $CuSO_4$, 0.5 M H_2SO_4, and 1.4 mM HCl was used as the standard solution, to which we added some additives. The temperature of the electrolytes was precisely controlled at 30°C.

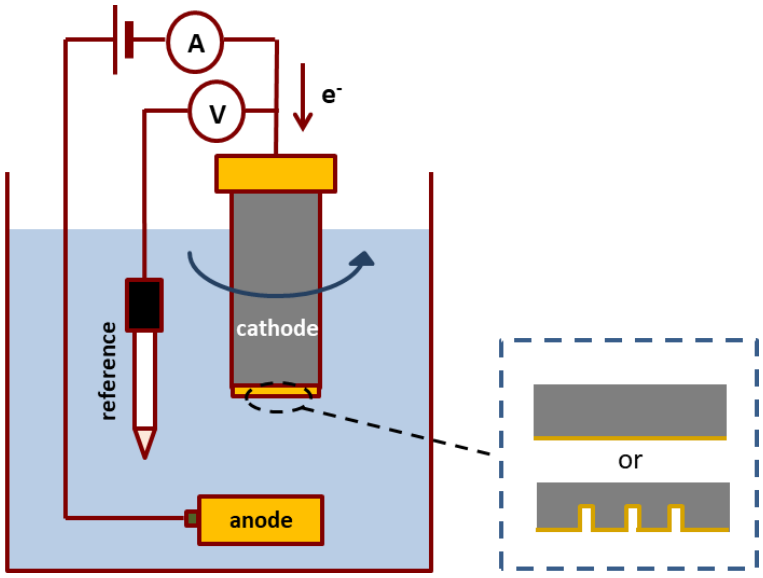

Figure 2.1. Schematic diagram of the three-electrode system for the Cu electrodeposition.

2.2. TSV filling using iodide ions as leveler

2.2.1. Electrochemical analysis

Various combination of polyethylene glycol-polypropylene glycol copolymer (PEG-PPG, molecular weight: 1100), SPS, and NH_4I were added in standard solution for electrochemical analysis. 50 μM PEG-PPG and 10 μM SPS were used as suppressor and accelerator, respectively, and 400 μM NH_4I was added as leveler. The electrochemical behavior of the additives during Cu electrodeposition was investigated by linear sweep voltammetry (LSV) with the potential range from 150 to -350 mV (vs. Ag/AgCl) at a scan rate of 10 mV/s, and the rotating speed of the RDE was set to 0 and 900 rpm to replicate convective conditions at the bottom and top of the TSV, respectively. The derivatization experiment was also performed using both the wafer and Cu RDE as the working electrodes. Both the wafer and the Cu RDE were immersed in the additive-containing solution for 30 s to induce the adsorption of the additives prior to the electrochemical measurement. All of the electrochemical analysis was conducted with a

PAR 263A potentiostat (EG&G, Princeton Applied Research Corporation). For the electrochemical measurement, Ag/AgCl electrode (KCl saturated) was used as reference electrodes.

2.2.2. TSV filling and visualization of Cu microstructure

The two types of constant current methods were employed for the TSV filling: one-step (1 mA/cm^2 for 1200 s) and two-step (1 mA/cm^2 for 500 s, then 3 mA/cm^2 for 233 s) fillings. The total charge for the deposition was 1200 mC/cm^2 based on the geometric area (1 cm^2) The substrate was horizontally rotated at 900 rpm to induce convection during the filling process. After the filling, the sample was annealed at 400˚C for 30 min in an Ar atmosphere. TSV filling was conducted with a PAR 263A potentiostat (EG&G, Princeton Applied Research Corporation), and Ag/AgCl electrode (KCl saturated) was used as reference electrodes. Surface morphology and composition of the derivatized Cu blanket wafer were observed using field-emission scanning electron microscopy (FESEM; MERLIN Compact, ZEISS) equipped with an energy dispersive spectrometer

(EDS; Thermo Fisher). The microstructure of Cu in TSV was investigated by electron back-scattered diffraction (EBSD; TexSEM Laboratory) in scanning electron microscopy (SEM; SU70, Hitachi). The height of Cu protrusions was measured by atomic-force microscopy (AFM; Agilent Technologies, 5420).

2.3. TSV filling using bromide ions as leveler

2.3.1. Electrochemical analysis

The additives used in this study were PEG-PPG (molecular weight: 1100), SPS, NH_4I, and NH_4Br. The concentrations of PEG-PPG and SPS were 50 and 10 μM, respectively. The NH_4I and NH_4Br were added to introduce I^- and Br^- into the electrolyte, and their concentrations were between 100 and 600 μM. The electrochemical behaviors of I^- and Br^- were investigated using LSV. The electrochemical potential was scanned from 150 to -350 mV (vs. Ag/AgCl) at a scan rate of 10 mV/s. The rotating speed of the RDE were 0 and 1000 rpm, which represent the convection conditions at the bottom and top of TSVs. The electrochemical measurements were performed in a three-electrode system with a potentiostat (PAR 263A, Princeton Applied Research). For the electrochemical analysis, Ag/AgCl electrode (KCl saturated) was used as reference electrodes.

2.3.2. TSV filling and Cu film deposition

The current density for TSV filling was fixed at 1 mA/cm^2. The substrate was rotated at 1000 rpm to apply convection during the filling experiments and TSV filling was performed with a PAR 263A potentiostat (EG&G, Princeton Applied Research Corporation). After Cu electrodeposition, the sample was molded in acrylic and polished using a polisher (RB 209 MINIPOL, TOPMET) with sandpaper and abrasive slurries. The cross-sectional images to inspect the TSV filling performance were taken by optical microscopy (OM, NEW-IMS-345, SOMETECH). In addition, the surface and cross-section of Cu films were observed by field emission scanning electron microscopy (FESEM, S-4800, Hitachi).

2.4. TSV filling in single additive system

2.4.1. Synthesis of advanced organic additive

All of the synthetic route for levelers in this study were performed by Yoonjae Lee in Laboratory of professor Young Gyu Kim. The levelers were synthesized from PEG of various molecular weights: ethylene glycol monomer (EG), PEG600, and PEG1000. The synthesized levelers were named Lev1, Lev600, and Lev1000 depending on the molecular weight of PEG, the starting material. All the chemicals were obtained from commercial sources and were used without further purification. Tetrahydrofuran (THF) was distilled immediately prior to use from sodium and benzophenone under nitrogen atmosphere. Air or moisture sensitive reactions were carried out under nitrogen atmosphere using oven-dried glassware. The reactions were monitored with TLC silica gel 60 F254 plate, stained with a p-anisaldehyde or a ninhydrin stain solution. Column chromatography was performed on silica gel 60 (70-230 mesh). 1H and 13C nuclear magnetic resonance (NMR, Avance-400, Bruker) spectra were analyzed at 400 and 100

MHz, respectively, in deuterated chloroform (CDCl3) or deuterated methanol (MeOH-d4). The 1H and 13C NMR spectroscopic data were reported in ppm (δ) from the internal standard (TMS, 0.0 ppm) or residual solvent peaks of CDCl3 (7.26 and 77.16 ppm, respectively) or MeOH-d4 (3.31 and 49.00 pp m, respectively): the chemical shift (the integration, the multiplicity, coupling constant in Hz). High resolution mass spectra (HRMS, JMS-600, JEOL) were measured by the fast atom bombardment (FAB) ionization method and analyzed with a magnetic sector mass analyzer. Matrix-Assisted Laser Desorption Ionization mass spectroscopy (MALDI-ToF, Voyager DE-STR, Applied Biosystems) was conducted in the reflector mode with a 3 ns pulse nitrogen laser at 337 nm. The samples were prepared with THF and 2,5-dihydroxybenzoic acid (DHB) as matrix. The synthetic route is shown in Fig. 2.2 (see appendix 3 for details).

2.4.2. Electrochemical analysis

PEG1000 was used as a control leveler, which has no quaternary ammonium cations and naphthalene ring. The concentration of PEG1000 and the levelers were 100 μM.

Since a small amount of bromide ions was present in the synthesized leveler, 200 μM NH_4Br was also added to check the interaction between PEG and bromide ions in the case of PEG1000. Electrochemical measurements were conducted with a potentiostat (EG&G 2273, Princeton applied research) in a three-electrode system. Hg_2SO_4 electrode (K_2SO_4 saturated) was used as the reference electrodes, because some problems could occur in Ag/AgCl electrode when it was used with inorganic halide ions for long time. The electrochemical behaviors of the levelers were investigated using LSV and cyclic voltammetry (CV). LSV was performed in the potential range of -300 mV to -800 mV (vs. Hg/Hg_2SO_4). CV was conducted applying the following parameters: start potential of -300 mV, vertex potential of -750 mV, and stop potential of -400 mV. In both analyzes, the scan rate was 10 mV/s, and the rotating speed of the RDE was set to 1,000 rpm and 0 rpm to replicate convective conditions at the top and bottom of the TSV, respectively. Electrochemical impedance spectroscopy was also performed at 0 mA in the frequency range of 100 Hz to 10 kHz with an AC current amplitude of 100 $\mu A/cm^2$ rms to obtain solution resistance for iR compensation, and the resistances were 9.5, 13.5, 11.2, 9.7,

10.4, and 9.6 ohm with additive-free, Lev1, Lev600, Lev1000, Br^- and PEG1000, and PEG1000, respectively.

2.4.3. TSV filling and Cu deposition

The substrate was rotated at 1,000 rpm to apply convection and a current density of 1 mA/cm^2 was applied during TSV filling for 500 or 1000 s. Electrochemical measurements were conducted with a potentiostat (EG&G 2273, Princeton applied research) in a three-electrode system, and Hg_2SO_4 electrode (K_2SO_4 saturated) was used as the reference electrodes. After TSV filling, the wafer was molded in acrylic and polished using a polisher (RB 209 MINIPOL, TOPMET) with sandpaper and abrasive slurries. the cross-section of the TSVs was observed with an optical microscope (OM, NEW-IMS-345, SOMETECH) to investigate the shape and uniformity of TSV filling. The surface and cross-sectional images of Cu films on TSV wafer were obtained using a field emission scanning electron microscope (FESEM, S-4800, Hitachi).

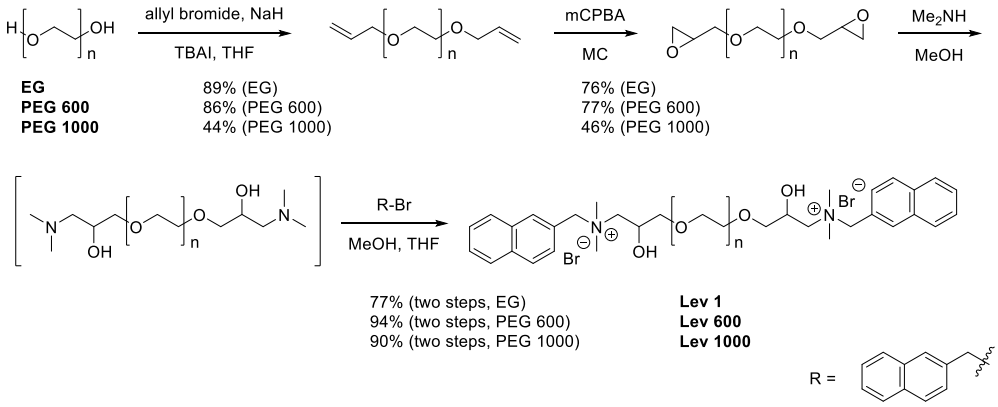

Figure 2.2. Synthetic route for the synthesized levelers. The abbreviations are ethylene-glycol (EG), tetrahydrofuran (THF), tetrabutylammonium iodide (TBAI), dichloromethane (MC), deuterated methanol (MeOH), and meta-chloroperoxybenzoic acid (mCPBA).

CHAPTER III

Results and Discussion

3.1. TSV filling using iodide ions as leveler

The successful TSV filling with iodide ions has been reported previously by our group.[43, 47] However, we needed an in-depth understanding of the working mechanism of iodide ions during Cu electrodeposition in order to perform TSV filling and grain sizing simultaneously. Therefore, the working mechanism of iodide ions was investigated to understand their role in TSV filling and their effect on Cu microstructure. Iodide ions can be added for TSV-scaled trench filling because they behave like levelers, such as convection-dependent suppression and synergistic suppression with PEG-PPG.[44, 49] Given a deeper understanding on the working mechanism of iodide ions, we tried to control the microstructure of Cu inside TSVs to minimize Cu protrusion.

3.1.1. Filling results and filling mechanism of iodide ions

TSV filling was performed with various concentration of iodide ions as leveler in three additives system containing PEG-PPG and SPS as suppressor and accelerator, respectively as shown in Fig. 3.1. In the solution containing only PEG-PPG and SPS, void was observed in the TSV. However, by adding iodide ions, TSV was sufficiently filled in the wide range of concentration of iodide ions.

In Fig. 3.2, the electrochemical reduction of Cu ions in the presence of additives was investigated with Cu RDE by LSV at 0 rpm and 900 rpm, which represent the convection conditions at the bottom and top of TSVs, respectively. In both conditions, the addition of iodide ions decreased the reduction current, indicating that iodide ions inhibit the Cu deposition with or without other additives. The degree of inhibition varies with the additive combination. The potential for 10 mA/cm^2 at each condition were 71, 20, -80, and -195 mV at stationary condition, and 68, -78, -124, and -225 mV at convective condition, respectively, in the order of Additive-free < I^- < PEG-PPG+SPS < PEG-PPG+SPS+I^-. The inhibition effect was significantly increased at 900 rpm in the presence

of iodide ions, demonstrating the convection-dependent inhibition of iodide ions. Iodide ions also have a greater inhibition effect when PEG-PPG and SPS are co-added, and this synergistic effect was more pronounced at 900 rpm than in the stationary condition.

The most likely inhibition mechanism of iodide ions is the formation of non-conducting CuI on the electrode surface, which suppresses the reduction of Cu ions during Cu electrodeposition. Table 3.1 lists the possible electrochemical reactions at the Cu electrode and their reduction potentials in the presence of iodide and cupric ions.[81, 82] The electrochemical reactions are strongly dependent on the concentration of iodide ions. The reduction potentials of CuI deposition (Eq. 3) shifts in the negative direction as the concentration of iodide ions decreases, whereas that of CuI reduction (Eq. 5) moves in the positive direction. Figs. 3.3(a) and (b) show current-time curves of Cu deposition with 400 μM iodide ions at different applied potentials under convective condition. The open-circuit potential of the Cu RDE at the early stage was 84 mV. At the potential of 50 mV, the addition of iodide ions decreased the reduction current density to one-tenth of that without iodide ions (Fig. 3.3(a)), indicating that iodide ions inhibited the reduction

of cupric ions by forming a CuI layer on the surface of the electrode. The formation of CuI (Eq. 3) is favorable below 200 mV in the concentration range. The CuI_2^- formation (Eq. 2) and its reduction (Eq. 1) may also take place to some extent. However, they have only a minor influence on the inhibition mechanism. No other electrochemical reactions associated with iodide ions would take place at 50 mV. The inhibition by iodide ions was also observed at 0 mV. The reduction current density was significantly reduced, by about 87% of that without iodide ions. However, the slight increase in current density was observed after 420 s in the presence of iodide ions (Fig. 3.3(b)), which was not observed at 50 mV. This indicates that additional electrochemical reactions occur. At 0 mV, the formation of CuI (Eq. 3) would be faster than at 50 mV, significantly reducing the surface concentration of iodide ions. The depletion of iodide ions near the electrode surface shifts the reduction potential of CuI (Eq. 5) in the positive direction. Therefore, CuI may start to be reduced when the surface concentration of iodide ions is below 0.2 μM, where its reduction potential becomes 0 mV. In this case, the formation of CuI_2^- is negligible because its reduction potential shifts negatively as the iodide ions concentration

decreases. At the more negative potentials, -50 mV and -100 mV, the consumption rate of iodide ions would be much faster than at 0 mV. The fast consumption of iodide ions makes the CuI reduction (Eq. 5) more favorable. Therefore, the current density, which is decreased by the CuI deposition (Eq. 3) at the initial stage, starts to increase much sooner than at 0 mV: 16 s and 4 s for -50 mV and -100 mV, respectively. The current densities then increase almost up to the values of the additive-free case. In this stage, CuI deposition (Eq. 3), cupric ion reduction (Eq. 4), and CuI reduction (Eq. 5) take place simultaneously, although the exact proportion of the reduction current density for each electrochemical reaction is not clear. However, we supposed that most of the current density would be used for cupric ion reduction, because the concentration of iodide ions is 2500 times lower than that of cupric ions. This indicates that the cupric ion reduction is not effectively inhibited by CuI at the potentials more negative than -50 mV. Hence, we concluded that the formation of CuI is a key process of the inhibition mechanism of iodide ions, and the inhibition effect is mitigated at highly negative potentials due to the electrochemical reduction of CuI.

The formation of CuI was also investigated in depth by using derivatization. Fig. 3.4 shows the surface morphologies of Cu blanket coupon wafers after dipping in the solutions containing iodide ions and other additives. White particles were formed on the surface after the dipping, and these white particles were identified as CuI (49.41 at% Cu and 50.59 at% I) by EDS analysis. Hence, CuI also forms via the following chemical reactions in addition to the electrochemical reaction (Eq. 3).

$$Cu^{2+} + Cu \leftrightarrow 2Cu^{+} \qquad [6]$$

$$Cu^{+} + I^{-} \leftrightarrow CuI \qquad [7]$$

At the Cu surface, cuprous ions are generated through the disproportionation reaction (Eq. 6), simultaneously reacting with iodide ions to form CuI (Eq. 7). It is notable that the larger portion of the surface was covered by CuI when the convection (Figs. 3.4(a) and 4(b) or Figs. 3.4(c) and 4(d)) and/or other additives (Figs. 3.4(a) and (c) or Figs. 3.4(b) and (d)) were introduced in the presence of iodide ions. PEG-PPG and SPS increase the residence time of cuprous ions in the vicinity of the electrode surface by forming an inhibition layer of Cl^{-}-Cu^{+}-PEG-PPG and catalytically reducing cupric ions

to cuprous ions via the formation of a Cu^{+}-thiolate complex.[83, 84] The high surface concentration of cuprous ions may facilitate the chemical formation of CuI. The introduction of convection would also have a positive influence on the chemical formation of CuI by promoting the mass transfer of iodide ions.

Fig. 3.5 shows LSV results of the derivatized Cu electrodes in the standard solution. The derivatization was performed in the solution containing different combinations of the additives under the stationary or convective condition. No convection was applied during the electrochemical analysis. In this case, the inhibition strength is related to the stability of the pre-formed CuI inhibition layer on the surface, because the solution is additive-free. The stronger inhibition effect of CuI was observed on the derivatized electrodes under the convective condition rather than the stationary condition. The combination of the iodide ions and other additives (PEG-PPG and SPS) also increased the inhibition effect, showing that the synergistic inhibition effect still exists on the derivatized electrodes. These results correspond well to the coverage of CuI formed during the derivatization (Fig. 3.4), validating that the formation of CuI is a key

inhibition mechanism. However, the inhibition effect on the derivatized electrodes was weaker than that shown in Fig. 3.2(a). For instance, on the electrode derivatized with NH_4I, PEG-PPG, and SPS, the reduction of Cu ion was suppressed up to -100 mV, whereas the reduction was suppressed up to -180 mV on the electrode in the solution containing the same additives, perhaps because of the positive shift of CuI reduction potential (Eq. 5) and the short supply of iodide ions to form CuI.

Given these investigations, the mechanism of the convection-dependent inhibition of iodide ions was identified. During the Cu deposition, a CuI layer is formed on the Cu surface both chemically and electrochemically in the presence of iodide ions, blocking active sites for Cu-ion reduction. The inhibition strength depends on the coverage of CuI formed on the surface. As CuI is formed via chemical and electrochemical reactions and is simultaneously removed by the electrochemical reduction, the amount of CuI formed is determined by the combined effect of the three reactions. The formation of CuI is favorable when the convection is introduced, because the mass transfer of iodide ions to the electrode surface is facilitated. The presence of PEG-PPG and SPS also increases the

amount of CuI by increasing the surface concentration of cuprous ions. On the other hand, CuI is removed via the electrochemical reduction when the surface concentration of iodide ions is low or when the applied potential is highly negative.

Table 3.1. Possible Electrochemical Reactions at the Cu Electrode and Their Reduction Potentials in the Presence of I^- (400 μM) and Cupric Ions (1.0 M)

Eq.	Reaction	Equilibrium potential	V (vs. Ag/AgCl)
1	$CuI_2^- + e \rightarrow Cu + 2I^-$	$E = 0.005 + 0.059 \log([CuI_2^-]/[I^-]^2)$	–
2	$Cu^{2+} + 2I^- + e \rightarrow CuI_2^-$	$E = 0.676 + 0.059 \log([Cu^{2+}][I^-]^2/[CuI_2^-])$	–
3	$Cu^{2+} + I^- + e \rightarrow CuI$	$E = 0.867 + 0.059 \log[Cu^{2+}][I^-]$	0.471 V
4	$Cu^{2+} + 2e \rightarrow Cu$	$E = 0.34 + 0.029 \log[Cu^{2+}]$	0.144 V
5	$CuI + e \rightarrow Cu + I^-$	$E = -0.186 - 0.059 \log[I^-]$	-0.182 V

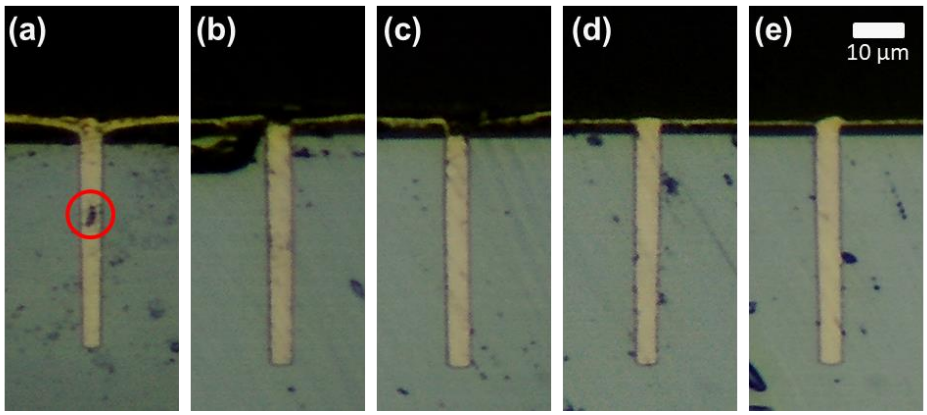

Figure 3.1. Cross-section images of TSV filled by Cu with the addition of 10 µM SPS, 50 µM PEG-PPG, (a) 0 µM, (b) 100 µM, (c) 200 µM, (d) 400 µM and (e) 600 µM of NH_4I at the current density of 1 mA/cm^2 applied for 1000 s.

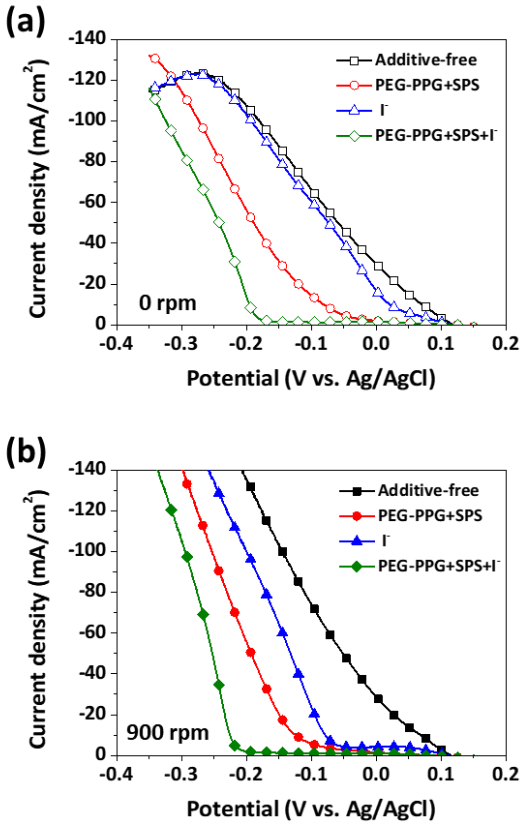

Figure 3.2. LSV curves of Cu RDE in the additive-containing standard solutions under (a) stationary and (b) convective condition. The concentrations of additives were 50 μM, 10 μM, and 400 μM for PEG-PPG, SPS, and NH_4I, respectively.

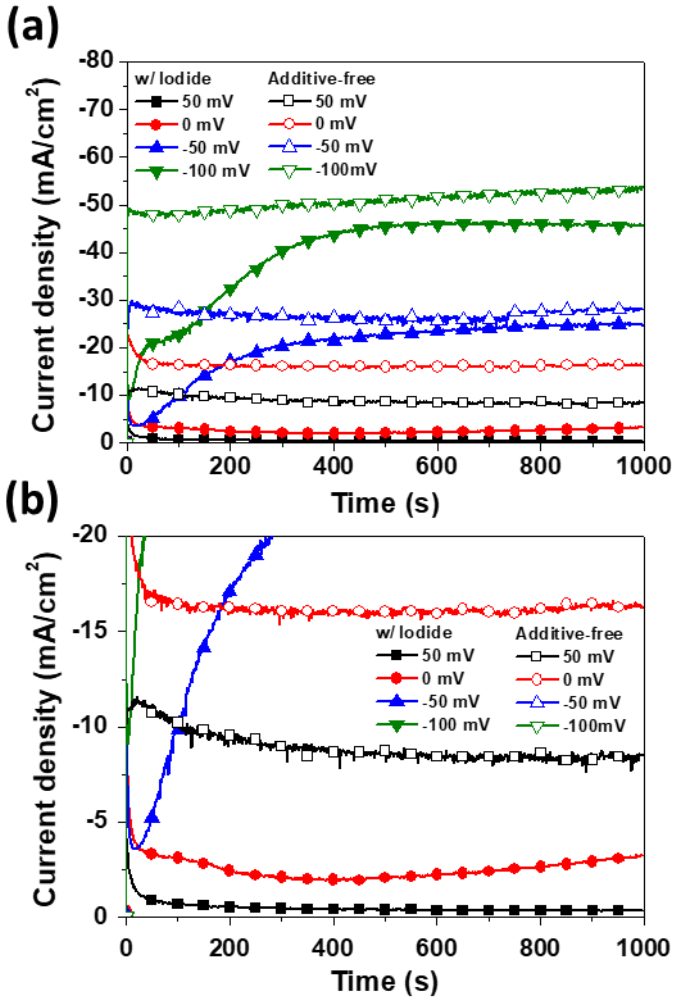

Figure 3.3. (a) Current-time curves of Cu RDE in the standard solution with and without iodide ions (400 μM NH_4I), and (b) the enlarged graph of (a).

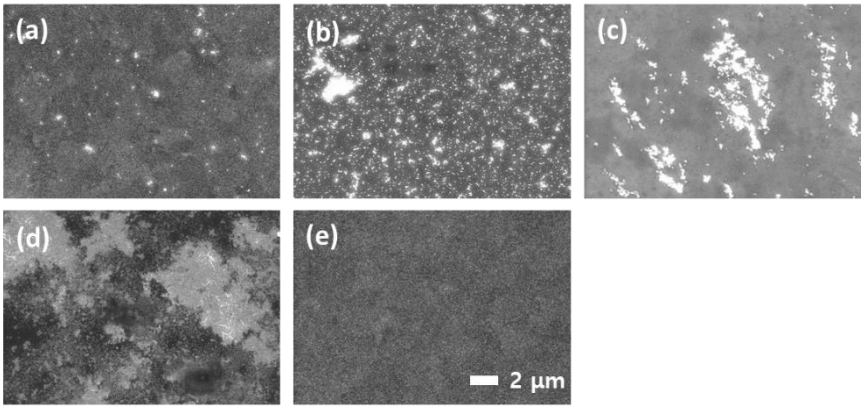

Figure 3.4. Surface morphologies of the Cu blanket coupon wafers after the derivatization in the additive-containing standard solutions under stationary and convective conditions, (a) NH_4I at 0 rpm, (b) NH_4I at 900 rpm, (c) NH_4I + PEG-PPG + SPS at 0 rpm, (d) NH_4I + PEG-PPG + SPS at 900 rpm, and (e) no additive. The concentrations of additives were 50 μM, 10 μM, and 400 μM for PEG-PPG, SPS, and NH_4I, respectively.

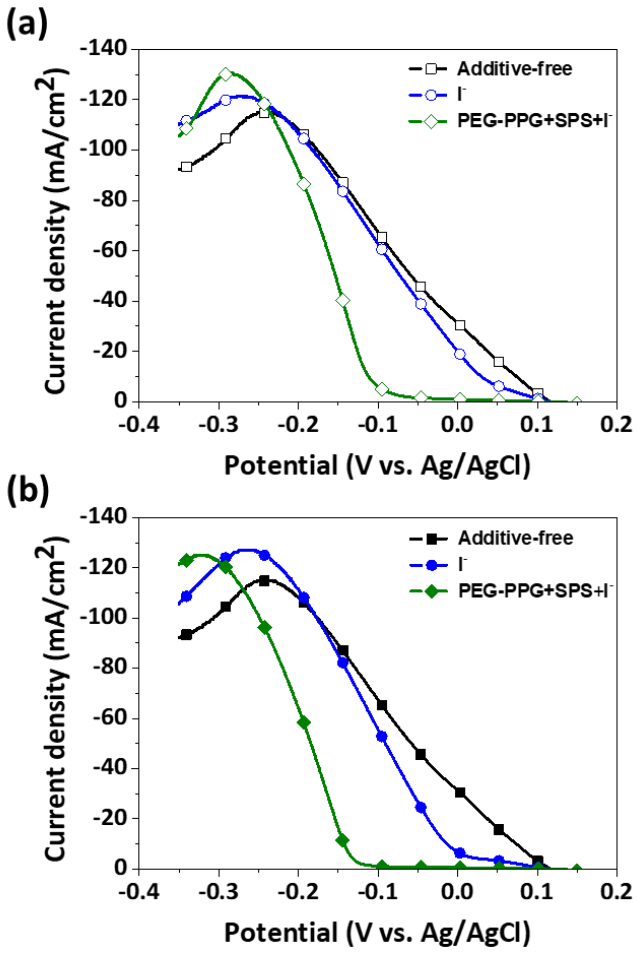

Figure 3.5. LSV curves of Cu RDE in the additive-free standard solution after the derivatization under (a) stationary and (b) convective conditions. No convection was applied during the electrochemical analysis. The concentrations of additives used for the derivatization were 50 μM, 10 μM, and 400 μM for PEG-PPG, SPS, and NH_4I, respectively.

3.1.2. Microstructure control of Cu in TSV and its application

The inhibition effect of CuI also affects the Cu microstructure in TSV filling. Fig. 3.6(a) shows the TSV after the Cu filling with the additive combination of PEG-PPG, SPS, and NH_4I at constant reduction current density (1 mA/cm^2). The defect-free Cu-filled TSVs were successfully obtained with the assistance of the convection-dependent behavior of iodide ions. The distribution of Cu grains in the TSV are shown in Figs. 3.6(b) and (c). Fig. 3.6(c) shows the distribution of Cu grains disregarding twin boundaries, which are a main factor that affects Cu pumping. The relatively small Cu grains were notably observed at the top, indicating that the addition of iodide ions suppresses the grain growth especially at the top, where the surface concentration of iodide ions is high. It is not clear why iodide ions suppress the grain growth, but we suspect that the small Cu grains originate from the CuI reduction reaction (Eq. 5). The Cu deposited via Eq. 5 would form smaller grains than that directly deposited via Eq. 4 because of the lack of surface diffusion.[85-87] A reduced Cu adatom from CuI may not migrate as easily on the surface as one from Cu ions can, because of the surrounding CuI.

The Cu grains disregarding twin boundaries were grouped by size and plotted in Fig. 3.6(d). There was no Cu grain larger than 20 μm^2, and the average area of the Cu grains was measured to be 6.65 μm^2.

In order to confirm the negative effect of CuI on Cu microstructure, a two-step filling was introduced to promote Cu deposition via Eq. 4 (cupric ion reduction) rather than Eq. 5 (CuI reduction). Eq. 4 can be more dominant than Eq. 5 at the high reduction current densities because the formation rate of CuI via electrochemical and chemical reactions (Eqs. 3 and 7) is limited by the surface concentration of iodide ions. However, the high current density may lead to the failure in defect-free filling, because the inhibition effect of iodide ions becomes weak: The CuI reduction is thermodynamically more favorable at the higher current densities. Therefore, 1 mA/cm^2 of the current density was applied at the first step until the TSV was half-filled from the bottom without any defect. The higher reduction current density (3 mA/cm^2) was then applied to promote Eq. 4. No defect was found during the second step, because the aspect ratio of TSV was cut in half after the first step.

The defect-free filling profile by the two-step method is shown in Fig. 3.7. In general, grain size becomes smaller as the higher current density is applied.[87, 88] However, in comparison to Fig. 3.6, the microstructure in Fig. 3.7(b) showed a noticeable increase in grain size, especially at the top. The size of Cu grains disregarding twin boundaries also increased dramatically (Figs. 3.7(c) and (d)). The average area of the grains was 45.72 μm^2, which was 690% larger than that of the one-step filling. This result demonstrates that the formation of small Cu grains by iodide ions results from the CuI reduction, which can be avoided by promoting the direct reduction of cupric ions to Cu. The relatively small grains observed at the middle of the TSV (Fig. 3.7(c)) resulted from the CuI reduction in the course of the first step. The larger grains were distributed at the top, where the second step was applied.

The degree of Cu pumping was then observed after the annealing at 400˚C for 30 min in an Ar atmosphere. to confirm the effect of increasing grain size. Fig. 3.8 shows AFM topography images and scan profiles of the top of TSVs after the one-step and two-step fillings. The average height of Cu protrusions was 272 (± 58) nm for the two-step filling,

whereas that for the one-step filling was 509 (± 120) nm. The 47% reduction of Cu protrusion was achieved by introducing the two-step filling, which increases the average grain size in TSV, showing clearly that the Cu protrusions can be reduced by controlling Cu microstructure in TSV.

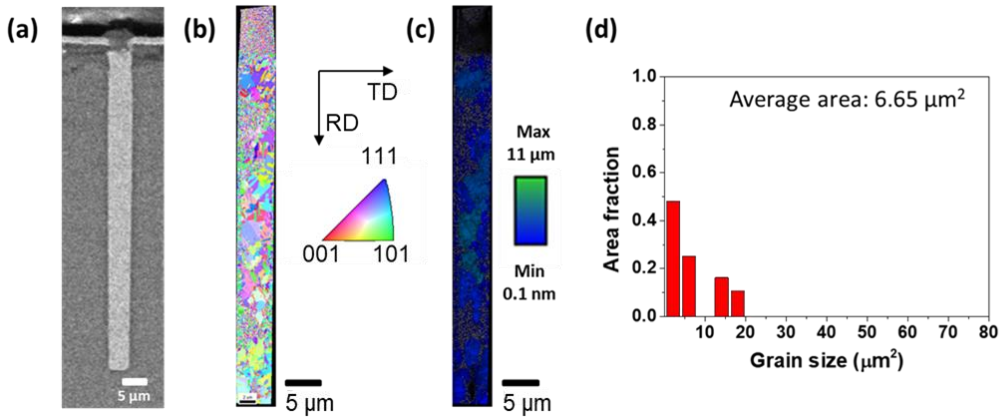

Figure 3.6. One-step TSV filling with the additive combination of NH_4I, PEG-PPG, and SPS: (a) the cross-sectional SEM image, (b) inverse pole figure map, (c) image quality (IQ) map of the Cu-filled TSV, and (d) the grain area distribution of Cu grains excluding twin boundary.

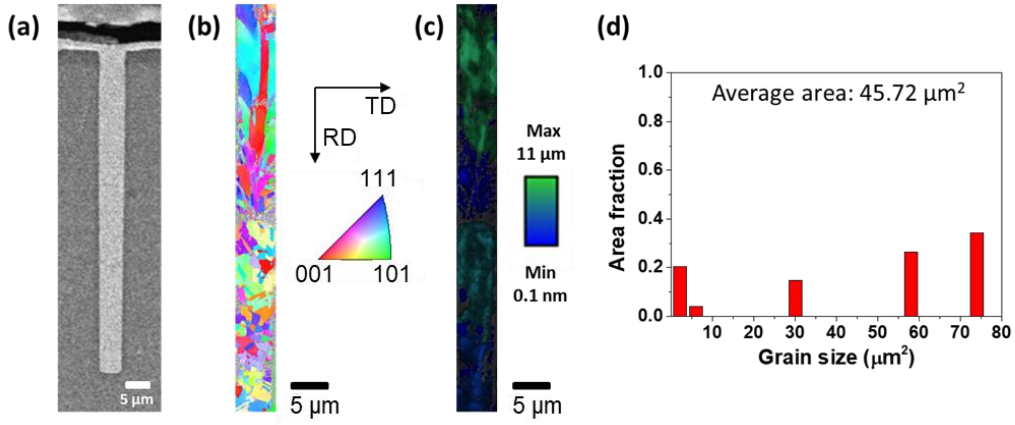

Figure 3.7. Two-step TSV filling with the additive combination of NH_4I, PEG-PPG, and SPS: (a) the cross-sectional SEM image (b) inverse pole figure map, (c) IQ map of the Cu-filled TSV, and (d) the grain area distribution of Cu grains excluding twin boundary.

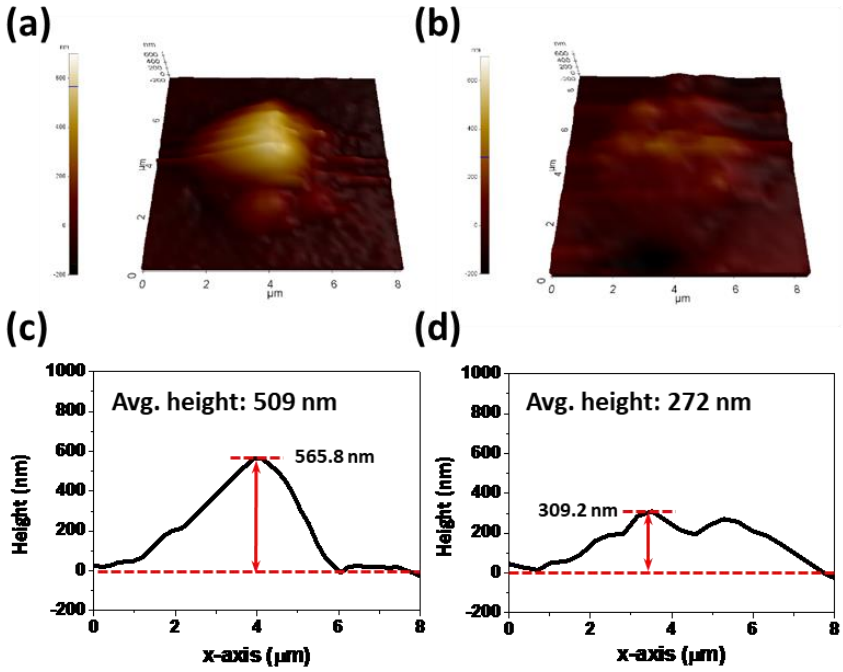

Figure 3.8. The AFM topography images of Cu protrusions formed on the TSVs filled by (a) one-step and (b) two-step fillings after the annealing at 400˚C for 30 min in an Ar atmosphere. Their scan profiles at the highest point are shown in (c) and (d), respectively.

3.2. TSV filling using bromide ions as leveler

The synergies between halide ions and organic additives are essential to achieve successful Cu bottom-up filling of Damascene features and TSVs. In a $CuSO_4$-H_2SO_4 electrolyte, Cl^- replaces the preadsorbed SO_4^{2-}-H_3O^+/H_2O layers, and increases the amount of non-hydrogen-bonded water near the electrode surface.[90] This displacement makes the Cu surface more hydrophobic, facilitating the adsorption of polymeric suppressors. Furthermore, the acceleration effect of SPS and MPSA can be achieved in the presence of Cl^-.[30, 83] The combination of Cl^- and SPS effectively accelerated the first reduction step for Cu electrodeposition, i.e. Cu^{2+} to Cu^+.[83] On the contrary, Br^- and I^- are known as inhibitors for Cu electrodeposition, and their bonds to Cu are more covalent than those to Cl^-.[91] Their adsorption depends on the convection of electrolyte, meaning that a strong agitation increases their inhibition effect on Cu electrodeposition.[42, 92] This convection-dependent inhibition of I^- successfully induced the bottom-up filling of TSVs.[42] However, we found that the experimental Faradaic efficiency of Cu electrodeposition in an I^--based electrolyte was significantly 31%, slowing down the

TSV filling process. Therefore, in this study, we explored the effect of Br^- on TSV filling as an alternative to I^-.

3.2.1. Electrochemical behavior and filling results of bromide ions

The deposition process was investigated with the linear sweep voltammetry and feature filling. Electrochemical analyses and TSV filling with bromide ions were conducted to clarify the deposition mechanism. LSV was performed at 0 and 1000 rpm to verify the effect of bromide ions and the convection dependent adsorption. The rotating speeds of 0 and 1000 rpm represented the convections at the bottom and top surface of the TSV, respectively. The linear sweep voltammograms with two rotating speeds are exhibited in Fig. 3.9. When the bromide ion was solely added, Cu deposition was weakly suppressed, and convection dependence was not observed. However, other additives, PEG-PPG and SPS, were additionally added, the inhibition strength was increased significantly, as well as the convection dependence was obtained. In three additives systems, -190 mV (vs. Ag/AgCl) should be applied for 10 mA/cm^2, while only

13 mV (vs. Ag/AgCl) was required when bromide ions were solely added. Under the convective condition, the potential for 10 mA/cm^2 of current density was negatively shifted to -224 mV (vs. Ag/AgCl) in three additives system.

In Fig. 3.10, TSV filling was performed with various concentration of bromide ions in three additive systems containing PEG-PPG and SPS as the suppressor and accelerator, respectively. As shown in Fig. 3.10(a), void was observed in the TSV due to the weak inhibition at the top surface without leveler. However, by adding bromide ions, TSV was successfully filled in the wide range of concentration of the inorganic halide ions.

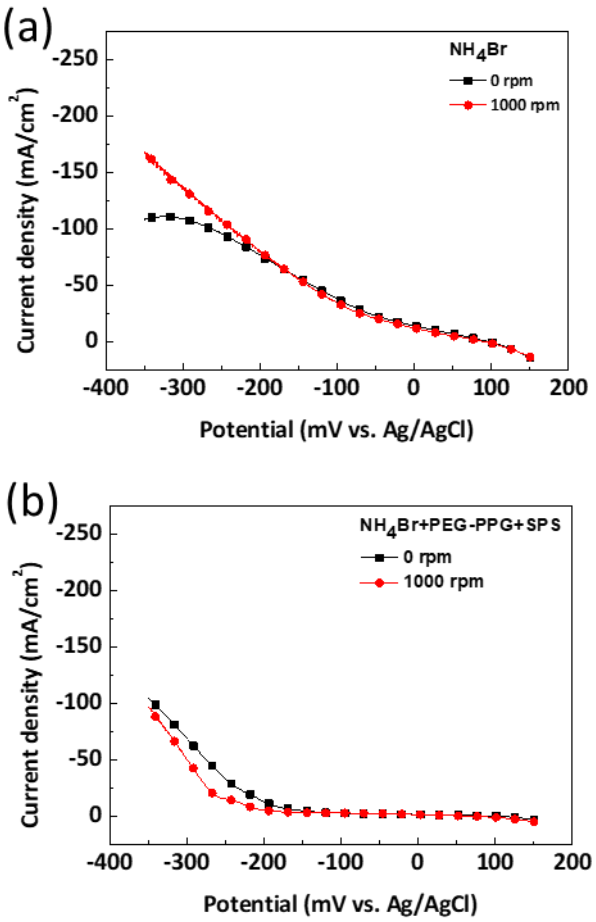

Figure 3.9. LSV curves of bromide ions under stationary and convective condition (1000 rpm) (a) without or (b) with PEG-PPG and SPS. The concentrations of additives were 50 μM, 10 μM, and 400 μM for PEG-PPG, SPS, and NH_4Br, respectively.

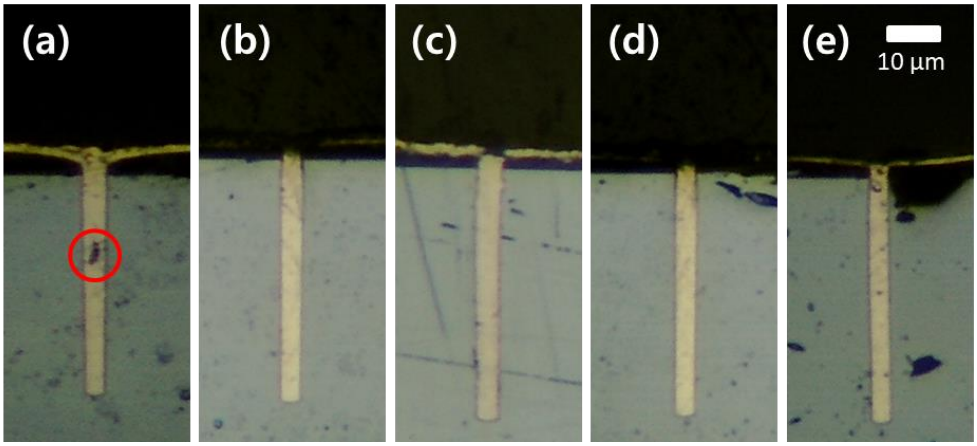

Figure 3.10. TSV filling results in three-additive system containing (a) 0, (b) 100, (c) 200, (d) 400, (e) 600 μM of NH_4Br. The solution was composed of 50 μM of PEG-PPG, and 10 μM of SPS.

3.2.2. Enhanced results with bromide ions compared to iodide ions

The electrochemical behavior of Br^- was compared to that of I^- using LSV at two different rotating speeds of the Cu disk electrode (Fig. 3.11). Both Br^- and I^- showed convection-dependent adsorption, implying that an increase in the rotating speed increased the adsorption of the halide ions as well as their inhibition effect. The I^- showed stronger inhibition of Cu^{2+} reduction compared to Br^-. Furthermore, the current density before the breakdown of the suppression layer, i.e. a rapid increase in the current, was considerably lower with I^-, meaning that the suppression layer of I^- was more compact than that of Br^-. Although the Br^- revealed weaker inhibition than did the I^-, the current density without rotating the electrode was 2.3 times larger than that with the convection at -0.2 V, which was comparable to that of I^- (6.9 times larger current density). Since the convection-dependent behavior of additives is essential in TSV filling, we further investigated the effects of Br^- and I^- on TSV filling by varying the concentrations of halide ions in the presence of SPS and PEG-PPG.

As shown in Figs. 3.1 and 3.10, both I^- and Br^- induced the successful TSV filling without void formation, where their concentrations were between 100 and 600 μM. These results indicate that the convection dependent behavior of Br^- shown in Fig. 3.11

was sufficient to achieve defect-free filling of TSVs similar to that of I^-.

Our calculation suggested that the theoretical time for complete TSV filling would be only within 60 s at 1 mA/cm^2, assuming a Faradaic efficiency of 100%, the complete inhibition of Cu deposition on the top surface of the substrate, and perfectly cylindrical TSVs, based on experimental results showing that the deposition of 1 μm-thick Cu film on a planar substrate required 2000 mC/cm^2. These calculations were valid since we accurately controlled the number of TSVs for TSV filling to 2300. However, in our experimental conditions, the deposition time to complete the TSV filling was 1000 s, which was 14–18 times longer than the calculated values. The longer deposition time observed in the experiments implied that Cu electrodeposition was not completely focused on the filling of TSVs, i.e. Cu deposition on the top surface, or some of the electrons could be consumed by undesired reactions. Therefore, the changes in filling profile over time were investigated to compare the efficiency of TSV filling with Br^- and I^-.

Fig. 3.12 shows the filling profiles at 200 and 500 s with I^- and Br^-. Both halide ions established flat growing surfaces at the bottom of TSVs, because of the selective disruption of the suppression layer by SPS and the gradients of suppressor concentration. Interestingly, the filling rate of Cu grown from the bottom with Br^- was 1.8–2.7 times

faster than that with I-. TSV filling in the presence of Br^- was completed after 500 s of electrodeposition, whereas a half of a TSV (55.6%) was filled with I^-. Based on these results, we hypothesized that the acceleration of TSV filling with Br^- might be due to (i) more effective inhibition on the top surface or (ii) a higher Faradaic efficiency for Cu electrodeposition.

The surface and cross section of TSV wafer after Cu electrodeposition for 500 s were investigated to clarify why Br^- filled TSVs more rapidly compared to I^- (Fig. 3.13). Since we accurately controlled number of TSVs for TSV filling to 2300, the comparison of thickness on the top surface would provide information on the efficiency of Cu electrodeposition with I^- and Br^-. When TSV filling was performed with I^-, the thickness of the Cu deposited on the top surface was 63 nm (Fig. 3.13(a)), whereas the thickness of Cu deposited with Br^- was 190 nm (Fig. 3.13(b)). This result signified that the suppression layer from Br^- was less effective for inhibiting Cu deposition on the top surface and to concentrating Cu deposition in the TSVs as shown in Fig. 3.11. Therefore, the promotion of TSV filling by Br^- was not related to the inhibition strength of Br^- on Cu electrodeposition, meaning hypothesis (i) was false.

Therefore, we calculated the total amount of Cu deposited in TSVs and on the top surface after 500 s to compare the Faradaic efficiency of Cu electrodeposition for Br^-

and I- cases and verify hypothesis (ii). The Faradaic efficiency with I^- was calculated to be 31% but 88% for Br^-. Even considering errors in the thickness measurement, this difference in efficiency was most likely to change the TSV filling speed. The low efficiency for I^- implied that a great many of electrons were consumed by undesired reaction. In our previous report, we found that I^- established the inhibition layer by electrochemically producing CuI on the top of the TSVs.[42, 52] The CuI films (or particles) on the top surface (white particles in the surface image, Fig. 3.13(a)) are not mechanically stable enough to bear the fluidic motion on the top surface. Furthermore, the CuI particles were observed in the electrolyte after the TSV filling experiments, and the remaining CuI on the substrate was easily washed out. Therefore, it is highly possible that the electrochemical formation of CuI and its detachment was continuously repeated during the TSV filling process with consuming a large amount of electrons.

In contrast, the inhibition effect of Br^- was not accompanied with the formation of CuBr films or particles. When 400 μM Br^- was added, the reduction potential of CuBr was calculated to be +0.035 V vs. Ag/AgCl (more positive than the TSV filling potential) from the Nernst equation, whereas CuI can be reduced at the potential more negative than -0.182 V.[81, 93-95] As a result, the CuBr would be immediately reduced to metallic Cu while CuI can be stable at the electrochemical conditions for TSV filling. Therefore, the

suppression effect of Br^- is more likely to be related to the establishment of PEG-PPG-Br^- layer (similar to polyether suppressor-Cl^- layers), not CuBr formation. As a result, the electrolyte with Br^- could maintain the high Faradaic efficiency of Cu electrodeposition; thereby increasing the TSV filling rate. The smooth Cu films without any particles after TSV filling (Fig. 3.13(b)) also supported that the suppression mechanism of Br^- is different from that of I^-.

We further investigated the change in the TSV filling profiles at 500 s as a function of the concentrations of Br^- (Fig. 3.14). When the Br^- concentrations were below 200 μM (Fig. 3.14(a) and 3.14(b)), TSV filling was not completed after 500 s, and the conformal profiles were observed. It was possible that seams were formed at the middle of TSVs, although they were not clearly observed in Fig. 3.10. On the contrary, when the concentration of Br^- was over 400 μM (Fig. 3.14(c) and 3.14(d)), defect-free filling was completed within 500 s. The bottom-up filling with superconformal profiles was already confirmed in Fig. 3.12.

The potential profiles during TSV filling show that filling process was concentration-dependent because of the saturation of the inhibition layer of Br^- on the top surface and near the opening of TSVs (Fig. 3.15). Since I^- clearly showed bottom-up filling in the previous research, the potential profiles for Br^- were compared to those for I^-. As shown

in Fig. 3.15(a), in the presence of I^-, the potential was stable throughout the TSV filling experiments, suggesting that the suppression layer of CuI on the top surface was not displaced by SPS even at 100 μM. Fig. 3.15(b) shows the potential profiles during the TSV filling with Br^-. The positive shift of the potential was observed between 100 and 1000 s when the concentration of Br^- was lower than 200 μM. This result suggested that the suppression layer of PEG-PPG and Br^- near the openings of TSVs was continuously displaced by SPS, since there was no significant increase in the active surface area for Cu deposition. On the contrary, when the concentration of Br^- was over 400 μM, the potentials were stable during the TSV filling experiments, and the completion of TSV filling was confirmed by the fluctuation of potential at 500 s (marked with arrows in Fig. 3.15(b). The stable potential profiles indicate that the suppression layer at this potential range was strong enough to inhibit its displacement by SPS. Therefore, it can be concluded that the saturation of PEG-PPG-Br^- suppression layer on the top surface by adding sufficient Br^- is essential to achieve the bottom-up filling of TSVs. Furthermore, it was found that a higher concentration of Br^- is necessary to achieve enough suppression effect for bottom-up filling than is needed for I^-, which is likely to be related to the different inhibition mechanisms of Br^- and I^-.

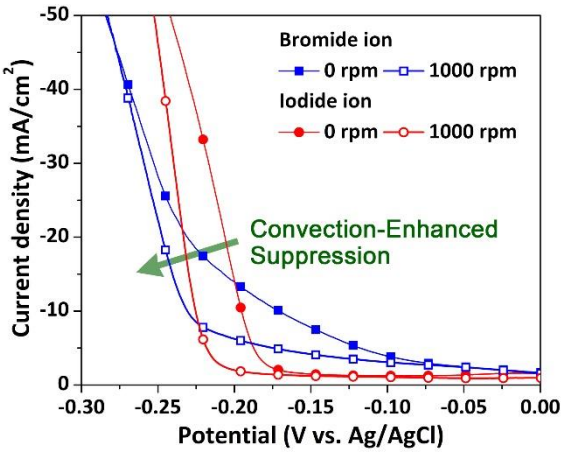

Figure 3.11. Linear sweep voltammograms for Cu^{2+} reduction in the presence of Br^- and I^-. The electrolyte consisted of 50 μM PEG-PPG, and 10 μM SPS, and the concentrations of both Br^- and I^- were 400 μM. The rotating speeds of the disk electrode were controlled to 0 and 1000 rpm to replicate the convection condition at the bottom and top of TSV, respectively.

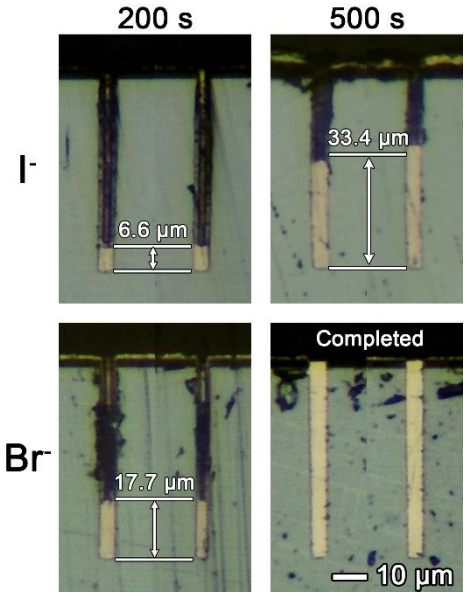

Figure 3.12. The cross-sectional profiles after Cu TSV filling for 200 and 500 s in the presence of I^- and Br^-. The concentrations of I^- and Br^- were 400 μM. The current density was 1 mA/cm^2, and the rotating speed of the substrate was fixed at 1000 rpm.

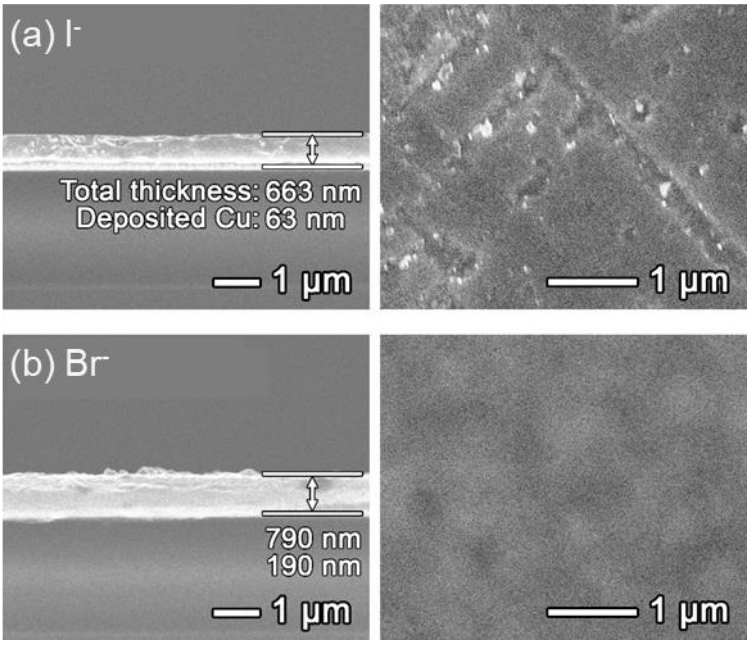

Figure 3.13. The cross-sectional and surface images of Cu films deposited after TSV filling experiment for 500 s in the presence of (a) I^- and (b) Br^-. These images were taken from the same samples shown in the right images of **Figure 3.12.**

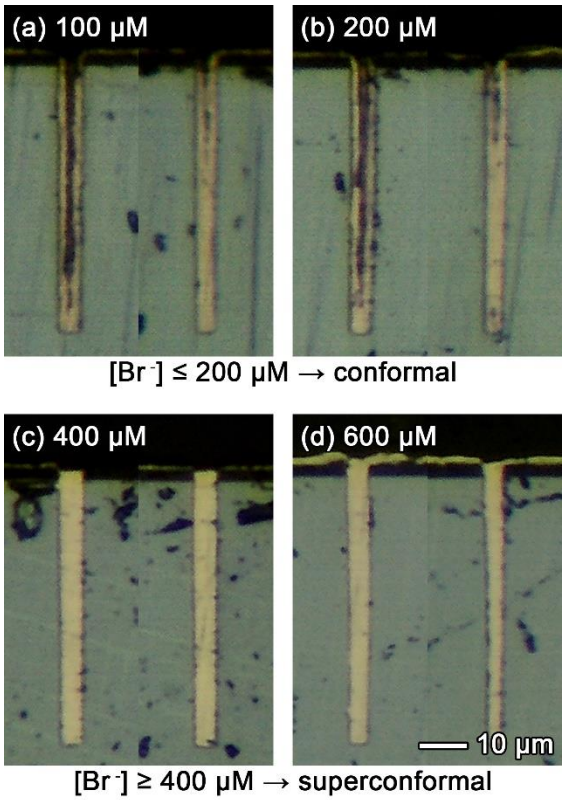

Figure 3.14. The TSV filling profiles after 500 s of Cu electrodeposition with the Br^- concentration of (a) 100, (b) 200, (c) 400, and (d) 600 μM. The electrolyte consisted of 50 μM PEG-PPG, and 10 μM SPS. The current density was 1 mA/cm^2, and the rotating speed of the substrate was fixed at 1000 rpm.

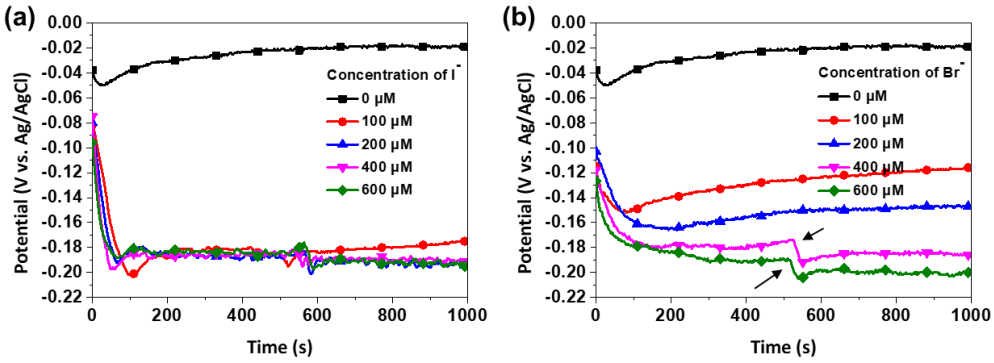

Figure 3.15. The potential profiles during TSV filling in the presence of (a) I^- and (b) Br^-. The corresponding TSV filling results are shown in **Figure 3.1 and 10**.

3.3. TSV filling in single additive system

In this study, a synthesized leveler containing two quaternary ammonium cations was used for TSV filling in a single additive system. A naphthalene ring was added to each quaternary ammonium cation of the leveler to obtain a strong suppression effect of the aromatic ring.[96-98] Moreover, we optimized the performance of the leveler by modifying its chain length using PEG of various molecular weights as the starting material (Fig. 3.16). Lev1, Lev600, and Lev1000 were synthesized from EG (n = 1), PEG600 (n = 12~15), and PEG1000 (n = 21~25), respectively. The TSV filling was performed and electrochemical behavior of the synthesized leveler with different chain length was systemically investigated.

3.3.1. TSV filling with synthesized additive

Figure 3.17 shows TSV filling profiles with the synthesized levelers after TSV filling for 1,000 s. In the case of Lev1, defect-free filling was achieved at large number of TSVs (Fig. 3.17(a)). However, some failures were also observed, such as interrupted TSV

filling and clogged TSV entrances. The filling ratio of the number of TSVs filled (72) to the total number of TSVs (108) was 68.5%. The filling ratio was significantly improved to 100% with Lev600, as shown in Fig. 3.17(b). No filling failures were found in the total of 82 TSVs. For Lev1000 with a long PEG chain length, only slight conformal deposition occurred, and TSV filling was no longer observed (Fig. 3.17(c)). This indicates that the PEG chain length of the synthesized leveler plays an important role in uniform TSV filling. On the other hand, PEG1000, without quaternary ammonium cations and naphthalene rings, resulted in the conformal deposition regardless of the presence of bromide ions (Figs. 3.17(d) and (e)). Similar filling profile was also obtained with PEG600. These results indicated that the functional groups of the synthesized levelers, quaternary ammonium cations and naphthalene rings, played an important role in changing the deposition profile in TSV filling.

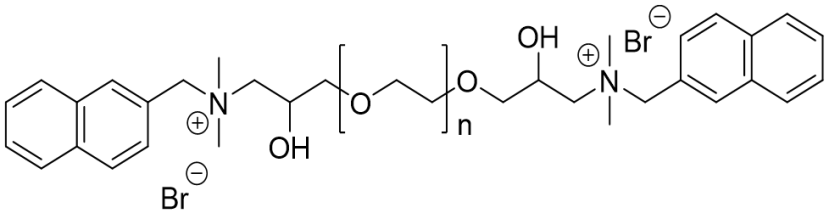

Figure 3.16. Organic structure of synthesized additives.

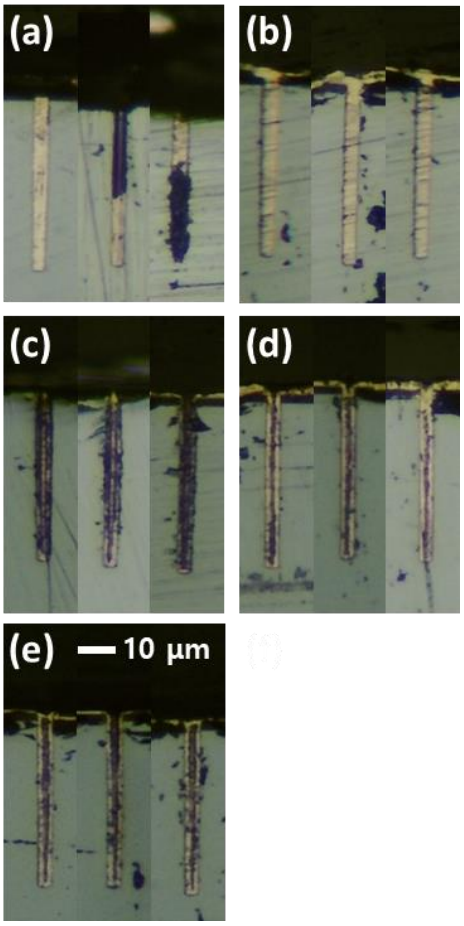

Figure 3.17. TSV filling profiles for 1000 s using 100 μM of (a) Lev1, (b) Lev600, (c) Lev1000, (d) 200 μM of NH_4Br, 100 μM of PEG1000, and (e) 100 μM of PEG1000.

3.3.2. Electrochemical analysis and filling mechanism

The electrochemical behavior of each leveler was investigated using LSV to demonstrate the effect of PEG chain length and functional groups at stationary (Figs. 3.18(a) and (b)) and convective conditions (Figs. 3.18(c) and (d)). The reduction current density of Cu ions was decreased by the addition of each leveler. As shown in Figs. 3.18(a) and (b), all synthesized levelers showed strong suppression of Cu deposition compared to Br^- + PEG1000 and PEG1000, indicating that the quaternary ammonium cations and naphthalene rings were effective in suppressing Cu deposition. The strength of the suppression until onset potential was in order of Lev1 > Lev600 > Lev1000 > Br^- + PEG1000 > PEG1000. It was also observed that the suppression effect of the synthesized leveler weakened slightly as the PEG chain length increased. For the synthesized levelers, the reduction current density increased sharply at the more negative potentials than -650 mV, which was the breakdown of the suppression layer. However, after the breakdown, the increase in current density with the applied potential decreased as the PEG chain length increased. This was the opposite of the suppression strength that

increased with the PEG chain length of the synthesized leveler. PEG1000 alone showed the weakest suppression effect. The addition of bromide ions with PEG1000 significantly enhanced the suppression effect, but still showed a weaker suppression compared to the synthesized leveler.[53] The electrochemical behaviors of PEG600 were similar to those of PEG1000, except that the suppression effect was weaker than PEG1000. Under convective condition, the suppression effect was enhanced overall by the convection, but the same tendency as in stationary condition was observed.

Figure 3.19 shows the LSV curves for each leveler under stationary and convective conditions before and after iR compensation. The convection-dependent adsorption (suppression) was observed in all levelers: the suppression effect was higher in the convective condition than in the stationary condition. However, TSV filling was failed with Lev1000, Br^- + PEG1000, or PEG1000 (Figs. 3.17(c) ~ (e)), while TSVs were filled with Lev1 or Lev600 (Figs. 3.17(a) and (b)). This difference can be explained by the shape of the LSV curve after iR compensation. In Figs. 3.19(a) and (b), clear negative differential resistance (NDR) profiles were obtained after iR compensation both at 0 rpm

and 1,000 rpm: the slope rapidly changed to negative at the points where the current densities were -3 mA/cm^2 (at -671 mV) and -10 mA/cm^2 (at -680 mV) for Lev1 and Lev600, respectively. The sharp change in slope at low current densities indicates that the surface state was rapidly switched from passive (suppressed) to active due to the instantaneous breakdown of the suppression layer formed by the leveler. In other words, the suppression layer composed of Lev1 or Lev600 remained stable up to a certain critical potential, and collapsed immediately when more negative potentials were applied. During Cu electrodeposition, this led the surface of the TSV structure to bifurcate into active and passive regions depending on different deposition conditions caused by the structure feature. Applied current is concentrated at the bottom of the TSVs by the preferential breakdown of the weakly formed suppression layer at the bottom, where the mass transfer is poor compared to the top.[99] Therefore, the active and passive regions become the bottom and top of the TSVs, respectively. Lev1 and Lev600 were able to effectively separate these two regions to achieve successful TSV filling. In the case of Lev1000, the slope change was rather gradual compared to Lev1 and Lev600, especially

at 1,000 rpm (Fig. 3.19(c)). The negative slope was observed at the current densities higher than 17 mA/cm^2, which indicated the breakdown of the suppression layer of Lev1000 was not instantaneous at the bottom of the TSVs. This resulted in TSV filling failure, though Lev1000 showed convection-dependent adsorption. In the case of Br^- + PEG1000 (Fig. 3.19(d)), NDR profiles were observed. However, the negative slopes were observed at higher current densities than 23 mA/cm^2 at both 0 rpm and 1,000 rpm, showing that the breakdown of the suppression layer was not instantaneous at both the top and the bottom of the TSV. This also led to TSV filling failure. PEG1000 alone did not show a NDR profile, as shown in Fig. 3.19(e), resulting in conformal deposition (Fig. 3.17(e)).

TSV filling mechanism of Lev1 and Lev600 was demonstrated by NDR profiles (suppression-breakdown). However, these LSV results were insufficient to explain the difference in TSV filling uniformity of the two additives. Figures 3.20(a) and (b) show CV curves for each leveler under stationary and convective conditions, respectively. During the CV measurement, the breakdown of the suppression layer (detachment of

adsorbed leveler) occurred in the negative potential sweep (forward scan) and then the leveler began to re-adsorb on the surface in the positive potential sweep (backward scan). In Fig. 3.20(a), the synthesized additives showed clear hysteresis. The hysteresis resulted from the slow re-adsorption of the leveler, which detached from the surface during the negative potential sweep: the slow re-adsorption rate of the leveler weakened the suppression effect and increased the reduction current density in the positive potential sweep. However, little hysteresis was observed when Br^- + PEG1000 or PEG1000 was added, indicating that PEG1000 quickly re-formed a suppression layer regardless of the applied potential and bromide ions. Therefore, it was concluded that the slow re-adsorption rate, a main cause of the hysteresis, was attributed to the synthesized levelers' functional groups (quaternary ammonium cations and naphthalene rings). The area of hysteresis is an indirect indication of how slow the re-adsorption rate of the leveler is. The hysteresis area of the synthesized additives was in the order of Lev1 > Lev600 > Lev1000. The hysteresis area became smaller as the PEG chain length of the synthesized leveler increased. This suggested that the PEG chain of the synthesized leveler

influenced the re-adsorption rate: the longer the length of the PEG chain, the faster the rate of re-adsorption. The functional groups of the leveler, quaternary ammonium cations and naphthalene rings, mainly enhanced the adsorption strength (suppression effect), but negatively affected the improvement of the re-adsorption rate.[53] Under the convection (Fig. 3.20(b)), hysteresis was reduced for all synthesized levelers. These results showed that the re-adsorption rate of the levelers was accelerated by the convection. However, the re-adsorption tendency of the synthesized levelers was the same as in the stationary condition. We supposed that the re-adsorption rate of the leveler affects the uniformity of TSV filling. At the initial stage of TSV filling, the deposition surface is bifurcated into active and passive regions (the bottom and top of the TSV, respectively) by the leveler. However, for some reasons, there may be local points where the suppression layer is not formed on the top surface, and Cu electrodeposition may not be suppressed at these points. Therefore, some areas of the top surface may be active, which can cause defects in TSV filling. From this point of view, a leveler with a fast re-adsorption rate can quickly recover the suppression layer at the top surface and reduce TSV filling

defects. Lev600, which exhibited a clear NDR profile, had a faster re-adsorption rate than Lev1. Therefore, the uniformity of TSV filling could be improved with Lev600.

In order to demonstrate the correlation between the re-adsorption rate of the leveler and the uniformity of TSV filling, the effect of the re-adsorption rate of the leveler on the Cu electrodeposition on top of TSV was investigated. Figure 3.21 shows the surface and cross-section images of the electrodeposited Cu films on the top surface of TSV, and the TSV filling profiles, after TSV filling for 500 s. As shown in Figs. 3.21(a)–(d), with Lev1, several Cu islands with tens of micrometers in width were observed on the top surface, while the electrodeposited Cu film thickness was only about 37 nm. The formation of the Cu islands indicates that the suppression effect by Lev1 was not applied locally due to the formation of a non-uniform suppression. As the re-adsorption rate of Lev1 was the slowest among the synthesized levelers, the recovery rate of the non-uniform suppression layer would be also the slowest. This hindered the deposition current from being concentrated at the bottom of the TSV, resulting in uneven TSV filling as shown in Fig. 3.17(a). It also reduced TSV filling efficiency, delaying TSV

filling time (Fig. 3.21(e)), which will be discussed later. However, no Cu island was observed on the top surface when Lev600 or Lev1000 was added (Figs. 3.21(f) and (h), Figs. 3.21(k) and (m)). The Cu film thicknesses were 136 nm and 156 nm for Lev600 and Lev1000, respectively, which were much thicker than that of Lev1 (Figs. 3.21(d), (i), (n)). These results showed that, compared to Lev1, the recovery rate of the non-uniform suppression layer became fast due to the fast re-adsorption rates of Lev600 and Lev1000, but the suppression effect itself weakened. Lev600, which showed a clear NDR profile and faster re-adsorption rate than Lev1, successfully bifurcated the deposition surface into active and passive regions, which were the bottom and top of the TSV, respectively, achieving uniform defect-free TSV filling. The TSV filling efficiency was also improved with Lev600. Figs. 3.21(e) and (j) are TSV filling profiles after TSV filling for 500 s with Lev1 and Lev600, respectively. Fully-filled TSVs were observed with Lev600, while only half-filled TSVs were obtained with Lev1. However, only small deposit was observed in TSVs when Lev1000 was used (Fig. 3.21(k)), though it also formed uniform suppression layer at the top surface (Figs. 3.21(k)-(n)). In the case of

Lev1000, the breakdown of suppression layer did not occur immediately compared to Lev1 and Lev600 due to the effect of long PEG chain (Fig. 3.19(c)). Therefore, the deposition current was less concentrated at the TSV bottom than Lev1 and Lev600, inducing conformal deposition.

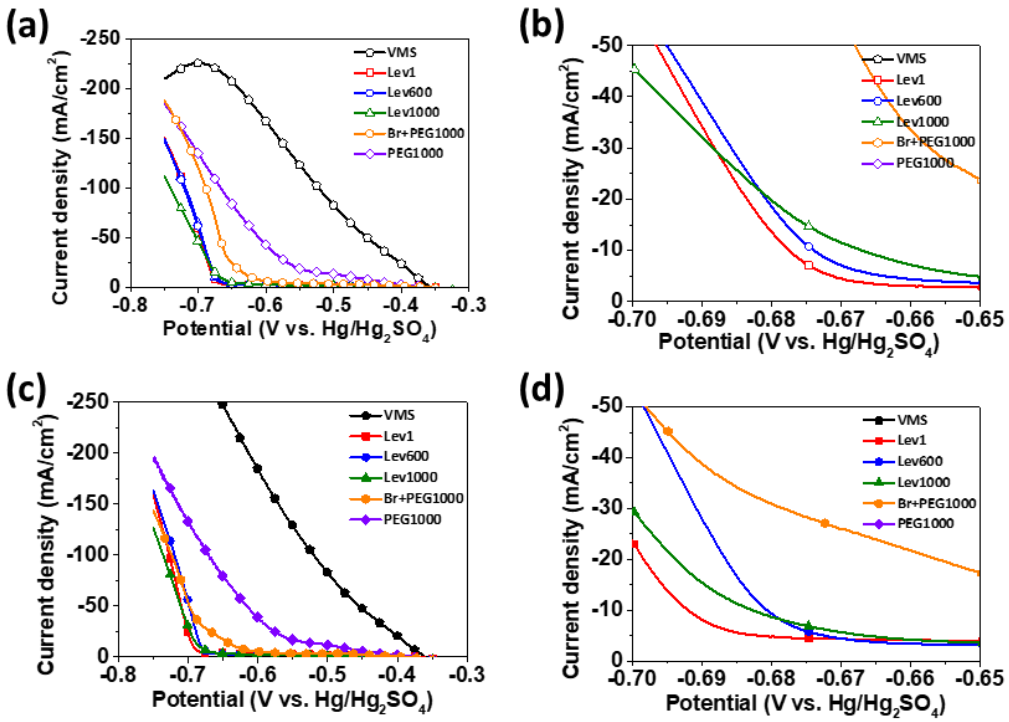

Figure. 3.18. LSV curves of Cu RDE in the additive-containing solutions under (a) stationary and (c) convective condition (1000 rpm). (b) and (d) are enlarged figures of (a) and (c), respectively. The concentration of additives was 100 μM of Lev1, Lev600, Lev1000, and PEG1000, and 200 μM of NH_4Br.

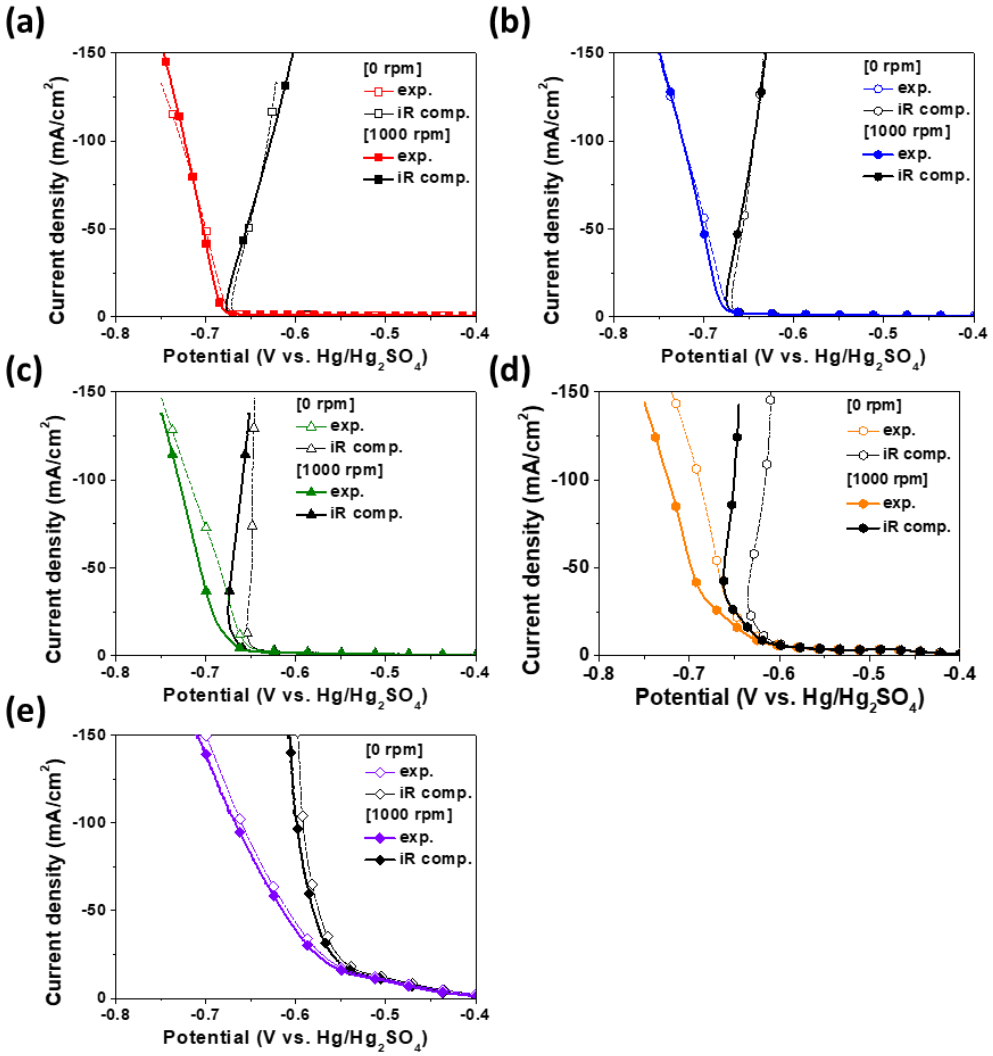

Figure. 3.19. iR compensation curves of LSV results in the additive-containing solutions under stationary and convective condition (1000 rpm), 100 μM of (a) Lev1, (b) Lev600, (c) Lev1000, (d) 200 μM of NH_4Br + 100 μM of PEG1000, and (e) 100 μM of PEG1000.

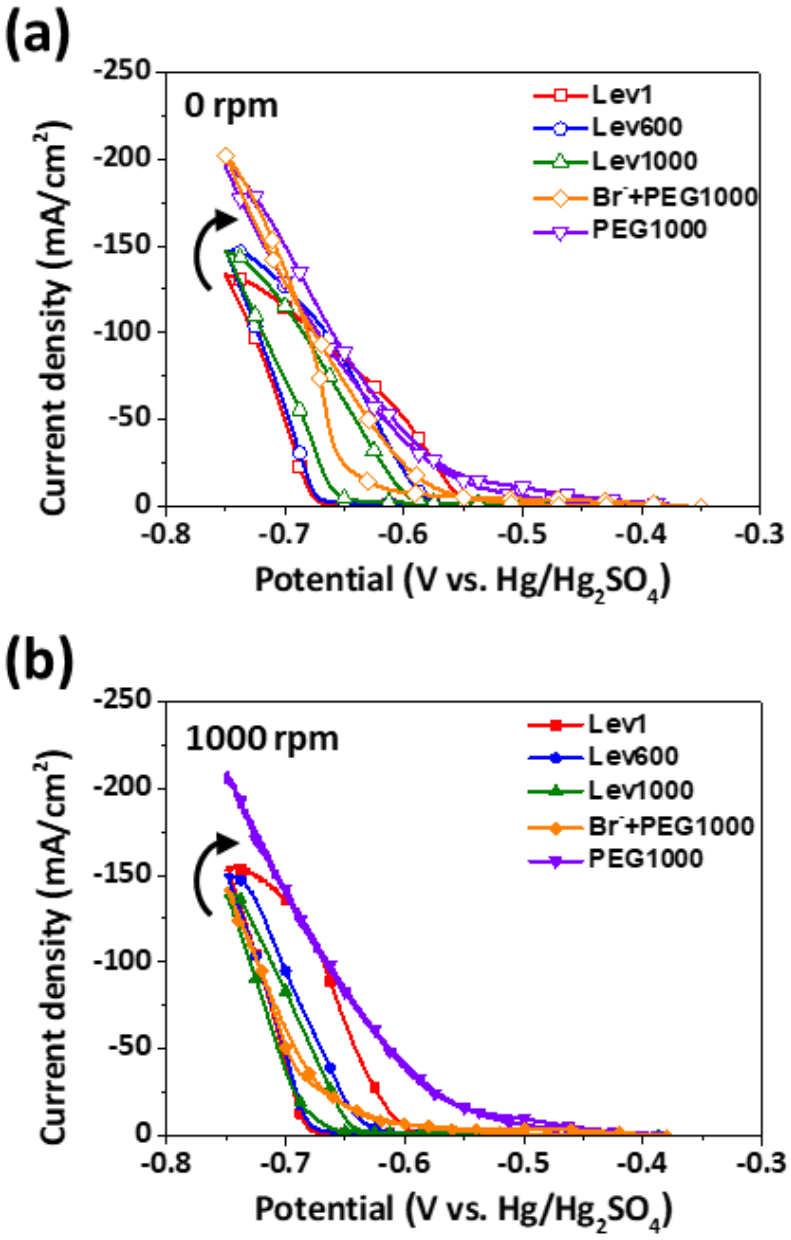

Figure. 3.20. CV curves of Cu RDE in the additive-containing solutions under (a) stationary and (b) convective condition. The concentration of additives were 100 μM of Lev1, Lev600, Lev1000, and PEG1000, and 200 μM of NH_4Br.

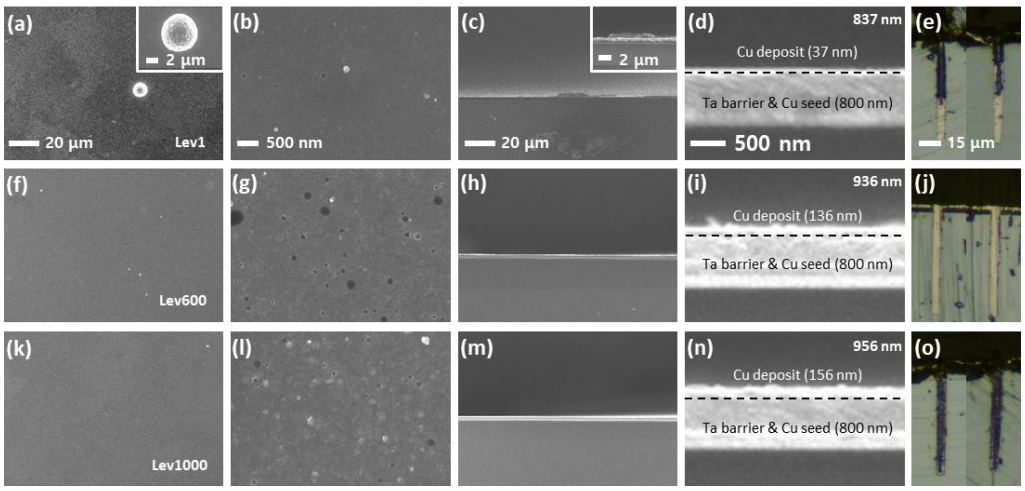

Figure. 3.21. Surface morphologies and cross-section image of the TSV-patterned wafers after TSV filling for 500 s containing (a)–(e) 100 μM Lev1, (f)–(j) 100 μM Lev600, and (k)–(o) 100 μM Lev1000. (b), (d), (g), (i), (l) and (n) are enlarged views of (a), (c), (f), (h), (k), and (m), respectively.

CHAPTER IV

Conclusion

In this study, various levelers were introduced, which were inorganic halide ions, iodide ions and bromide ions, and synthesized leveler containing quaternary ammonium cations and naphthalene ring. At first, the working mechanism of iodide ions and their effect on Cu microstructure in TSV filling were investigated. The iodide ions react with cupric and cuprous ions via both electrochemical and chemical pathways, forming CuI inhibition layer on the Cu surface. The formation of CuI is facilitated by convection and the presence of other additives, which increase the surface concentration of cuprous ions. Meanwhile, the formed CuI is also reduced to Cu electrochemically. The two opposing processes occur simultaneously, enabling defect-free TSV filling. However, the electrochemical reduction of CuI during the filling process results in small Cu grains. Therefore, a two-step filling was applied to promote the direct reduction of cupric ions rather than the CuI reduction. After the two-step filling, the grain size of Cu in TSV was increased by 690 %, and the enlarged grains reduced the degree of Cu protrusion by 47%.

In addition, bromide ions as an inorganic leveler for TSV filling was also investigated. The convection-dependent inhibition of bromide ions successfully induced bottom-up

filling of TSVs. Furthermore, bromide ions improved the stability of the suppression layer compared to iodide ions, leading to the acceleration of TSV filling. The Br-established suppression layer with a polymeric suppressor (PEG-PPG-Br^-) that was more stable than the CuI inhibition layer. The CuI layer continuously detached and regenerated during TSV filling and consumed additional electrons, decreasing the filling efficiency, whereas the Br^--based inhibition layer was unaffected by convection, achieving high Cu TSV filling efficiency. As a result, the addition of Br^- completed defect-free TSV filling in 500 s, which was half of the time needed by I^- at the same current density. Furthermore, since Br^- does not produce any decomposition product(s) during electrodeposition, the use of Br^- would be more beneficial for maintaining the performance of an electrodeposition bath than would other organic levelers be.

Synthesized additives containing quaternary ammonium cations and naphthalene rings as functional groups, were applied to TSV filling in a single additive system, and the filling mechanism were investigated. Suppression-breakdown, an important characteristic for TSV filling in a single additive system, was observed with the synthesized additives. The results show that TSV filling and its uniformity were highly dependent on the additive's chain length, and the chain length was found to affect the additive's suppression strength and re-adsorption rate. A trade-off between the suppression strength and re-adsorption

rate of the additive was found that as the chain length increased, the re-adsorption rate of the additive increased and its suppression weakened. Thus, by modifying the chain length of the synthesized additive, defect-free and uniform TSV filling in single additive system was successfully achieved utilizing Lev600**,** which was determined to have the optimum chain length.

References

1. P. C. Andricacos, C. Uzoh, J. O. Dukovic, J. Horkans and H. Deligianni, *IBM J. Res. Dev.*, **42**, 567 (1998).

2. J. G. Ryan, R. M. Geffken, N. R. Poulin and J. R. Paraszczak, *IBM Journal of Research and Development*, **39**, 371 (1995).

3. M. J. Kim, K. J. Park, T. Lim, O. J. Kwon and J. J. Kim, *Journal of The Electrochemical Society*, **160**, D3126 (2013).

4. M. J. Kim, H. J. Lee, S. H. Yong, O. J. Kwon, S.-K. Kim and J. J. Kim, *Journal of The Electrochemical Society*, **159**, D253 (2012).

5. G. Schneider, D. Hambach, B. Niemann, B. Kaulich, J. Susini, N. Hoffmann and W. Hasse, *Applied Physics Letters*, **78**, 1936 (2001).

6. IEDM, *IEEE International Electron devices Meeting* (2017).

7. IRDS, *International Roadmap for Devices and Systems*, 2018 (2018).

8. M. J. Kim, T. Lim, K. J. Park, O. J. Kwon, S.-K. Kim and J. J. Kim, *Journal of The Electrochemical Society*, **159**, D544 (2012).

9. M. J. Kim, T. Lim, K. J. Park, S. K. Cho, S.-K. Kim and J. J. Kim, *Journal of The Electrochemical Society*, **159**, D538 (2012).

10. M. J. Kim, T. Lim, K. J. Park, S.-K. Kim and J. J. Kim, *Journal of The Electrochemical Society*, **160**, D3081 (2013).

11. M. J. Kim, T. Lim, K. J. Park, S.-K. Kim and J. J. Kim, *Journal of The Electrochemical Society*, **160**, D3088 (2013).

12. J. U. Knickerbocker, P. S. Andry, B. Dang, R. R. Horton, M. J. Interrante, C. S. Patel, R. J. Polastre, K. Sakuma, R. Sirdeshmukh and E. J. Sprogis, *IBM Journal of Research and Development*, **52**, 553 (2008).

13. J. Tao, N. W. Cheung and C. Hu, *IEEE Electron Device Letters*, **14**, 249 (1993).

14. C.-K. Hu and J. Harper, *Materials Chemistry and Physics*, **52**, 5 (1998).

15. F. d'Heurle, *Metallurgical transactions*, **2**, 683 (1971).

16. L. Arnaud, G. Tartavel, T. Berger, D. Mariolle, Y. Gobil and I. Touet, *Microelectronics Reliability*, **40**, 77 (2000).

17. Y. Zhu, S. Ma, X. Sun, J. Chen, M. Miao and Y. Jin, *Microelectronic Engineering*, **117**, 8 (2014).

18. L. Kong, J. Lloyd, K. Yeap, E. Zschech, A. Rudack, M. Liehr and A. Diebold, *Journal of Applied Physics*, **110**, 053502 (2011).

19. A. Nguyen, K. Fealey, P. Reilly, G. Pattanaik, A. Gracias, F. Wafula, M. Flynn and J. Enloe, *Journal of Microelectronics and Electronic Packaging*, **12**, 43 (2015).

20. F. Inoue, Y. Harada, M. Koyanagi, T. Fukushima, K. Yamamoto, S. Tanaka, Z. Wang and S. Shingubara, *Electrochemical and Solid-State Letters*, **12**, H381 (2009).

21. J. J. Kelly, C. Tian and A. C. West, *Journal of the Electrochemical Society*, **146**, 2540 (1999).

22. J. J. Kim, S.-K. Kim and Y. S. Kim, *Journal of electroanalytical chemistry*, **542**, 61 (2003).

23. M. Matsuda, T. Takahashi, S. Yoshihara and M. Dobashi, *Transactions of The Japan Institute of Electronics Packaging*, **2**, 55 (2009).

24. T. Moffat, D. Wheeler and D. Josell, *Journal of The Electrochemical Society*, **151**, C262 (2004).

25. T. P. Moffat, D. Wheeler and D. Josell, *Journal of The Electrochemical Society*, **151**, C262 (2004).

26. M. Sung, H. C. Kim, T. Lim and J. J. Kim, *Journal of The Electrochemical Society*, **164**, D805 (2017).

27. S. Yoshihara, *ECS Transactions*, **41**, 1 (2012).

28. H. C. Kim, S. Choe, J. Y. Cho, D. Lee, I. Jung, W.-S. Cho, M. J. Kim and J. J. Kim, *Journal of The Electrochemical Society*, **162**, D109 (2015).

29. T. Moffat and D. Josell, *Journal of The Electrochemical Society*, **159**, D208 (2012).

30. M. Tan, C. Guymon, D. R. Wheeler and J. N. Harb, *Journal of The Electrochemical Society*, **154**, D78 (2007).

31. M. Walker, L. Richter and T. Moffat, *Journal of The Electrochemical Society*, **152**, C403 (2005).

32. M. L. Walker, L. J. Richter and T. P. Moffat, *Journal of The Electrochemical Society*, **153**, C557 (2006).

33. F. Wang, X. Ren, P. Zeng, H. Xiao, Y. Wang and W. Zhu, *Microelectronic Engineering*, **180**, 25 (2017).

34. F. Wang, P. Zeng, Y. Wang, X. Ren, H. Xiao and W. Zhu, *Microelectronic Engineering*, **180**,

30 (2017).

35. H. Xiao, F. Wang, Y. Wang, H. He and W. Zhu, *Journal of The Electrochemical Society*, **164**, D126 (2017).

36. D.-H. Jung, A. Sharma, K.-H. Kim, Y.-C. Choo and J.-P. Jung, *Journal of Materials Engineering and Performance*, **24**, 1107 (2015).

37. H. C. Kim, M. J. Kim, Y. Seo, Y. Lee, S. Choe, Y. G. Kim, S. K. Cho and J. J. Kim, *ECS Electrochemistry Letters*, **4**, D31 (2015).

38. S. C. Hong, W. G. Lee, W. J. Kim, J. H. Kim and J. P. Jung, *Microelectronics Reliability*, **51**, 2228 (2011).

39. S. Jin, S. Seo, S. Park and B. Yoo, *Microelectronic Engineering*, **156**, 15 (2016).

40. Q. Zhu, A. Toda, Y. Zhang, T. Itoh and R. Maeda, *Journal of The Electrochemical Society*, **161**, D263 (2014).

41. Q. Zhu, X. Zhang, C. Liu and H. Liu, *Journal of The Electrochemical Society*, **166**, D3006 (2019).

42. M. Sung, S.-H. Kim, H.-J. Lee, T. Lim and J. J. Kim, *Electrochimica Acta*, **295**, 224 (2019).

43. M. J. Kim, H. C. Kim and J. J. Kim, *J. Electrochem. Soc.*, **163**, D434 (2016).

44. M. J. Kim, Y. Seo, H. C. Kim, Y. Lee, S. Choe, Y. G. Kim, S. K. Cho and J. J. Kim, *Electrochim. Acta*, **163**, 174 (2015).

45. S.-M. Huang, C.-W. Liu and W.-P. Dow, *Journal of The Electrochemical Society*, **159**, D135 (2012).

46. D. Josell, D. Wheeler and T. Moffat, *Journal of The Electrochemical Society*, **159**, D570 (2012).

47. H. C. Kim, M. J. Kim and J. J. Kim, *Journal of The Electrochemical Society*, **165**, D91 (2018).

48. M. J. Kim, Y. Seo, J. H. Oh, Y. Lee, H. C. Kim, Y. G. Kim and J. J. Kim, *Journal of The Electrochemical Society*, **163**, D185 (2016).

49. J. Tang, Q. Zhu, Y. Zhang, X. Zhang, J. Guo and J. Shang, *ECS Electrochemistry Letters*, **4**, D28 (2015).

50. T. Hayashi, K. Kondo, T. Saito, M. Takeuchi and N. Okamoto, *Journal of The Electrochemical Society*, **158**, D715 (2011).

51. L. Yin, Z. H. Liu, Z. P. Yang, Z. L. Wang and S. Shingubara, *Transactions of the IMF*, **88**, 149 (2010).

52. M. Sung, A. Lee, T. Kim, Y. Yoon, T. Lim and J. J. Kim, *Journal of The Electrochemical Society*, **166**, D514 (2019).

53. M. Sung, Y. Yoon, J. Hong, M. J. Kim and J. J. Kim, *Journal of The Electrochemical Society*, **166**, D546 (2019).

54. D. Josell, L. A. Menk, A. E. Hollowell, M. Blain and T. P. Moffat, *Journal of The Electrochemical Society*, **166**, D3254 (2019).

55. D. Josell and T. Moffat, *Journal of The Electrochemical Society*, **165**, D23 (2018).

56. L. Menk, D. Josell, T. Moffat, E. Baca, M. Blain, A. Smith, J. Dominguez, J. McClain, P. Yeh and A. Hollowell, *Journal of The Electrochemical Society*, **166**, D3066 (2019).

57. T. Isono, S. Tachibana, T. Kawase and N. Omura, Google Patents (2014).

58. T. B. Richardson, Y. Zhang, C. Wang, V. Paneccasio Jr, C. Wang, X. Lin, R. Hurtubise and J. A. Abys, Google Patents (2010).

59. O. Kardos, D. A. Arcilesi and S. P. Valayil, Google Patents (1977).

60. M. Hayase and K. Otsubo, *Journal of The Electrochemical Society*, **157**, D628 (2010).

61. M. Hayase and M. Nagao, *Journal of The Electrochemical Society*, **160**, D3216 (2013).

62. Y. Yoon, H. Kim, T. Y. Kim, K. H. Lee, S. Choe and J. J. Kim, *Electrochimica Acta*, **339**, 135916 (2020).

63. L. Oniciu and L. Mureşan, *Journal of applied electrochemistry*, **21**, 565 (1991).

64. D. Roha and U. Landau, *Journal of The Electrochemical Society*, **137**, 824 (1990).

65. C. Madore and D. Landolt, *Journal of The Electrochemical Society*, **143**, 3936 (1996).

66. C. Madore, M. Matlosz and D. Landolt, *Journal of The Electrochemical Society*, **143**, 3927 (1996).

67. K. Kondo, Y. Suzuki, T. Saito, N. Okamoto and M. Takauchi, *Electrochemical and Solid-State Letters*, **13**, D26 (2010).

68. T. Hayashi, K. Kondo, T. Saito, N. Okamoto, M. Yokoi, M. Takeuchi, M. Bunya, M. Marunaka and T. Tsuchiya, *Journal of The Electrochemical Society*, **160**, D256 (2013).

69. J.-J. Sun, K. Kondo, T. Okamura, S. Oh, M. Tomisaka, H. Yonemura, M. Hoshino and K. Takahashi, *Journal of The Electrochemical Society*, **150**, G355 (2003).

70. O. Lühn, C. Van Hoof, W. Ruythooren and J.-P. Celis, *Electrochimica Acta*, **54**, 2504 (2009).

71. L. A. Menk, E. Baca, M. G. Blain, J. McClain, J. Dominguez, A. Smith and A. E. Hollowell, *Journal of The Electrochemical Society*, **166**, D3226 (2019).

72. T. Braun, D. Josell, M. Silva, J. Kildon and T. Moffat, *Journal of The Electrochemical Society*, **166**, D3259 (2019).

73. Z. Lei, L. Chen, W. Wang, Z. Wang and C. Zhao, *Electrochimica Acta*, **178**, 546 (2015).

74. S.-M. Huang, C.-W. Liu and W.-P. Dow, *Journal of The Electrochemical Society*, **159**, D135 (2011).

75. W.-P. Dow, C.-C. Li, Y.-C. Su, S.-P. Shen, C.-C. Huang, C. Lee, B. Hsu and S. Hsu, *Electrochimica Acta*, **54**, 5894 (2009).

76. T. Lu, F. Wang and Y. He, *Journal of The Electrochemical Society*, **163**, D663 (2016).

77. D. Josell and T. P. Moffat, *Journal of The Electrochemical Society*, **160**, D3035 (2013).

78. D. Josell and T. P. Moffat, *Journal of The Electrochemical Society*, **163**, D322 (2016).

79. D. Josell and T. P. Moffat, *Journal of The Electrochemical Society*, **164**, D327 (2017).

80. D. Josell, M. Silva and T. P. Moffat, *Journal of The Electrochemical Society*, **163**, D809 (2016).

81. K. Doblhofer, S. Wasle, D. M. Soares, K. G. Weil, G. Weinberg and G. Ertl, *Zeitschrift für Physikalische Chemie*, **217**, 479 (2003).

82. D. Tromans and J. C. Silva, *Journal of The Electrochemical Society*, **143**, 458 (1996).

83. V.-H. Hoang and K. Kondo, *Journal of The Electrochemical Society*, **164**, D564 (2017).

84. M. L. Walker, L. J. Richter and T. P. Moffat, *Journal of The Electrochemical Society*, **152**, C403 (2005).

85. S. Barnes, *Electrochimica Acta*, **5**, 79 (1961).

86. E. Budevski, *Journal of crystal growth*, **13**, 93 (1972).

87. R. Winand, *Hydrometallurgy*, **29**, 567 (1992).

88. S.-C. Chang, J.-M. Shieh, B.-T. Dai, M.-S. Feng and Y.-H. Li, *Journal of The Electrochemical Society*, **149**, G535 (2002).

89. M. Stangl, M. Liptak, A. Fletcher, J. Acker, J. Thomas, H. Wendrock, S. Oswald and K. Wetzig, *Microelectronic Engineering*, **85**, 534 (2008).

90. G.-K. Liu, S. Zou, D. Josell, L. J. Richter and T. P. Moffat, *The Journal of Physical Chemistry C*, **122**, 21933 (2018).

91. O. M. Magnussen, *Chemical Reviews*, **102**, 679 (2002).

92. A. V. N. Tran, H. V. Hoang, T. Hirato and K. Kondo, *J. Surf. Finish. Soc. Jpn.*, **69**, 352 (2018).

93. T. Aben and D. Tromans, *Journal of The Electrochemical Society*, **142**, 398 (1995).

94. M. J. Muñoz-Portero, J. García-Antón, J. L. Guiñón and V. Pérez-Herranz, *CORROSION*, **60**, 749 (2004).

95. D. Tromans and J. C. Silva, *Journal of The Electrochemical Society*, **143**, 458 (1996).

96. J. J. Hatch, M. J. Willey and A. A. Gewirth, *Journal of The Electrochemical Society*, **158**, D323 (2011).

97. S. Ren, Z. Lei and Z. Wang, *Journal of The Electrochemical Society*, **162**, D509 (2015).

98. Y. Yamada, K. Kondo, M. Takeuchi, N. Okamoto, T. Saito, M. Bunya and Y. Yokoi, *ECS Transactions*, **58**, 97 (2014).

99. H. Xiao, H. He, X. Ren, P. Zeng and F. Wang, *Microelectronic Engineering*, **170**, 54 (2017).

국문 초록

실리콘 관통 전극(TSV)는 3차원 웨이퍼/칩 적층 공정에서 가장 중요한 기술 중의 하나로 꼽힌다. 이 연구에서는 무기 할라이드 평탄제, 4차 암모늄 및 나프탈렌 고리를 가진 합성 평탄제 등 다양한 첨가제들을 활용하여 TSV (깊이: 60 μm, 지름: 5 μm) 를 결함없이 채웠으며, 해당 평탄제들의 채움 메커니즘을 규명하였다. 우선 아이오딘 이온의 TSV 채움 메커니즘을 전기화학적인 분석 방법들을 통해 확인하였으며, 그 결과 이 이온은 아이오딘화 구리라는 안정한 물질을 전극 표면에 형성함으로써 구리 도금을 억제 하는 것을 확인하였다. 아이오딘 이온의 이러한 억제 작용을 통해 TSV를 바닥 차오름 형태로 결함없이 채울 수 있었다. 더 나아가 전류를 2단계에 걸쳐 가함으로써, 아이오딘화 구리의 억제 작용을 줄이고 구리 이온의 직접적인 도금을 증가시킴으로써 TSV 내부의 구리 결정의 크기를 크게 형성할 수 있었고, 구리 돌출 현상 역시 크게 줄어들었다.

하지만 이러한 아이오딘화 구리의 형성과정에서 전자의 소모가 발생하기 때문에, 구리 도금을 진행할 때 도금 효율이 크게 감소한다는 문제점이 발견되었다. 아이오딘화 구리는 웨이퍼 표면에 불안정하게 흡착해 쉽게 떨어지게 되며, 이로 인해 초기 억제층을 형성하기 위한 전자 소모

이후에도 도금 과정 동안 지속적으로 전자를 소모하게 된다. 이러한 문제를 가진 아이오딘 이온의 대안으로써 브로민 이온에 대한 연구가 진행되었다. 브로민 이온은 아이오딘 이온보다 더 약하게 구리 도금을 억제했지만, 브로민 이온이 형성한 억제층은 아이오딘화 구리보다 안정적으로 전극 표면에 유지되는 것을 관찰했다. 그 결과 구리 도금의 효율이 크게 향상되었으며, 공정 시간 역시 기존의 1000 초에서 500 초로 크게 단축시킬 수 있었다.

무기 첨가제와 더불어, 단일 첨가제 조성에서도 TSV 를 효과적으로 채울 수 있는 유기 첨가제에 대한 연구도 진행하였다. 폴리 에틸렌 글라이콜(polyethylene-glycol, PEG)을 기반으로 4차암모늄 이온과 나프탈렌 고리를 포함한 이 평탄제는, 단일 첨가제 조성에서 바닥 차오름 현상을 유도하였으며, 이를 통해 TSV를 성공적으로 채울 수 있었다. 하지만 다른 첨가제와의 상호 작용이 없고, 흡착력이 너무 강해 TSV가 균일하게 차지 않는 문제가 발생하였다. 이 문제를 평탄제의 사슬 길이를 조절함으로써 해결하고자 하였고, 그 결과 TSV채움의 균일도를 향상시킬 수 있었다. 전기 화학 분석을 통해 사슬 길이와 재흡착 속도, 대류 조건의 연관성을 밝혔으며, 이로 인해 TSV의 위치에 따른 재흡착 속도의 차이로 인한 억제 세기의 차이로 바닥 차오름이 유도되는 것을 확인하였다. 따라서, 적절한

길이의 사슬 길이를 가진 합성 평탄제를 사용함으로써, TSV를 결함없이 균일하게 채울 수 있었다. 또한, 평탄제의 강한 억제를 기반으로 도금의 선택도를 향상시켜 공정 시간을 450 s까지 줄일 수 있었다.

주요어: 실리콘 관통 비아, 구리, 전해도금, 평탄제, 무기 할라이드 평탄제, 합성 평탄제, 단일 첨가제 조성, 수퍼필링

학 번: 2015-22833

Appendix I

Effects of Organic Additives on Grain Growth in Electrodeposited Cu Thin Film during Self-Annealing

It was examined that additives influenced to microstructure of Cu in TSV in Chapter 3.1.4. In this Chapter, pre-research was conducted to investigate the effect of additives on the properties of Cu deposit.

1. Introduction

Copper (Cu) is widely used as a metallization material because of its superior properties, high electromigration resistance, and a low electrical resistivity.[1-4] Thus, various Cu-electrodeposition methods for metallization have been studied with the use of organic additives, or with the control of current/potential profiles such as pulse/pulse-reverse depositions.[5-14] The microstructures of the Cu deposits, such as the

grain size, texture, and grain-size distribution, have been extensively investigated by many research groups such as interuniversity microelectronics centre, because they exert a strong influence on the resistivity and reliability of the Cu interconnects.[15-21] The final microstructure of the Cu deposit is determined after the self-annealing in which the relaxation of the accumulated defect energy within the deposit occurs. Self-annealing is usually observed in electrodeposited films because electrodeposition generates various defect sites that originate from the impurities in the deposition electrolyte.[20-22]

In particular, organic additives are used to obtain the preferred deposition profiles and/or the deposition properties that strongly affect the self-annealing process.[23, 24] In Cu metallization, organic additives are essential because they can control the local deposition rate through an adsorption on the to-be-deposited surface, thereby inducing a void-free filling of, for example, the damascene structure. Polyethylene glycol (PEG) and bis-(3-sulfopropyl) disulfide (SPS) are a representative suppressor and accelerator in Cu electrodeposition, respectively. The combinations of PEG and SPS are widely

used in Cu metallization for the void-free filling of vias and trenches in damascene structures.[5-10] The adsorption of these organic additives on the surface alter the deposition rate and disturb the surface diffusion of the Cu ions, both of which determine the grain-growth mechanism. Therefore, revealing the effects of organic additives on the grain growth during the self-annealing is important for the improvement of the film properties in Cu electrodeposition. Although the adsorption mechanisms and effects of these additives during the Cu electrodeposition have been studied extensively, there are few detailed studies on the effect of the additives on microstructural evolution during self-annealing. Most of previous studies reported the additive effect on self-annealing by simply showing the resultant microstructure of Cu interconnects.[18, 25-27]

Herein, the relation between the microstructural evolution and the organic additives in electrodeposited Cu films during self-annealing are investigated in depth as a basic research study before the study of the microstructural changes in three-dimensional (3D) metallization. The investigation is mainly based on the crystallographic

observation of the microstructural evolution during the self-annealing.

2. Experimental

The Cu electrodeposition was performed using a standard electrolyte composed of 0.25 M $CuSO_4$, 1.0 M H_2SO_4, and 1.0 mM of HCl. Organic additives, 50 μM of SPS and/or 50 μM of PEG (MW: 3400), were also added to the standard electrolyte. As electrochemical analysis was conducted in a three-electrode system. A Cu rotating-disk electrode (RDE, 0.196 cm^2) was used as the working electrode, and an electronic-grade Cu rod and a silver/sliver chloride (Ag/AgCl) electrode (KCl saturated) were the counter and reference electrodes, respectively. Chronoamperometry was performed by applying -200 mV (vs. Ag/AgCl) to the working electrode with different additive concentrations under rotation at 300 rpm. The applied charge is 2000 mC/cm^2, which is the value for the deposition of 1-μm-thick Cu film on the assumption that the Coulombic efficiency is 100%. The Cu was also electrodeposited on a Cu-seeded blanket-coupon wafer [Cu (60 nm, physical vapor deposition (PVD))/Ta (7.5 nm, PVD)/TaN (7.5 nm, PVD)/SiO_2]

for the observation of the microstructures of the deposited Cu films. The native oxide on the surface of the Cu-blanket wafer was removed by using an aqueous solution of 0.02 M citric acid and 0.03 M KOH before the electrodeposition. All of the electrodeposition was conducted with a PAR 263A potentiostat (EG&G, Princeton Applied Research Corporation, United States) at 25˚C.

The microstructural changes of the deposited Cu films during the self-annealing were observed for 11 days after deposition. The crystallographic orientations of the Cu films were examined using X-ray diffractometry (XRD; D8 Advance, Bruker, United States) with a Cu Kα1 X-ray source (0.154 nm). The scan rate is 3°/min for the two-theta range of 30°–60°. The grain size was calculated using the Scherrer equation with the full width at half maximum (FWHM) values of the Cu(111) and Cu(200) diffraction peaks after the removal of the instrument error (0.0513°), which was measured using the standard reference material 660a, LaB_6, provided by the National Institute of Standards and Technology. The measured FWHM values were then further corrected considering the peak broadening effect that is induced by the diffractometer. The XRD (X'pert Pro,

PANalytical, The Netherlands) with the Cu Kα1 X-ray source was used to analyze the residual stress and the crystal imperfection. The residual stress was measured using the grazing-incident method that was performed at an omega 1° of the incident X-ray angle, and the crystal imperfection was examined using the FWHM values of Cu(111) that had been measured using the rocking-curve analysis. The electron back-scattered diffraction (EBSD; TexSEM Laboratory, United States) and the scanning electron microscope (SEM; SU70, Hitachi, Japan) were used to observe the changes of the misorientation and the grain size according to the self-annealing time. The step size for the EBSD analysis is 17 nm, and the samples for the EBSD analysis were prepared using a focused ion beam (FIB; SMI3050SE, SII Nanotechnology, United States).

3. Results and Discussion

Linear sweep voltammetry (LSV) and chronoamperometry (CA) were conducted to identify the electrochemical behaviors of the additives on the Cu reduction. As shown in Fig. 1 (a), the Cu reduction current was increased slightly by the SPS, whereas it was

decreased in the presence of the PEG. These behaviors show the acceleration effect of the SPS and the suppression effect of the PEG on the Cu reduction. The acceleration effect of the SPS was observed distinctly when the SPS and PEG were co-present. Fig. 1 (b) shows the current profiles of the film depositions with different combinations of additives at -200 mV (vs. Ag/AgCl). The same additive effects were observed, as shown in Fig. 1 (a). In particular, in the PEG-SPS system, the gradual increase in the current density indicated the displacement of a pre-adsorbed PEG layer by the SPS: The SPS gradually displaces the PEG layer gradually during the deposition, thereby accelerating the Cu reduction process.[7-10]

The microstructures of the Cu films deposited with the organic additives were observed using FIB after 11 days of self-annealing (Fig. 2). The decrease of the apparent grain size was observed with the addition of either PEG (F_{PEG}) or SPS (F_{SPS}) when it was compared with that of the Cu film without the additive (F_{free}), and only a slight difference in the grain size between the F_{PEG} and the F_{SPS} was observed. Meanwhile, relatively large grains were observed when both the PEG and the SPS were added together ($F_{PEG-SPS}$).

This result demonstrates that the organic additives influence the final microstructure of the electrodeposited films after the self-annealing.

The crystalline-structure change of the Cu films during the self-annealing was examined using XRD (Fig. 3). As only Cu(111) and Cu(200) diffraction peaks were detected from the electrodeposited Cu films, those diffraction peaks were characterized separately. Other Cu orientations were also detected using the pole figure and the grazing incident (not shown here), indicating that the Cu films were randomly oriented and their preferred orientation is Cu(111).

As shown in Fig. 3 (a), the Cu(111) intensity of the as-prepared $F_{PEG\text{-}SPS}$ decreased by 75% compared with the value of the as-prepared F_{free}, while those of the as-prepared F_{SPS} and F_{PEG} decreased by 10% and 40%, respectively. In general, the formation of Cu (111) is preferred in thin films whose thickness is less than a few micrometers.[28-31] In the thin film, the surface energy is generally larger than the strain energy, so the surface-energy minimization is a more dominant factor in the determination of the film texture than the strain-energy minimization. The formation of Cu(111) is an effective way to reduce the

surface energy. However, the adsorption of either the deposition of SPS or PEG on the surface disturbs the surface diffusion of the Cu ions, thereby suppressing the development of the preferred orientation, Cu(111). The decrement in the Cu(111) intensity of the F_{PEG} was larger than that of the F_{SPS}, indicating that the PEG impedes the growth of the Cu(111) more effectively compared with the SPS. It has been reported that the adsorption of PEG of a high molecular weight requires a large adsorption site and that adsorbed PEG forms a stronger complex with Cl^- on the surface compared with the SPS.[9, 10, 32, 33] Therefore, it is likely that the adsorption of the PEG disturbs the surface diffusion of the Cu ions to a greater extent than the SPS. In the two-additive system of the PEG and the SPS, the competitive adsorptions of the PEG and the SPS strongly blocks the surface diffusion of the Cu ions, and the displacement between these additives changes the growth condition over time. Both effects disrupt the formation of the highly oriented crystalline structure of Cu(111), resulting in the largest decrement of the Cu(111) intensity. After the film deposition, the Cu(111) intensity increased at all of the films as the self-annealing was proceeded to further minimize the surface energy that had

accumulated in the films during the electrodeposition. The Cu(111) intensities of the F_{free}, F_{SPS}, and F_{PEG} increased by 10%, and the increase was terminated within 3 days. However, that of the $F_{PEG\text{-}SPS}$ increased by 100% for 7 days. The same trend was observed in the Cu(111) grain size that was calculated using the Scherrer equation,[34, 35] as shown in Fig. 3 (b). The accuracy of the quantitative analysis of the grain size via the Scherrer equation is slightly doubtful because a peak broadening is related to the crystal imperfections of films like the substructure and the dislocation as well as the grain size.[34-37] However, the considerable increase in the grain size was clearly observed at the $F_{PEG\text{-}SPS}$. The drastic growth of the Cu(111) grains in the $F_{PEG\text{-}SPS}$ after the self-annealing was induced by a high defect energy including both the surface energy and the strain energy, which will be discussed further in this study.

As presented in Figs. 3 (c) and (d), the Cu(200) diffraction peak was observed at the $F_{PEG\text{-}SPS}$ during the self-annealing. The formation of Cu(200) indicates that the appreciable strain energy that accumulated during the electrodeposition was relieved because Cu(200) exhibits the lowest strain energy in a thin film.[38, 39] The strain energy

was attributed to the competitive absorption and displacement between the PEG and the SPS. The displacement continuously changes the condition of the electrodeposition for each grain over time, preventing the highly preferred orientation of its microstructure from being realized.

The grain size that is calculated using the Scherrer equation is generally smaller than the actual grain size due to the film's crystal imperfection, and the gap between the two values is broadened as the actual grain size increases because the substructures barely grow larger than 200 nm.[37] Therefore, the actual grain size over several hundreds of nanometers results in a large deviation from the calculated value. The microstructures of the F_{free} and the $F_{PEG\text{-}SPS}$ were examined using the EBSD to observe the microstructural evolution directly during the self-annealing. It was not possible to observe the drastic microstructural change of the $F_{PEG\text{-}SPS}$ before 1 day due to the time interval between the sample preparation and its analysis. As shown in Figs. 4 (a) and (g), the apparent grain size of the $F_{PEG\text{-}SPS}$ is larger than that of F_{free} even after just 1 day of the self-annealing due to the drastic grain growth; although, the deposition condition of the $F_{PEG\text{-}SPS}$ is the

same as that of the F_{free} with the exception of the presence of additives. The grain growth of the $F_{PEG\text{-}SPS}$ was still observable after 1 day of self-annealing while that of the F_{free} was rarely changed, as shown in Figs. 4 (a)–(c) and Figs. 4 (g)–(i). During the self-annealing, twin boundaries that are denoted as red lines in Figs. 4 (d)–(f) and (j)–(l) were also detected. More twin boundaries were formed at the $F_{PEG\text{-}SPS}$ than the F_{free} even though the total length of the grain boundaries of the $F_{PEG\text{-}SPS}$ is shorter than that of the F_{free}, as shown in Figs. 4 (d)–(f) and (j)–(l). Twin boundary is a type of dislocations induced by stress, which is an indicator that shows that considerable stress is applied to film. As a twin boundary has the lowest grain-boundary energy,[40] the formation of twin boundaries can also reduce the total defect energy that accumulates in the $F_{PEG\text{-}SPS}$. These twin boundaries diminished gradually with the grain growth in both of the films as the self-annealing proceeded.

The drastic grain growth in the $F_{PEG\text{-}SPS}$ during the self-annealing occurs to reduce the strain energy as well as the surface energy. The relaxation of the strain energy by the grain growth was characterized by measuring the film stress that had accumulated at the

films. Fig. 5 shows the residual stress of the electrodeposited films with different additives before and after the self-annealing. The as-prepared films exhibited a similar stress (140 MPa), except for the $F_{PEG\text{-}SPS}$. The independent PEG or SPS exerted a negligible influence on the film stress because the Cu ions were reduced on a surface that was uniformly covered by a single additive during the electrodeposition: the condition of the surface that was being deposited upon is spatially and timely identical. However, the relatively high stress (250 MPa) was accumulated at the $F_{PEG\text{-}SPS}$. In this case, the adsorption state of the two additives and the deposition rate changed continuously due to the dynamic interaction of these additives. As the deposition condition varied with space and time during the deposition, the formation of a misorientation, which mainly attributes to film stress, is highly probable. After the completion of the self-annealing, the stress of the $F_{PEG\text{-}SPS}$ decreased by 40%, while those of the others increased by 9–12%. According to Chaudhari's model, grain growth generally causes film stress because of the volume shrinkage of the grain boundaries,[41] which can demonstrate the increase of the film stress after the self-annealing in the Cu

films, with the exception of the $F_{PEG\text{-}SPS}$. However, the stress in the $F_{PEG\text{-}SPS}$ was rather decreased to 156.5 MPa. In this case, the high strain energy that had accumulated in the as-prepared $F_{PEG\text{-}SPS}$ was relieved by the drastic grain growth that accompanied the reduction of the total grain boundaries (Fig. 3 (b)). Since the largest amount of the grain boundaries among the films was found in the as-prepared $F_{PEG\text{-}SPS}$ (the smallest average grain size), the elimination of the grain boundaries that hold a huge amount of strain energy is an efficient way to reduce the overall strain energy.[28-30, 42, 43] The relatively small strain energy, caused by the volume expansion of the drastic grain growth, then induced the formation of Cu(200), as shown in Fig. 3 (c).[38, 39] That is, the overall strain energy of the as-prepared $F_{PEG\text{-}SPS}$ was alleviated by the dissipation of the grain boundaries and the formation of Cu(200) during the self-annealing.

The drastic grain growth in the $F_{PEG\text{-}SPS}$ was caused by the high stress that had accumulated during the electrodeposition. The rocking curve was used to investigate the origin of the stress in the as-prepared films and the FWHM values of the rocking curves are shown in Fig. 6. The FWHM value is proportional to the crystal imperfection, which

is the number of Cu(111) grains that are not parallel to the preferred orientation. The tilted grains lead to the increase of the defect energy. The FWHM values of the rocking curve are in the sequential order of $F_{PEG\text{-}SPS} > F_{SPS} > F_{free} > F_{PEG}$ in the as prepared states; however, the order was changed to $F_{SPS} > F_{free} > F_{PEG} > F_{PEG\text{-}SPS}$ after the completion of the self-annealing. After the self-annealing, the FWHM value of the $F_{PEG\text{-}SPS}$ decreased by 25%, while those of the other films decreased slightly to less than 3%. This decrease indicates that the grain growth occurred to reduce the number of grains with the Cu(111)-orientation tilting based on the normal direction of the substrate during the self-annealing, thereby reducing the defect energy. In the case of the $F_{PEG\text{-}SPS}$, the drastic grain growth resulted in a significant decrease of the FWHM value. When a film is electrodeposited, the growth types of the grains vary with the deposition conditions. When the deposition rate is fast, grains exhibit various crystalline orientations,[23, 44-46] because the increase of the deposition rate suppresses the surface diffusion of the Cu ions, which is for finding energetically stable sites where they can be deposited. Therefore, the FWHM value of the rocking curve must increase. As shown in Fig. 6, the FWHM values of the as-

prepared films showed the same tendency with the deposition current density except for the $F_{PEG\text{-}SPS}$ that is shown in Fig. 1 (b). The PEG or SPS alone only affects the deposition rate without changing the Cu reduction mechanism. Therefore, the film was electrodeposited via a two-dimensional nucleation of the macrosteps in the absence of an additive or the presence of a single additive, as shown in Fig. 7 (a). This type of film deposit is called field-oriented texture type (FT type).[23, 44, 47] In these cases, the deposition current density is the only factor that affects the formation of the preferred orientation. However, the $F_{PEG\text{-}SPS}$ showed different tendency. Although the deposition current density for the $F_{PEG\text{-}SPS}$ is smaller than that for the F_{free} or the F_{SPS}, it has the largest FWHM value among these films. When both the PEG and the SPS are present, the two additives are adsorbed on the surface competitively, creating various local deposition conditions on the surface. In addition, the SPS simultaneously displaces the pre-adsorbed PEG at the same time. This dynamic situation results in an unoriented dispersion (UD) type in which a film grows via 3D nucleation, and the crystal imperfection of the film increases as shown in Fig. 7 (b).[23, 44, 47] Therefore, a high stress

is accumulated by the formation of a high-angle misorientation under the effect of both additives. This energy induced the drastic grain growth of the $F_{PEG\text{-}SPS}$ during the self-annealing.

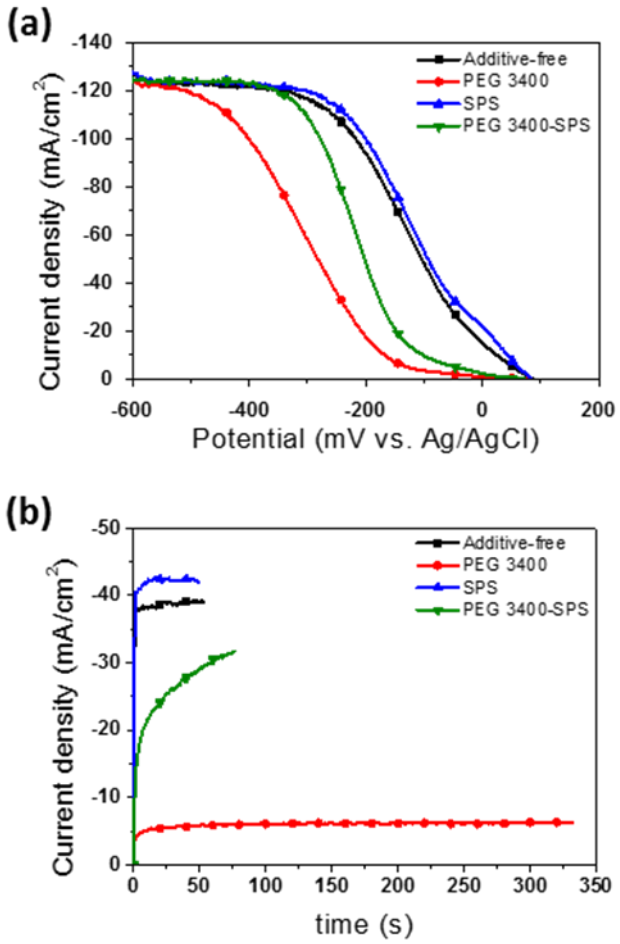

Figure 1. (a) Linear sweep voltammogram and (b) current-time curve of the Cu reduction with organic additives.

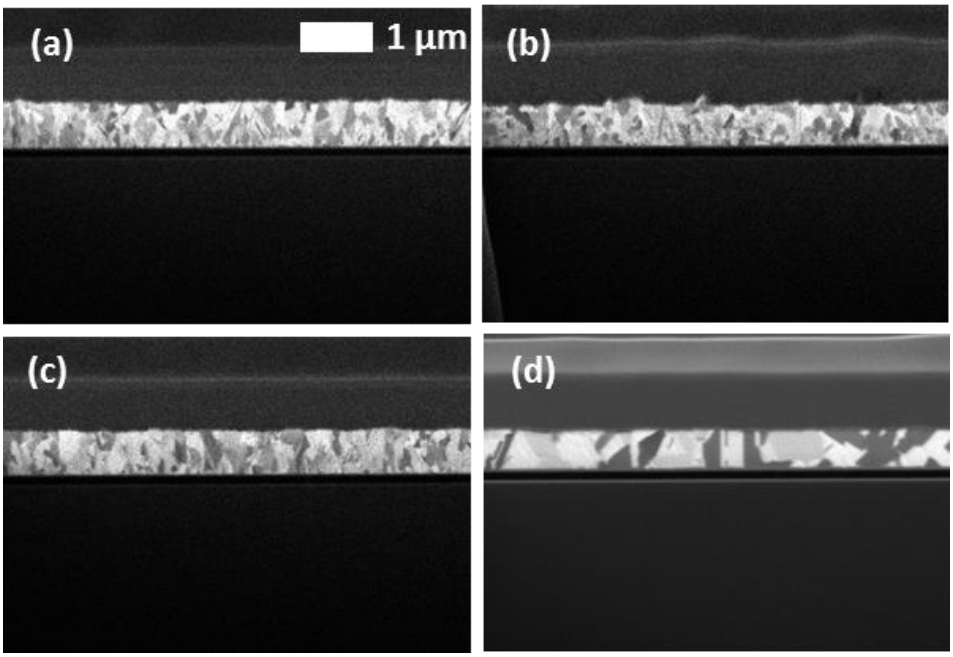

Figure 2. FIB images of Cu films after 11 days of self-annealing: (a) F_{free}, (b) F_{PEG}, (c) F_{SPS}, and (d) $F_{PEG\text{-}SPS}$.

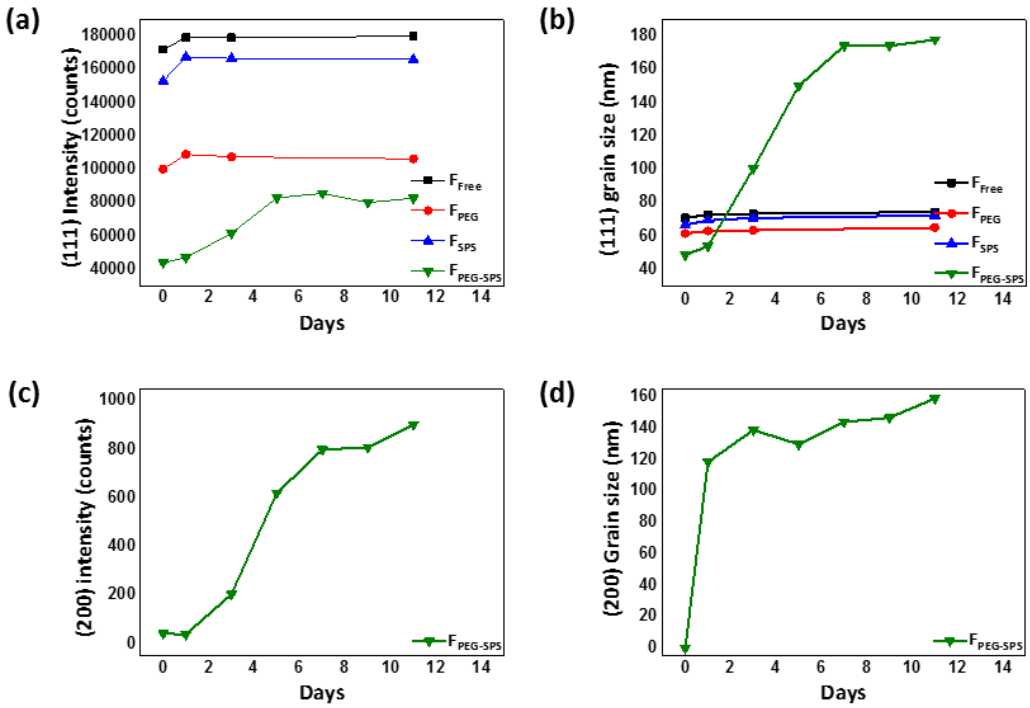

Figure 3. XRD results of Cu films with PEG 3400 and/or SPS according to the self-annealing time; (a) Cu(111) intensity, (b) calculated Cu(111)-grain size, (c) Cu(200) intensity, and (d) calculated Cu(200)-grain size.

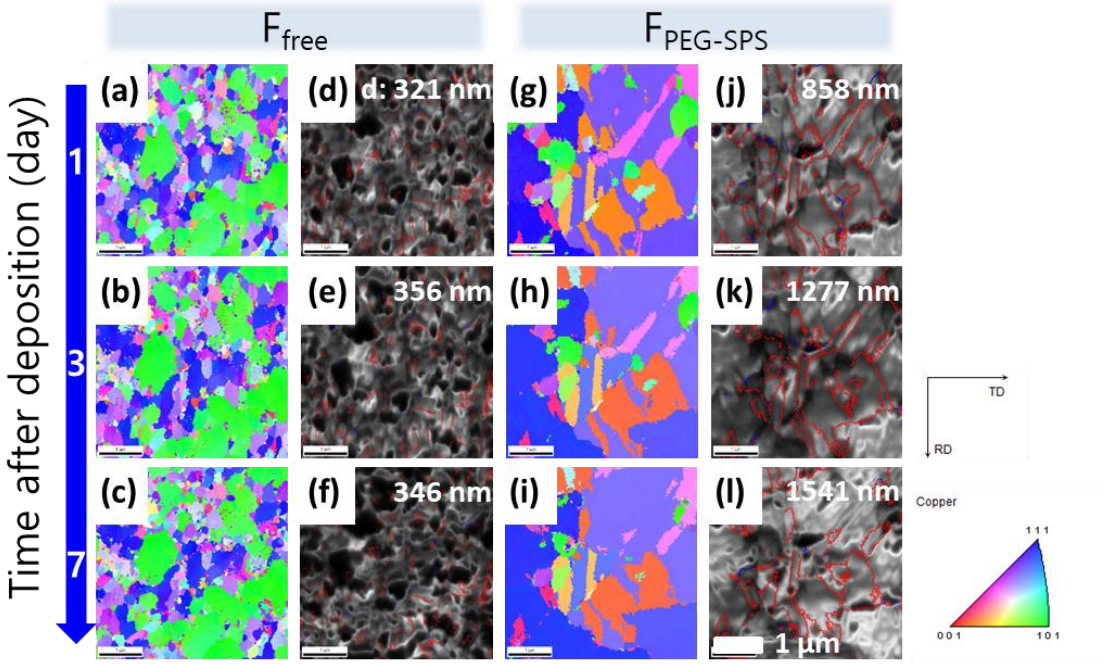

Figure 4. Inverse pole figures, (a)–(c) and (g)–(i), and gray-scale maps, (d)–(f) and (j)–(l), of the F_{free} and $F_{PEG\text{-}SPS}$ that were acquired using an EBSD analysis according to the self-annealing time. The F_{free} is (a)–(f), and the $F_{PEG\text{-}SPS}$ is (g)–(l)). Here, 'd' is the EBSD-calculated average grain size.

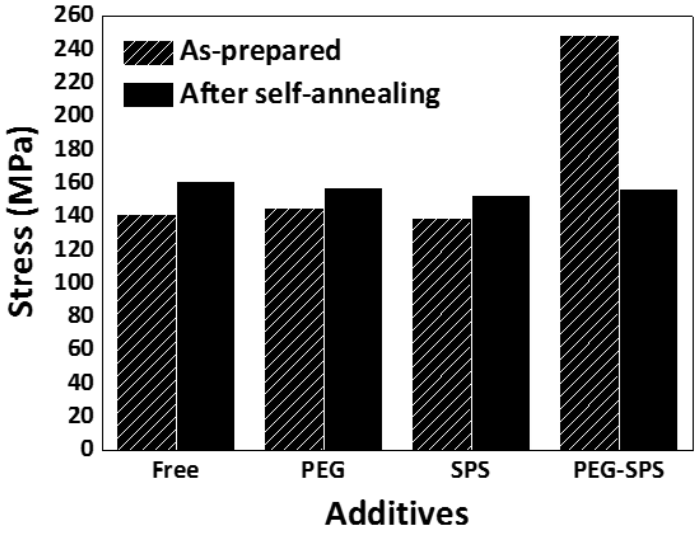

Figure 5. Residual stress of films electrodeposited with PEG 3400 and/or SPS.

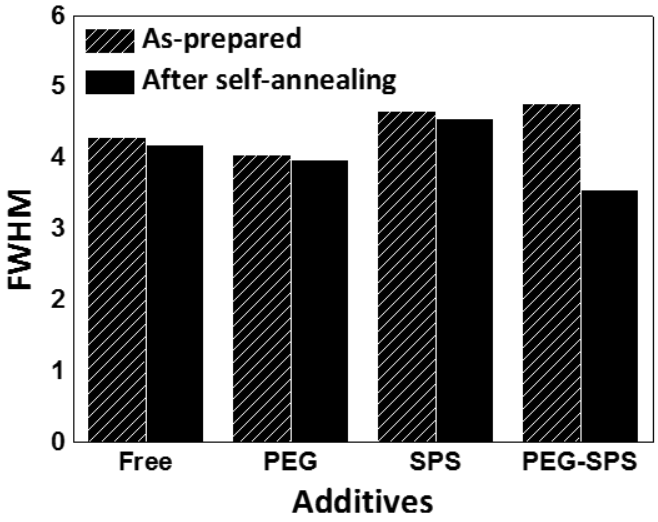

Figure 6. Rocking curve results of films electrodeposited with PEG 3400 and/or SPS.

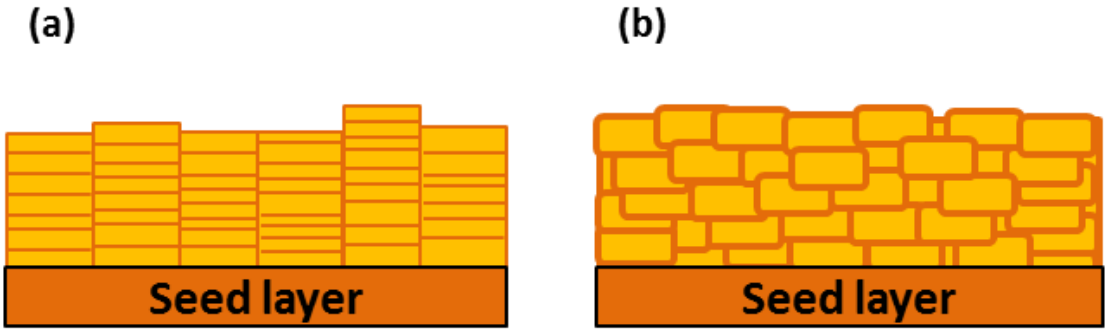

Figure 7. Illustration of a grain boundary (orange line) formation, in which the defect energy is accumulated; (a) FT type and (b) UD type.

4. Conclusion

A drastic change in the grain size of Cu films was observed during self-annealing when the film was electrodeposited with a combination of the PEG and the SPS. The grain size increased by more than 400% with the addition of the PEG-SPS, which is contrary to the 10% increase from the sole addition of either the PEG or the SPS. The significant increase in the grain size of the $F_{PEG\text{-}SPS}$ is attributed to the film stress. The film stress of the as-prepared $F_{PEG\text{-}SPS}$ is approximately 75% higher than those of the F_{PEG} and the F_{SPS}. The rocking-curve analysis revealed that the stress originated from the crystal imperfection of the $F_{PEG\text{-}SPS}$ that was developed by the displacement reaction between PEG and SPS. It is believed that this study can provide a clue for understanding the correlation between the adsorption behaviors of the organic additives and the grain growth, and for improving the reliability of the interconnects through the control of the grain size.

5. References

1. J. Tao, N. W. Cheung, and C. Hu, *IEEE Electron Device Lett.*, **14**, 249 (1993).

2. C.-K. Hu, and J. Harper, *Mater. Chem. Phys.*, **52**, 5 (1998).

3. F. d'Heurle, *Metall. Trans.*, **2**, 683 (1971).

4. L. Arnaud, G. Tartavel, T. Berger, D. Mariolle, Y. Gobil, and I. Touet, *Microelectron. Reliab.*, **40**, 77 (2000).

5. H. C. Kim, S. Choe, J. Y. Cho, D. Lee, I. Jung, W.-S. Cho, M. J. Kim, and J. J. Kim, *J. Electrochem. Soc.*, **162**, D109 (2015).

6. T. Moffat, and D. Josell, *J. Electrochem. Soc.*, **159**, D208 (2012).

7. T. Moffat, D. Wheeler, and D. Josell, *J. Electrochem. Soc.*, **151**, C262 (2004).

8. M. Tan, C. Guymon, D. R. Wheeler, and J. N. Harb, *J. Electrochem. Soc.*, **154**, D78 (2007).

9. M. Walker, L. Richter, and T. Moffat, *J. Electrochem. Soc.*, **152**, C403 (2005).

10. M. L. Walker, L. J. Richter, and T. P. Moffat, *J. Electrochem. Soc.*, **153**, C557 (2006).

11. M. J. Kim, and J. J. Kim, *Korean Chem. Eng. Res.*, **52**, 26 (2014).

12. H. C. Kim, and J. J. Kim, *Korean Chem. Eng. Res.*, **54**, 723 (2016).

13. S. Jin, G. Wang, and B. Yoo, *J. Electrochem. Soc.*, **160**, D3300 (2013).

14. K. Kondo, Y. Suzuki, T. Saito, N. Okamoto, and M. Takauchi, *Electrochem. Solid-State Lett.*, **13**, D26 (2010).

15. K. Vanstreels, S. Brongersma, Z. Tokei, L. Carbonell, W. De Ceuninck, J. D'Haen, and M. D'Olieslaeger, *J. Mater. Res.*, **23**, 642 (2008).

16. W. Zhang, S. Brongersma, N. Heylen, G. Beyer, W. Vandervorst, and K. Maex, *J. Electrochem. Soc.*, **152**, C832 (2005).

17. W. Wu, D. Ernur, S. Brongersma, M. Van Hove, and K. Maex, *Microelectron. Eng.*, **76**, 190 (2004).

18. C. Okoro, K. Vanstreels, R. Labie, O. Lühn, B. Vandevelde, B. Verlinden, and D. Vandepitte, *J. Micromech. Microeng.*, **20**, 045032 (2010).

19. H. Kadota, R. Kanno, M. Ito, and J. Onuki, *Electrochem. Solid-State Lett.*, **14**, D48 (2011).

20. S. Brongersma, E. Richard, I. Vervoort, H. Bender, W. Vandervorst, S. Lagrange,

G. Beyer, and K. Maex, *J. Appl. Phys.*, **86**, 3642 (1999).

21. S.-C. Chang, J.-M. Shieh, B.-T. Dai, M.-S. Feng, and Y.-H. Li, *J. Electrochem. Soc.*, **149**, G535 (2002).

22. M. Stangl, M. Liptak, A. Fletcher, J. Acker, J. Thomas, H. Wendrock, S. Oswald, and K. Wetzig, *Microelectron. Eng.*, **85**, 534 (2008).

23. H. Fischer, *Electrodepos. Surface treat.*, **1**, 319 (1973).

24. R. Sekar, K. K. Jagadesh, and G. N. K. R. Bapu, *Korean J. Chem. Eng.*, **6**, 1194 (2015).

25. M. Hasegawa, Y. Nonaka, Y. Negishi, Y. Okinaka, and T. Osaka, *J. Electrochem. Soc.*, **153**, C117 (2006).

26. T. Osaka, N. Yamachika, M. Yoshino, M. Hasegawa, Y. Negishi, and Y. Okinaka, *Electrochem. Solid-State Lett.*, **12**, D15 (2009).

27. Y. Zhang, G. Ding, P. Cheng, and H. Wang, *ECS Electrochem. Lett.*, **3**, D23 (2014).

28. C. V. Thompson, and R. Carel, *J. Mech. Phys. Solids*, **44**, 657 (1996).

29. W. D. Nix, *Metall. Trans. A*, **20**, 2217 (1989).

30. C. Thompson, *Annu. Rev. Mater. Sci.*, **30**, 159 (2000).

31. C. Thompson, *Scr. Metall. Mater*, **28**, 167 (1993).

32. J. J. Kim, S.-K. Kim, and Y. S. Kim, *J. Electroanal. Chem.*, **542**, 61 (2003).

33. M. Stangl, J. Acker, S. Oswald, M. Uhlemann, T. Gemming, S. Baunack, and K. Wetzig, *Microelectron. Eng.*, **84**, 54 (2007).

34. A. Patterson, *Phys. Rev.*, **56**, 978 (1939).

35. J. I. Langford, and A. Wilson, *J. Appl. Crystallogr.*, **11**, 102 (1978).

36. V. Mote, Y. Purushotham, and B. Dole, *J. Theoret. Appl. Phys.*, **6**, 6 (2012).

37. Y. Zhong, D. Ping, X. Song, and F. Yin, *J. Alloys Compd.*, **476**, 113 (2009).

38. F. Witt, and R. Vook, *J. Appl. Phys.*, **39**, 2773 (1968).

39. E. Zielinski, R. Vinci, and J. Bravman, *J. Appl. Phys.*, **76**, 4516 (1994).

40. G. Hasson, J.-Y. Boos, I. Herbeuval, M. Biscondi, and C. Goux, *Surf. Sci.*, **31**, 115 (1972).

41. P. Chaudhari, *J. Vac. Sci. Technol.*, **9**, 520 (1972).

42. M. F. Doerner, and W. D. Nix, *Crit. Rev. Solid State Mater. Sci.*, **14**, 225 (1988).

43. I. Shimizu, *Geophys. Res. Lett.*, **25**, 4237 (1998).

44. H. Fischer, *Electrodepos. Surface treat.*, **1**, 239 (1973).

45. R. Winand, *J. Appl. Electrochem.*, **21**, 377 (1991).

46. R. Winand, *Hydrometallurgy*, **29**, 567 (1992).

47. J. J. Kelly, C. Tian, and A. C. West, *J. Electrochem. Soc.*, **146**, 2540 (1999).

Appendix II

Sulfur-containing additives for mitigating Cu protrusion in through silicon via (TSV)

1. Introduction

The TSV filling is usually metallized by Cu electrodeposition with various additives, such as an accelerator, suppressor, and leveler. These additives play an important role in achieving a defect-free TSV filling by controlling the deposition profile in the TSV. Among them, the leveler, which controls the difference in deposition rate between the top and bottom of the TSV, is most important for TSV filling.[1-10] A leveler interacts with suppressors, showing convection-dependent suppression of Cu deposition, which enables selective deposition at the bottom. A variety of levelers have been investigated, but most of them are organic materials with complex structures.[2, 5, 8-10] Recently, inorganic additives such as iodide ions have been reported as a leveler.[6, 7, 11] An inorganic leveler is easy to synthesize and has advantages in monitoring the additive

degradation.

In addition to additive studies, Cu protrusion, which greatly influences the reliability of TSVs, is becoming an issue.[11-21] Cu protrusion means that Cu inside the TSV protrudes because of a difference in the thermal-expansion coefficient between Si and Cu at a high temperature during a subsequent process after the TSV filling. This Cu protrusion causes a structural deformation, deteriorating the reliability and performance of the semiconductor device. Therefore, various studies have been made to mitigate the Cu protrusion.

Most of the studies have focused mainly on how TSV factors, such as the aspect ratio and volume of TSV and the degree of expansion according to microstructure, are related to Cu protrusion. [12-18] Some studies have introduced an additional pre-annealing process that can relieve the stress between Cu and Si in order to mitigate the Cu protrusion in the following process.[19, 20] Cu protrusion can also be restrained by controlling the properties of Cu during the TSV filling process, where electrodeposition techniques and additives play an important role.[11, 22-25] This method

has a great advantage in process intensification, because no additional process is required. Recently, we reported the mitigation of Cu protrusion by adopting a two-step TSV filling with iodide ions as a leveler.[11] It has been also reported that increasing the additive concentration can reduce the degree of Cu protrusion.[21] However, there are still few reports on how to actively mitigate Cu protrusion.

In this study, we tried to control the properties of Cu during iodide-ion-derived TSV filling to mitigate Cu protrusion. We deliberately incorporated impurities into the Cu matrix to reduce the degree of Cu protrusion in TSVs. During electrodeposition, additives can be incorporated into the Cu matrix, but most of the additives do not have a significant effect on the Cu protrusion because they diffuse out over time[26] or are incorporated in small amounts.[27] However, the sulfur-containing additives with N atoms are strongly adsorbed on the Cu surface, and is known to accumulate at high levels in the Cu matrix.[27, 28] These Impurities accumulated in the Cu grain boundaries, causing a so-called pinning effect[21, 27, 29, 30] that inhibits the grain growth of Cu. To incorporate impurities into Cu-TSV, 2-mercapto-5-benzimidazole sulfonic acid

(2M5S) and thiourea (TU) were additionally used during the TSV filling with iodide ions, which are an inorganic leveler. The molecular structures of the two additives are shown in Fig. 1. These two additives have the same functional group (thiol group); however, because of structural differences, they interact differently with iodide ions. We investigated the effects of these two additives on the TSV filling with iodide ions and on the mitigation of Cu protrusion.

2. Experimental

The electrochemical behaviors of 2M5S and TU were investigated using linear sweep voltammetry (LSV) using an electrochemical workstation (PAR 263A potentiostat, Princeton Applied Research). The electrochemical measurement was performed in a three-electrode system. A Cu rotating-disk electrode (RDE, 0.196 cm^2), and an electronic-grade Cu rod were used as the working and counter electrodes, respectively. The reference electrode was an Ag/AgCl electrode (KCl saturated), which is commonly used for Cu electrodeposition.[2, 5-8, 11] The standard electrolyte consisted of 1.0 M $CuSO_4$,

0.5 M H_2SO_4, 1.4 mM HCl, and additives, which were 50 μM polyethylene glycol-polypropylene glycol copolymer (PEG-PPG; molecular weight, 1100), 10 μM bis(3-sulfopropyl) disulfide (SPS), and 400 μM NH_4I as a suppressor, accelerator, and leveler, respectively. HCl and NH_4I were used as the sources of chloride and iodide ions, respectively. Various concentrations of 2M5S and TU were then added to the standard electrolyte. The electrochemical potential was linearly scanned from 150 mV to -350 mV (vs. Ag/AgCl) at a scan rate of 10 mV/s. During the measurement, the rotational speed of the working electrode was set to 0 rpm and 1000 rpm to simulate convection conditions at the bottom and top of the TSV, respectively.

The TSV filling was done on a Si coupon wafer with patterned vias (diameter, 5 μm; depth, 60 μm; aspect ratio, 12:1). Ta (200 nm) and Cu (600 nm) films were sequentially deposited on the wafer by physical vapor deposition as a diffusion barrier and a seed layer, respectively. The filling was carried out by applying a current of 1 mA/cm_{geo}^2 for 1000 s (total deposition charge, 1000 mC/cm_{geo}^2). The composition of the electrolyte used in the TSV filling was the same as that used in the electrochemical analysis. The

substrate was horizontally rotated at 1000 rpm to apply convection during the filling process. The rotation was performed using a RDE rotator (616A, Princeton Applied Reasearch) with a lab-made RDE holder. All of the electrochemical experiment was performed at 30˚C using a thermostat to maintain constant electrolyte temperature regardless of external temperature. The cross-sectional images of TSV, were obtained using optical microscopy (OM; SOMETECH). In order to form Cu protrusions, the sample was mechanically polished after the filling, and then annealed at 400˚C for 30 min in an Ar atmosphere. The height of Cu protrusions was measured by atomic-force microscopy (AFM; Agilent Technologies, 5420).

3. Results and Discussion

The electrochemical behaviors of additives during Cu electrodeposition were investigated by LSV. Fig. 2 shows the LSV results of sulfur-containing additives under stationary (0 rpm) and convective (1000 rpm) conditions, respectively. At both conditions, the addition of 2M5S increased the reduction-current density, indicating that

2M5S reduced the inhibition effect of iodide ions. In the absence of 2M5S, Cu-ion reduction is strongly inhibited by the formation of non-conducting CuI on the electrode surface by the adsorption of iodide ions.[11] However, this inhibition effect was weakened by the addition of 2M5S, which is known to form a complex layer (Cu(I)-2M5S) on the Cu surface by combining with Cu ions.[27, 29, 30] The formation of Cu(I)-2M5S is accelerated by iodide ions, as shown in the following reaction steps,[30] and accompanies the dissolution of the CuI inhibition layer, increasing the reduction current.

$$(CuI)_{ads} + I^- \rightarrow CuI_2^- \quad (1)$$

$$CuI_2^- + 2M5S \rightarrow Cu(I)\text{-}2M5S + 2I^- + H^+ \quad (2)$$

where the proton (H^+) is the dissociation product of 2M5S that forms the Cu(I)-2M5S complex.

Given convection, this effect was more evident because of the facile mass transfer of 2M5S. The high surface concentration of 2M5S would result in the greater surface

coverage of Cu(I)-2M5S rather than CuI. TU behaved differently from 2M5S. Under stationary condition, TU had a negligible influence on the inhibition effect of CuI, as shown in Fig. 2(a). However, under convection (Fig. 2(b)), TU showed an additional inhibition effect in the presence of CuI. These electrochemical behaviors were related to the complex formation between TU and CuI. TU combines with CuI to form complexes of various structures, such as unconnected forms, chains, and web structures, depending on the ratio of TU to CuI on the electrode surface.[31-35] The stability of such complexes is an important factor influencing the inhibition of Cu-ion reduction. Under stationary condition where the surface concentration of TU was low, the TU-CuI complex was not stable enough to have an additional inhibition effect on the surface. However, when the convection is applied, there will be sufficient TU on the surface, and a stable TU-CuI complex will form. This further inhibited Cu-ion reduction, as shown in Fig. 2(b).

These electrochemical interactions between additives affected TSV filling significantly. Fig. 3 shows cross-sectional images of TSVs after the TSV filling with various concentration of 2M5S. In the standard electrolyte (Fig. 3(a)), a uniform and

defect-free TSV filling was achieved. However, as shown in Figs. 3(b) and (c), void-free-filled TSVs (fully filled) and conformally filled TSVs (not fully filled) coexisted at 50 and 100 μM of 2M5S. This non-uniformity of TSV filling with 2M5S can be clearly observed in the top surface image (Fig. 3(e)). As shown by the electrochemical analysis in Fig. 2, the formation of Cu(I)-2M5S complexes weakens the inhibition effect of CuI, particularly on the top surface, in which the mass transfer of 2M5S is facilitated. Therefore, the formation of Cu(I)-2M5S resulted in excessive Cu deposition on the top surface, as shown in Figs. 3(b) and (c). The conformal filling occurred for the same reason: the formation of Cu(I)-2M5S on the TSV reduced the difference in inhibition effect between the bottom and side of the TSVs. At the higher 2M5S concentration (Fig. 3(d)), the TSV filling was no longer achieved, as will be discussed later.

The filling profiles of TSV at various concentrations of TU are shown in Fig. 4. A uniform defect-free TSV filling was achieved at all TU concentrations investigated, indicating that TU formed a stable inhibition layer with CuI on the top of the TSVs, regardless of TU concentration. The uniform filling of TSVs can be also clearly observed

in Fig. 4(d) with 150 μM of TU.

TSV filling using 2M5S resulted in both defect-free filled TSVs and unfilled TSVs (Fig. 3). In contrast, TU achieved uniform and defect-free TSVs (Fig. 4); there was no TSV where the filling was incomplete. The difference in the filling results of 2M5S and TU was attributed to the different interactions of the additives with iodide ions: 2M5S competes with iodide ions to break the CuI inhibition layer, whereas TU reinforces the CuI layer (Fig. 2). We compared the filling profiles of half-filled TSVs to demonstrate the difference, as shown in Fig. 5. The half-filled TSV was obtained after 500 s of the deposition (500 mC). Figs. 5(a) and (b) are the TSV profiles after the deposition with 2M5S. The TSVs were filled from the bottom. However, the filling ratio of each TSV was different, and Cu deposition was observed on the side of TSV (conformal filling). These factors indicate that the formation of Cu(I)-2M5S complexes on the surface was not uniform and thus weakened the inhibition effect of CuI. CuI shows a leveling effect by inhibiting Cu deposition, particularly at the top of TSV, resulting in the flat growing surface of Cu inside the TSV, as shown in Fig. 5(e). However, Cu(I)-2M5S complexes

compete with CuI, and this interaction caused the non-uniform and conformal filling (Figs. 3(b)–(d)). This phenomenon was more apparent at high concentrations of 2M5S (Fig. 5(b)). The weakened inhibition effect and charge leakage at the top, induced by the formation of Cu(I)-2M5S, led to non-uniform and conformal TSV filling. When TU was added (Figs. 5(c) and (d)), the growing surface of Cu inside the TSV was kept flat during the deposition, as is similar to the TSV filling without any 2M5S and TU (Fig. 5(e)), thus showing that TU formed a stable inhibition layer in a form of TU-CuI complexes.

The coupon wafers after the TSV filling with 2M5S were mechanically polished and annealed at 400℃ for 30 min to observe the effect of 2M5S on Cu protrusion. Fig. 6 shows AFM line scan profiles and topographs of the Cu protrusions formed on the Cu-filled TSVs after the annealing. When the 2M5S was added for TSV filling, the height of the Cu protrusion was decreased significantly. The degree of Cu protrusion was mitigated as the concentration of 2M5S increased. The average heights of Cu protrusions were 438.5, 197.0, and 85.5 nm for 50, 75, and 100 μM of 2M5S, respectively. These values were 75.7%, 34.8%, and 15.1% of the height of Cu protrusion without 2M5S, the

reference value (565.8 nm). It is well known that, during Cu electrodeposition, 2M5S adsorbs strongly on the Cu surface and is incorporated into the Cu. [27, 29] This process is accelerated by the catalytic effect of iodide ions.[30] The incorporated 2M5S induced a pinning effect, effectively mitigating Cu protrusion.

The effect of TU on the mitigation of Cu protrusion was also observed (Fig. 7). The heights of the Cu protrusions were 557.8, 340.4, 309.5 nm, and 174.2 nm at 50, 75, 100, and 150 μM of TU, respectively. These values are 98.5%, 60.2%, 54.7%, and 30.8% of the reference value, respectively. This result indicates that TU suppresses Cu protrusion less than 2M5S does at the same concentration. However, in terms of the uniformity of TSV filling, it is desirable to use TU rather than 2M5S for the mitigation of Cu protrusion. A uniform TSV filling was achieved even at a high concentration (150 μM) of TU, and the Cu protrusion was reduced by 69.2%, similar to that by 75 μM of 2M5S.

The height changes of the Cu protrusion according to the concentrations of 2M5S and TU are summarized in Fig. 8. The Cu protrusion was gradually alleviated as the concentration of both additives increased. This is because the incorporation of more

additives enhanced the pinning effect. Both additives have a mercapto group with two N atoms that can easily form a strong complex with Cu ions, resulting in a high level of incorporation in the Cu matrix. However, comparing the effects of the two additives, 2M5S showed a stronger pinning effect than did TU at the same concentration, because of the difference in molecular structure between 2M5S and TU. In addition to the mercapto group, 2M5S contains a benzene ring, which is advantageous for the incorporation into the Cu matrix. The existence of a benzene ring in the molecular structure promoted the additive incorporation and increased the pinning effect.[27]

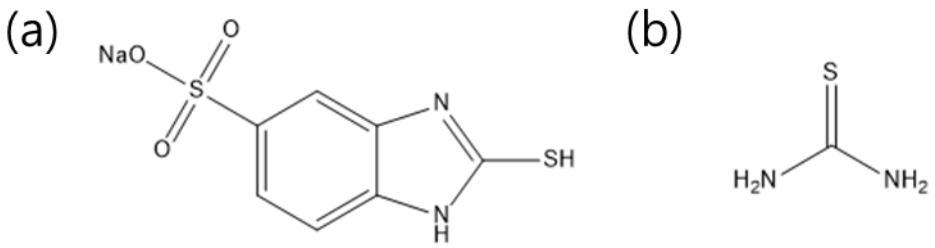

Figure 1. Molecular structures of (a) 2-mercapto-5-benzimidazole sulfonic acid (2M5S) and (b) thiourea (TU).

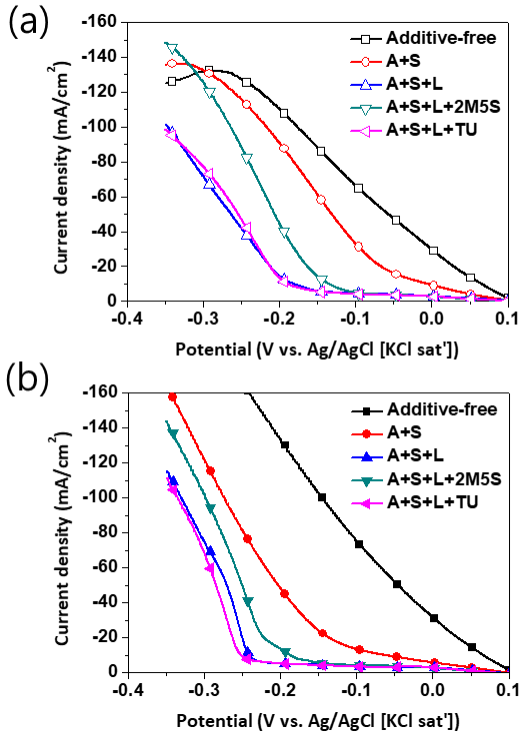

Figure 2. LSV curves of Cu electrodes in the deposition electrolytes with various combination of additives (a) at 0 rpm (b) at 1000 rpm. The additives were 10 μM SPS (A), 50 μM PEG-PPG (S), 400 μM NH_4I (L), 100 μM 2M5S, and 100 μM TU. The additive-free electrolyte was composed of 1.0 M $CuSO_4$, 0.5 M H_2SO_4, 1.4 mM HCl.

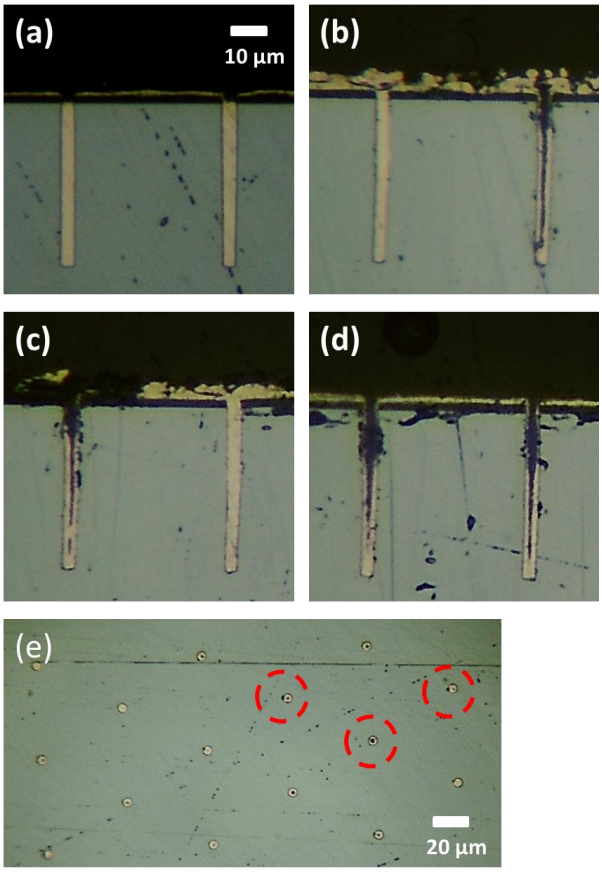

Figure 3. TSV filling profiles formed in 2M5S-containing standard electrolyte; (a) 0 μM, (b) 50 μM, (c) 100 μM, (d) 150 μM of 2M5S, and (e) top view of TSV filled with 100 μM of 2M5S. The standard electrolyte was composed of 1.0 M $CuSO_4$, 0.5 M H_2SO_4, 1.4 mM HCl, 50 μM PEG-PPG, 10 μM, SPS and 400 μM NH_4I.

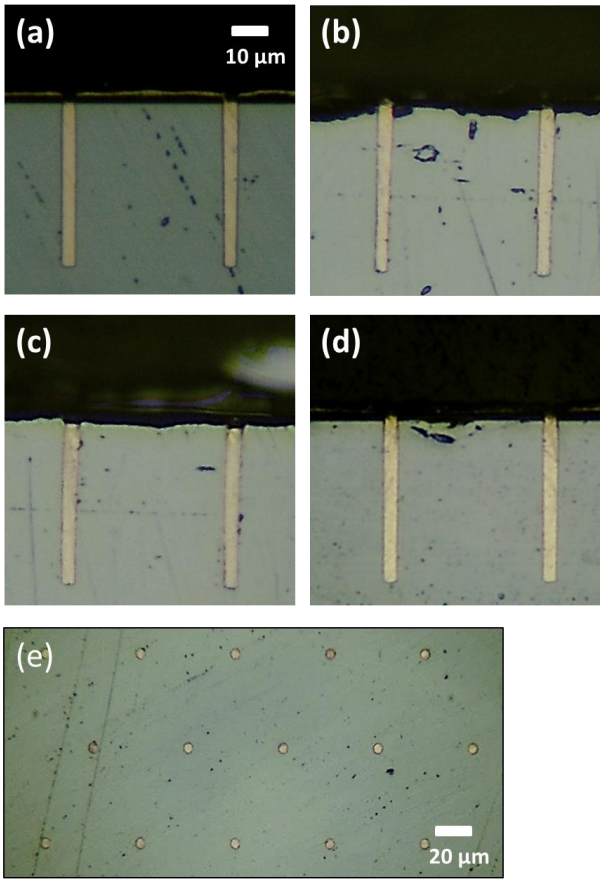

Figure 4. TSV filling profiles formed in TU-containing standard electrolyte; (a) 0 µM, (b) 50 µM, (c) 100 µM, (d) 150 µM of TU, and (e) top view of TSV filled with 100 µM of TU. The standard electrolyte was composed of 1.0 M $CuSO_4$, 0.5 M H_2SO_4, 1.4 mM HCl, 50 µM PEG-PPG, 10 µM, SPS and 400 µM NH_4I.

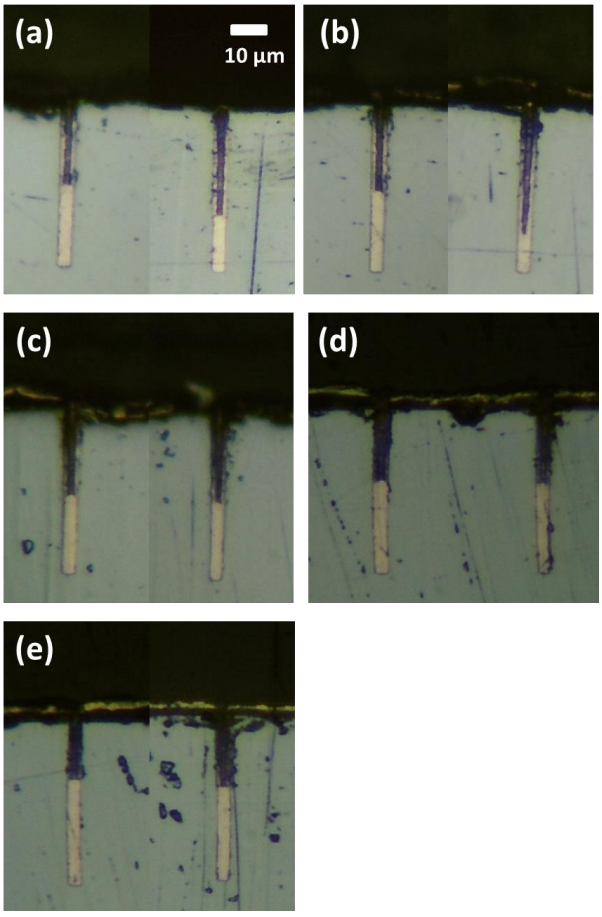

Figure 5. Half-filled TSV profiles formed in additive-containing standard electrolyte; (a) 50 μM 2M5S, (b) 100 μM 2M5S, (c) 50 μM TU, (d) 100 μM TU, and (e) the standard electrolyte. The standard electrolyte was composed of 1.0 M $CuSO_4$, 0.5 M H_2SO_4, 1.4 mM HCl, 50 μM PEG-PPG, 10 μM, SPS and 400 μM NH_4I.

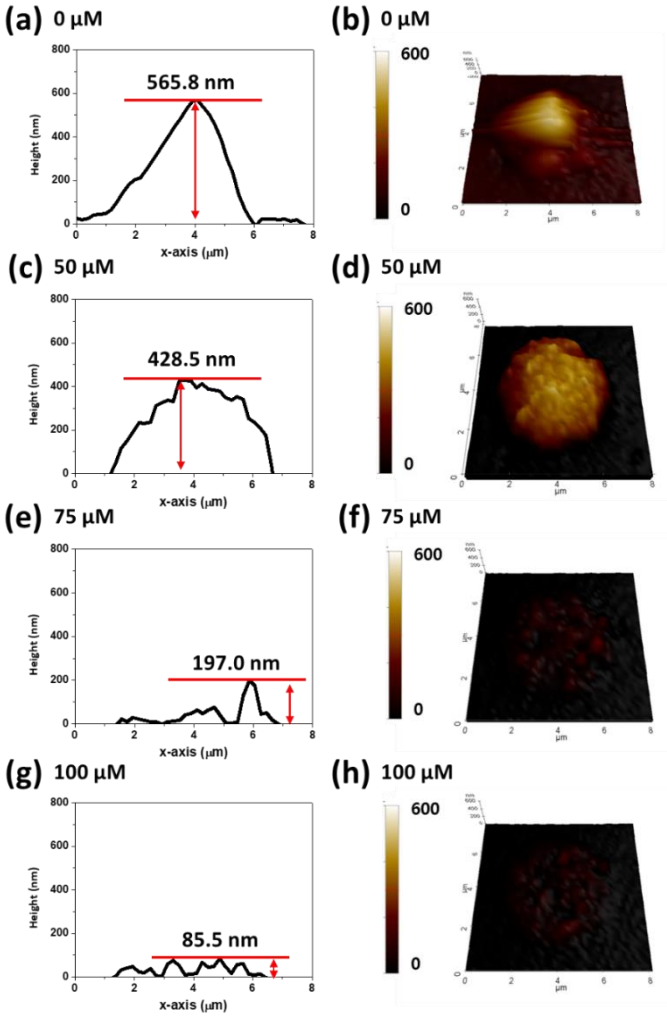

Figure 6. The scan profiles, (a), (c), (e), and (g), and AFM topography images, (b), (d), (f), and (h), of Cu protrusions formed on the TSVs filled at various concentrations of 2M5S. The TSVs were annealed at 400˚C for 30 min in an Ar atmosphere..

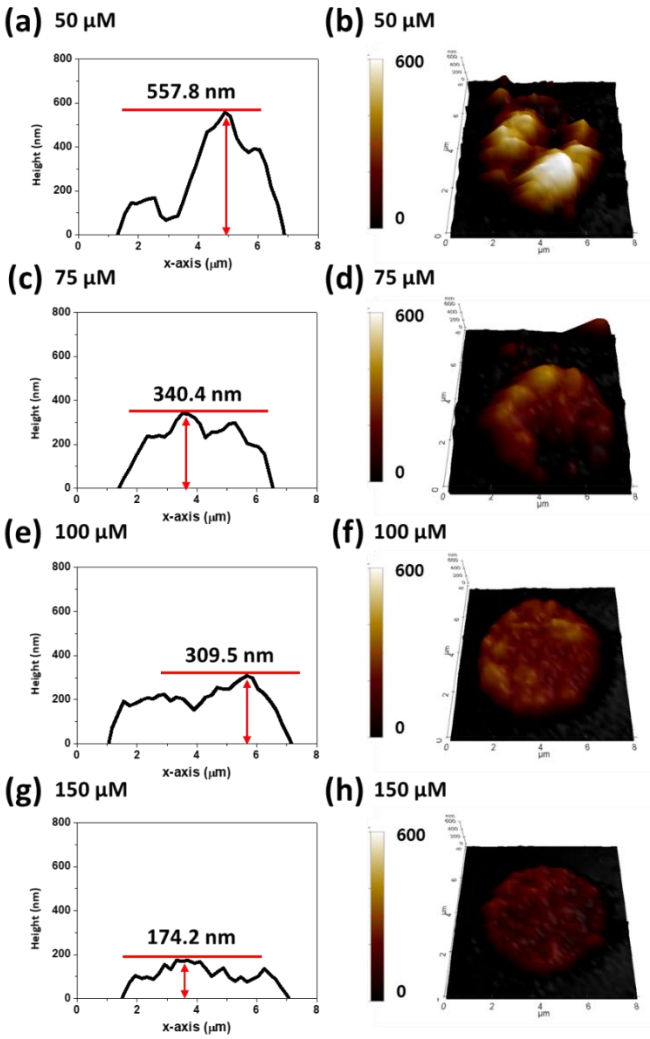

Figure 7. The scan profiles, (a), (c), (e), and (g), and AFM topography images, (b), (d), (f), and (h), of Cu protrusions formed on the TSVs filled at various concentrations of TU. The TSVs were annealed at 400˚C for 30 min in an Ar atmosphere.

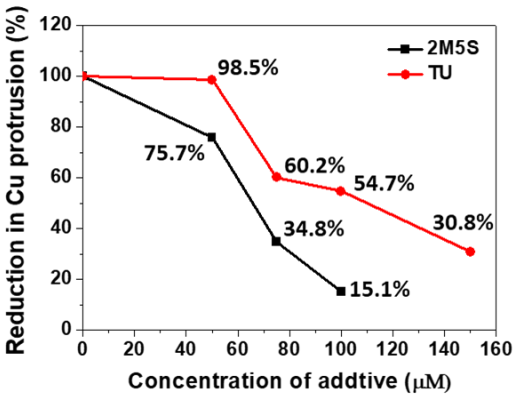

Figure 8. Reduction in Cu protrusion (%) using 2M5S or TU.

4. Conclusions

Cu protrusion of a TSV was mitigated by using a separate additive during Cu electrodeposition. The additives, 2M5S and TU, were incorporated into the Cu matrix during deposition, reducing the degree of Cu protrusion by a pinning effect. 2M5S, which contains a benzene ring, showed a stronger pinning than TU did because of its strong binding force with Cu ions. At 100 μM of 2M5S, Cu protrusion was reduced by 84.9%. However, the uniformity of TSV filling was poor because of the formation of Cu(I)-2M5S, which weakened the leveling effect of the iodide ions. On the other hand, TU, not containing a benzene ring, mitigated Cu protrusion by 69.2% (at 150 μM). Though the mitigation of Cu protrusion by TU was weaker than that by 2M5S, uniform TSV filling was achieved at even higher TU concentration, because TU forms a stable TU-CuI inhibition layer on the Cu surface.

5. References

1. F. Inoue, H. Philipsen, A. Radisic, S. Armini, Y. Civale, P. Leunissen, M. Kondo, E. Webb and S. Shingubara, *Electrochim. Acta*, **100**, 203 (2013).

2. S. Jin, G. Wang and B. Yoo, *J. Electrochem. Soc.*, **160**, D3300 (2013).

3. D. Josell, D. Wheeler and T. Moffat, *J. Electrochem. Soc.*, **159**, D570 (2012).

4. H. Kadota, R. Kanno, M. Ito and J. Onuki, *Electrochem. Solid-State Lett.*, **14**, D48 (2011).

5. H. C. Kim, S. Choe, J. Y. Cho, D. Lee, I. Jung, W.-S. Cho, M. J. Kim and J. J. Kim, *J. Electrochem. Soc.*, **162**, D109 (2015).

6. H. C. Kim, M. J. Kim and J. J. Kim, *J. Electrochem. Soc.*, **165**, D91 (2018).

7. M. J. Kim, H. C. Kim and J. J. Kim, *J. Electrochem. Soc.*, **163**, D434 (2016).

8. M. J. Kim, Y. Seo, H. C. Kim, Y. Lee, S. Choe, Y. G. Kim, S. K. Cho and J. J. Kim, *Electrochim. Acta*, **163**, 174 (2015).

9. L. Menk, D. Josell, T. Moffat, E. Baca, M. Blain, A. Smith, J. Dominguez, J. McClain, P. Yeh and A. Hollowell, *J. Electrochem. Soc.*, **166**, D3066 (2019).

10. T. Moffat and D. Josell, *J. Electrochem. Soc.*, **159**, D208 (2012).

11. M. Sung, S.-H. Kim, H.-J. Lee, T. Lim and J. J. Kim, *Electrochim. Acta*, **295**, 224 (2019).

12. F. Che, W. Putra, A. Heryanto, A. Trigg, X. Zhang and C. Gan, *IEEE T. Comp. Pack. Man.*, **3**, 732 (2013).

13. J. De Messemaeker, O. V. Pedreira, H. Philipsen, E. Beyne, I. De Wolf, T. Van der Donck and K. Croes, in *Electronic Components and Technology Conference*, p. 613, IEEE (2014).

14. J. De Messemaeker, O. V. Pedreira, B. Vandevelde, H. Philipsen, I. De Wolf, E. Beyne and K. Croes, in *Electronic Components and Technology Conference*, p. 586, IEEE (2013).

15. A. Heryanto, W. Putra, A. Trigg, S. Gao, W. Kwon, F. Che, X. Ang, J. Wei, R. I. Made and C. L. Gan, *J. Electron. Mater.*, **41**, 2533 (2012).

16. P. Kumar, I. Dutta and M. Bakir, *J. Electron. Mater.*, **41**, 322 (2012).

17. M. Pathak, J. Pak, D. Z. Pan and S. K. Lim, in *Proceedings of the International*

Conference on Computer-Aided Design, p. 555, IEEE (2011).

18. D. Zhang, K. Hummler, L. Smith and J. J.-Q. Lu, in *Electronic Components and Technology Conference*, p. 1407, IEEE (2013).

19. X. Jing, H. He, L. Ji, C. Xu, K. Xue, M. Su, C. Song, D. Yu, L. Cao and W. Zhang, in *Electronic Components and Technology Conference*, p. 1116, IEEE (2014).

20. X. Jing, U.-H. Lee, C. Xu, Z. Niu, H. Hao, J.-Y. Bae, J. Won and W. Zhang, in *International Symposium on the Physical and Failure Analysis of Integrated Circuits*, p. 45, IEEE (2015).

21. S. Chen, F. Qin, R. Wang, T. An and H. Yu, in *International Conference on Electronic Packaging Technology* p. 875, IEEE (2015).

22. J. J. Kelly, C. Tian and A. C. West, *J. Electrochem. Soc.*, **146**, 2540 (1999).

23. C. Okoro, K. Vanstreels, R. Labie, O. Lühn, B. Vandevelde, B. Verlinden and D. Vandepitte, *J. Micromech. Microeng.*, **20**, 045032 (2010).

24. M. Sung, H. C. Kim, T. Lim and J. J. Kim, *J. Electrochem. Soc.*, **164**, D805 (2017).

25. W. Wu, D. Ernur, S. Brongersma, M. Van Hove and K. Maex, *Microelectron. Eng.*,

76, 190 (2004).

26. M. Stangl, J. Acker, S. Oswald, M. Uhlemann, T. Gemming, S. Baunack and K. Wetzig, *Microelectron. Eng.*, **84**, 54 (2007).

27. M. Matsuda, T. Takahashi, S. Yoshihara and M. Dobashi, *Trans. Jpn. Inst. Electron. Packag.*, **2**, 55 (2009).

28. A. Lee, M. J. Kim, S. Choe and J. J. Kim, *Korean J. Chem. Eng.*, **36**, 981 (2019).

29. S. Yoshihara, *ECS Trans.*, **41**, 1 (2012).

30. D. Zhang, L. Gao and G. Zhou, *J. Appl. Electrochem.*, **33**, 361 (2003).

31. G. A. Bowmaker, J. V. Hanna, C. Pakawatchai, B. W. Skelton, Y. Thanyasirikul and A. H. White, *Inorg. Chem.*, **48**, 350 (2008).

32. H. C. Kim, M. J. Kim, S. Choe, T. Lim, K. J. Park, K. H. Kim, S. H. Ahn, S.-K. Kim and J. J. Kim, *J. Electrochem. Soc.*, **161**, D749 (2014).

33. S. Ramaprabhu, E. A. Lucken and G. Bernardinelli, *J. Chem. Soc., Dalton Trans.*, 115 (1995).

34. A. Saxena, E. C. Dugan, J. Liaw, M. D. Dembo and R. D. Pike, *Polyhedron*, **28**,

4017 (2009).

35. R. Vranka and E. Amma, *J. Am. Chem. Soc.*, **88**, 4270 (1966).

Appendix III

Synthetic Route of Synthesized Organic Leveler Containing Quaternary Ammonium and Naphthalene ring

*All of synthetic route was performed by Yoonjae Lee in Laboratory of professor Young Gyu Kim.

1. Synthesis of Lev 1

2-(Bromomethyl)naphthalene (1,596 mg, 7.22 mmol) was added to a solution of 1,2″-bis(*N,N*-dimethylaminomethyl) triethylene glycol (**3**) (867 mg, 3.28 mmol) in THF (10 mL) and methanol (10 mL), and the resulting mixture was stirred for 12 hrs at room temperature. Then, the reaction mixture was concentrated under the reduced pressure. The obtained crude reaction mixture was diluted with distilled water (20 mL), washed with ethyl acetate (EtOAc, 20 mL), and the combined aqueous layer was concentrated under the reduced

pressure to give **Lev 1** as viscous yellowish oil (14,803 mg, 82% yield from compound **2**); ^{1}H NMR (MeOH-d_4) δ 3.18 (6H, s), 3.24 (6H, s), 3.51-3.62 (8H, m), 3.72 (4H, s), 4.48 (2H, br s), 4.84 (4H, ABq, *J*=13.2), 7.60-7.64 (4H, m), 7.67-7.70 (2H, m), 7.95-8.03 (6H, m), 8.19 (2H, s); ^{13}C NMR (MeOH-d_4) δ 51.6, 51.9, 66.2, 67.9, 70.3, 71.9, 74.4, 126.3, 128.1, 128.8, 128.9, 129.5, 129.9, 130.4, 134.3, 135.1, 135.3; HRMS for **Lev 1** (FAB) calcd for $C_{34}H_{46}BrN_2O_4^+$ 625.2641 ($[M-Br]^+$), found 625.2635.

2. Synthesis of PEG 600-diallyl ether (4)

Sodium hydride (55% NaH, 458 mg, 10.5 mmol) was slowly added to a solution of polyethylene glycol 600 (PEG 600, 2,100 mg, 3.5 mmol) dissolved in THF (20 mL) and *N*,*N*-dimethylformamide (DMF, 5 mL) at 0 ºC and stirred for 30 min under nitrogen atmosphere. Then, tetrabutylammonium iodide ($Bu_4N^+I^-$, 277 mg, 0.7 mmol) and allyl bromide (0.91 mL, 10.5 mmol) were added to a

reaction mixture and stirred at room temperature for 8 hrs. The reaction mixture was quenched with addition of distilled water (1 mL), and the resulting mixture was partitioned between ethyl acetate (EtOAc, 20 mL) and distilled water (10 mL). The separated organic layer was washed with distilled water (5 mL × 2), and the combined organic layers were dried over $MgSO_4$, filtered, and concentrated under the reduced pressure. The crude mixture was purified by silica gel column chromatography with the gradient eluents (1:1 hexane:EtOAc to 1:1:5 hexane:MeOH:EtOAc to 10:1 CH_2Cl_2:MeOH) to afford compound **4** (2,157 mg, 91%) as colorless oil; ^{1}H NMR ($CDCl_3$) δ 3.59-3.68 (50H, m), 4.03 (4H, m), 5.17-5.30 (4H, m), 5.87-5.97 (2H, m); ^{13}C NMR ($CDCl_3$) δ 69.4, 70.5, 70.6, 72.2, 117.0, 134.8; The compound **4** was also characterized by MALDI-ToF MS (Fig. 1).

3. Synthesis of PEG 600-diglycidyl ether (5)

A solution of compound **4** (2,360 mg, 3.47 mmol) and *meta*-chloroperoxybenzoic acid (75% *m*CPBA, 2,393 mg, 10.4 mmol) dissolved in dichloromethane (CH_2Cl_2, 20 mL) was refluxed for 6 hrs. Then, the reaction mixture was diluted with CH_2Cl_2 (10 mL) and washed with sat. $NaHCO_3$ (20 mL x 3). The organic layer was dried over $MgSO_4$, filtered, and concentrated under the reduced pressure. The crude mixture was purified by silica gel column chromatography with the gradient eluents (1:1:5 hexane:MeOH:EtOAc to 10:1 CH_2Cl_2:MeOH) to afford compound **5** (889 mg, 36%) as colorless oil; ^{1}H NMR ($CDCl_3$) δ 2.60-2.62 (2H, dd, *J*=4.8, 2.8), 2.78-2.81 (2H, dd, *J*=4.8, 4), 3.15-3.18 (2H, m), 3.41-3.46 (2H, m), 3.65-3.71 (54H, m), 3.77-3.81 (2H, m); ^{13}C NMR ($CDCl_3$) δ 43.9, 50.5, 70.3, 70.5, 71.7; The compound **5** was also characterized by MALDI-ToF MS (Fig. 2)

4. Synthesis of ω,ω'–bis(*N*,*N*'-dimethylaminomethyl)PEG 600 (6)

N,*N*'-dimethylamine (2 M in MeOH, 10 mL, 20 mmol) was added to a solution of compound **5** dissolved in MeOH (5 mL) at room temperature and stirred for 12 hrs. Then, the reaction mixture was concentrated to remove MeOH. The concentrated crude mixture was diluted with distilled water (10 mL) and washed with EtOAc (10 mL). The aqueous layer was concentrated under the reduced pressure to afford compound **6** as viscous yellowish oil; ^{1}H NMR (MeOH-d_4) δ 2.37 (12H, s), 2.45-2.53 (4H, m), 3.43-3.48 (4H, m), 3.59-3.64 (54H, m), 3.88-3.92 (2H, m); ^{13}C NMR (MeOH-d_4) δ 46.0, 63.2, 68.7, 71.5, 71.7, 75.2; The compound **6** was also characterized by MALDI-ToF MS (Fig. 3).

5. Synthesis of Lev 600

Lev 600 was synthesized in the same synthetic procedure of **Lev 1** above. Starting from the compound **6** (988 mg, 1.23 mmol), **Lev 600** (1,414 mg, 94% yields from compound **5**) was obtained as viscous yellowish oil; ^{1}H NMR

(MeOH-d_4) δ 3.17 (6H, s), 3.24 (6H, s), 3.45-3.54 (8H, m), 3.59-3.65 (60H, m), 4.46 (2H, br s), 4.84 (4H, ABq, *J*=12), 7.61-7.69 (6H, m), 7.96-8.04 (6H, m), 8.18 (2H, s); ^{13}C NMR (MeOH-d_4) δ 51.7, 52.0, 66.2, 67.7, 70.4, 71.5, 71.8, 74.3, 126.4, 128.1, 128.8, 128.9, 129.6, 129.9, 130.5, 134.3, 135.1, 135.3; **Lev 600** was also characterized by MALDI-ToF MS (Fig. 4).

6. Synthesis of PEG 1000-diallyl ether (7)

Compound **7** was synthesized in the same synthetic procedure of compound **4** above. Starting from the PEG 1000 (5,000 mg, 5 mmol), compound **7** (2,357 mg, 2.18 mmol) was obtained as colorless solid; ^{1}H NMR ($CDCl_3$) δ 3.60-3.68 (82H, m), 4.02-4.04 (4H, m), 5.17-5.30 (4H, m), 5.89-5.97 (2H, m); ^{13}C NMR ($CDCl_3$) δ 69.3, 70.4, 70.5, 72.1, 116.9, 134.7; The compound **7** was also characterized by MALDI-ToF MS (Fig. 5).

7. Synthesis of PEG 1000-diglycidyl ether (8)

Compound **8** was synthesized in the same synthetic procedure of compound **5** above. Starting from the compound **7** (909 mg, 0.84 mmol), compound **8** (430 mg, 0.39 mmol) was obtained as white solid; ^{1}H NMR ($CDCl_3$) δ 2.60-2.62 (2H, dd, *J*=4.8, 2.8), 2.79-2.81 (2H, dd, *J*=4.8, 4), 3.16-3.17 (2H, m), 3.41-3.45 (2H, m), 3.65-3.71 (94H, m), 3.77-3.81 (2H, m); ^{13}C NMR (CDCl3) δ 44.4, 50.9, 70.7, 70.9, 72.1; The compound **8** was also characterized by MALDI-ToF MS (Fig. 6).

8. Synthesis of ω,ω'–bis(*N*,*N*'-dimethylaminomethyl)PEG 1000 (9)

Compound **9** was synthesized in the same synthetic procedure of the compound **8** above. Starting from the compound 8 (430 mg, 0.39 mmol), compound **9** was obtained as yellowish solid; ^{1}H NMR (MeOH-d_4) δ 2.37 (12H, s), 2.46-2.54 (4H, m), 3.41-3.50 (4H, m), 3.59-3.64 (104H, m), 3.88-3.92 (2H,

m); ^{13}C NMR (MeOH-d_4) δ 51.8, 52.0, 66.2, 67.8, 70.4, 71.6, 71.9, 74.3, 126.5, 128.2, 128.9, 129.0, 129.6, 130.0, 130.6, 134.4, 135.2, 135.4; The compound **9** was also characterized by MALDI-ToF MS (Fig. S7).

9. Synthesis of Lev 1000

Lev 1000 was synthesized in the same synthetic procedure of **Lev 1** above. Starting from the compound **9** (469 mg, 0.39 mmol), **Lev 1000** (580 mg, 90% yields from compound **8**) was obtained as viscous yellowish solid; ^{1}H NMR (MeOH-d$_4$) δ 3.18 (6H, s), 3.24 (6H, s), 3.49-3.54 (8H, m), 3.60-3.65 (112H, m), 4.46 (2H, br s), 4.84 (4H, ABq, *J*=12), 7.62-7.69 (6H, m), 7.96-8.05 (6H, m), 8.19 (2H, s); ^{13}C NMR (MeOH-d$_4$) δ 51.7, 52.0, 66.1, 67.7, 70.3, 71.5, 71.8, 74.2, 126.4, 128.1, 128.8, 128.9, 129.6, 129.9, 130.5, 134.3, 135.1, 135.3; **Lev 1000** was also characterized by MALDI-ToF MS (Fig. S8).

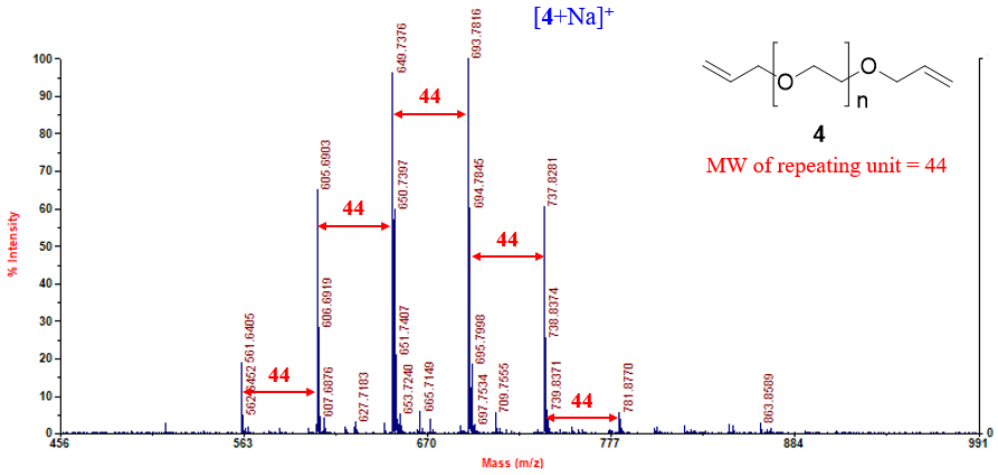

Figure 1. MALDI-ToF mass spectrum of compound **4** (calculated for $C_{32}H_{62}O_{14}Na^+$ 693.82 [**4**+Na]$^+$, found 693.78).

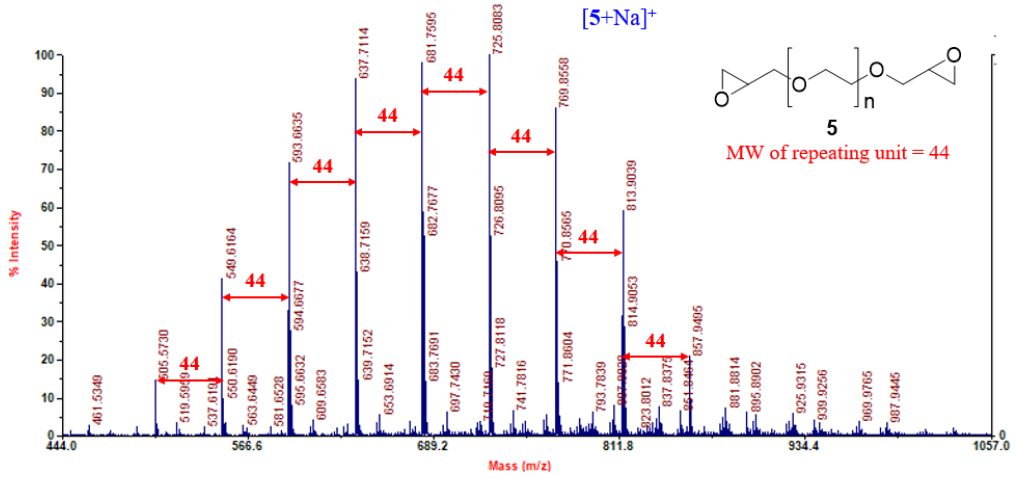

Figure 2. MALDI-ToF mass spectrum of compound **5** (calculated for $C_{32}H_{62}O_{16}Na^+$ 725.82 [**5**+Na]$^+$, found 725.81).

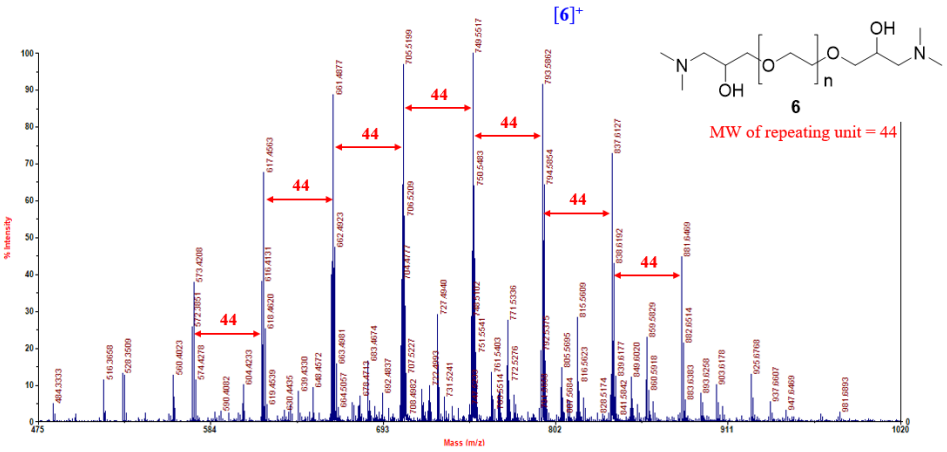

Figure 3. MALDI-ToF mass spectrum of compound **6** (calculated for $C_{36}H_{76}N_2O_{16}^+$ 793.00 [**6**]$^+$, found 793.59).

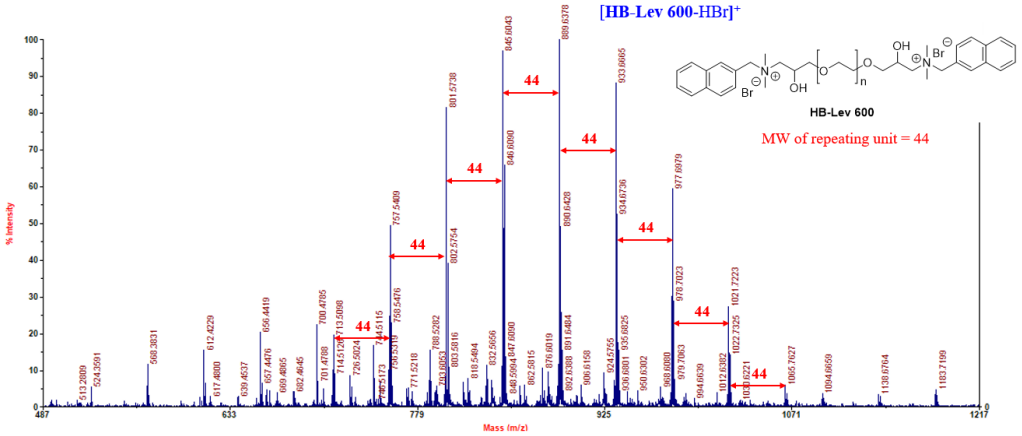

Figure 4. MALDI-ToF mass spectrum of compound **Lev 600** (calculated for $C_{46}H_{69}BrN_2O_{10}^+$ 889.97 [**Lev 600**-HBr]$^+$, found 889.64).

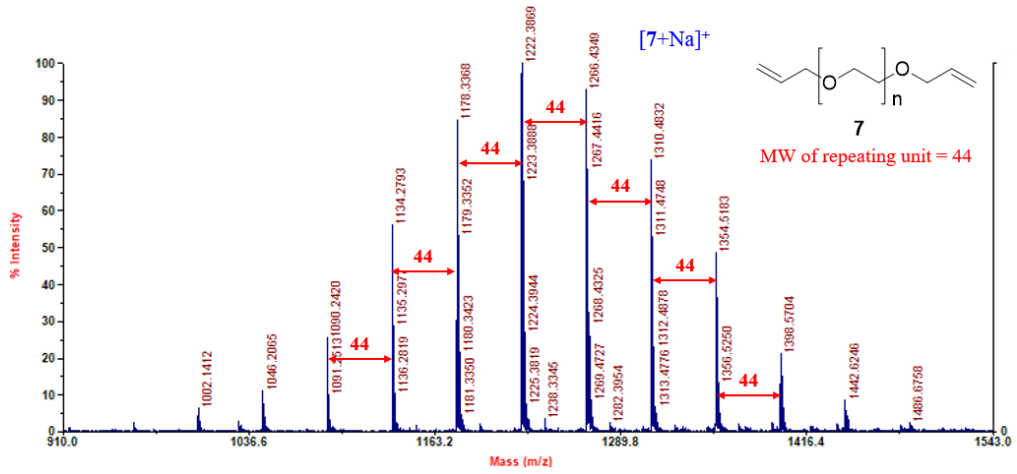

Figure 5. MALDI-ToF mass spectrum of compound **7** (calculated for $C_{52}H_{102}O_{24}Na^+$ 1134.35 [**7**+Na]$^+$, found 1134.28).

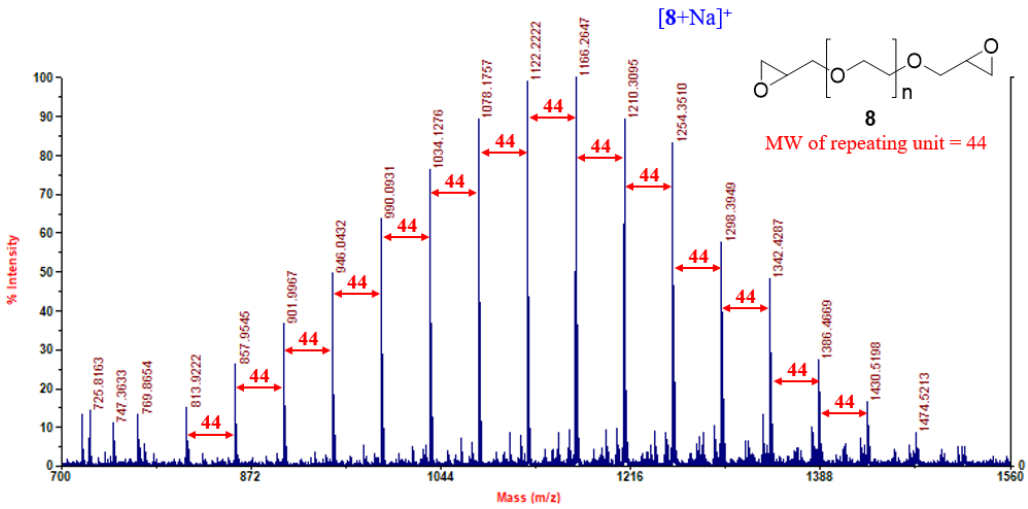

Figure 6. MALDI-ToF mass spectrum of compound **8** (calculated for $C_{52}H_{102}O_{26}Na^+$ 1166.35 [**8**+Na]$^+$, found 1166.26).

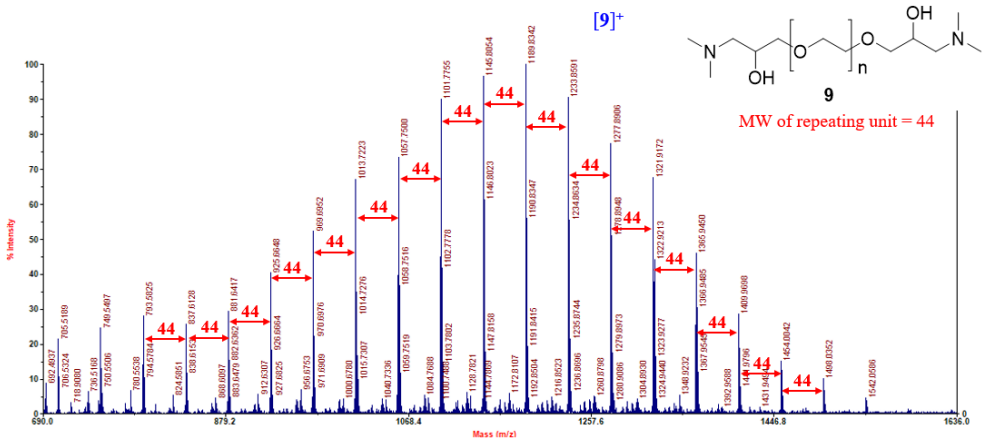

Figure 7. MALDI-ToF mass spectrum of compound **9** (calculated for $C_{56}H_{116}N_2O_{26}^+$ 1233.53 [**9**]$^+$, found 1233.86).

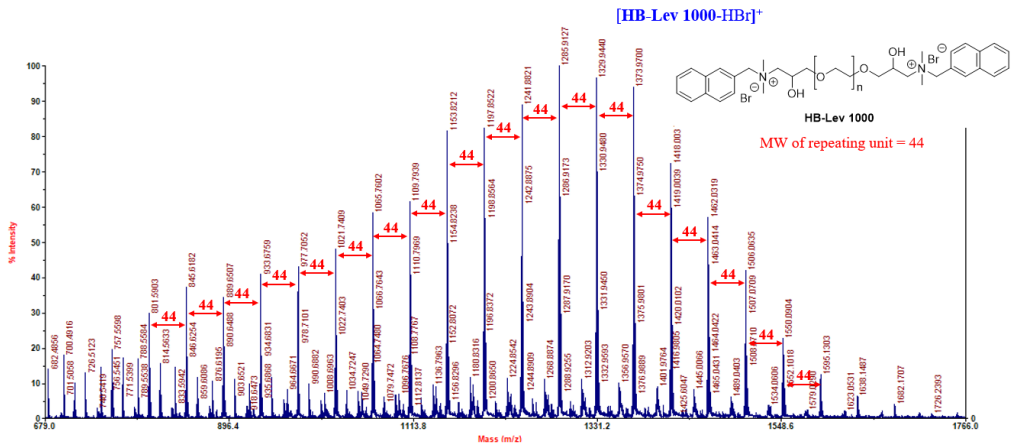

Figure 8. MALDI-ToF mass spectrum of compound **Lev 1000** (calculated for $C_{68}H_{113}BrN_2O_{21}^+$ 1374.55 [**Lev 1000**-HBr]$^+$, found 1373.97).

CURRICULUM VITAE

Minjae Sung

Electronics Processing Research Laboratory
School of Chemical and Biological Engineering
Seoul National University, Seoul 08826, KOREA

Personal Information

Name: Minjae Sung
Date of Birth: May 30, 1990
Place of Birth: Daejeon, Korea
Nationality: Republic of Korea
Sex: Male

Office Address

Institute of Chemical Processes
Seoul National University
1 Gwanak-ro, Gwanak-gu
Seoul 08826, Korea
Tel: +82-2-880-1576
E-mail: tjdjdalswo@snu.ac.kr

EDUCATION

Doctor of Philosophy (August 2015 ~ present)
School of Chemical and Biological Engineering, Seoul National University
Advisor: Prof. Jae Jeong Kim
Thesis: “Additive development for extreme bottom-up filling of Through Silicon Via: from inorganic halide leveler to synthesized additive containing quaternary ammonium and naphthalene ring for single additive system”

Bachelors of Engineering (March 2009 ~ February 2015)
School of Chemical and Biological Engineering, Seoul National University

LIST OF PUBLICATIONS (Minjae Sung)

-International Journal-

[1] M. Sung, H. C. Kim, T. Lim, and J. J. Kim, *Journal of The Electrochemical Society*, **164** (13) D805 (2017).
[2] H. Shen, H. C. Kim, M. Sung, T. Lim, and J. J. Kim, *Journal of Electroanalytical Chemistry*, **816**, 132 (2018).
[3] M. Sung, S.-H. Kim, H.-J. Lee, T. Lim, and J. J. Kim, *Electrochimica Acta*, **295**, 224 (2019).
[4] T. Y. Kim, M. Sung, Y. Yoon, K. H. Lee, S. Choe, and J. J. Kim, *Journal of The Electrochemical Society*, **166** (8) G61 (2019).
[5] M. Sung, A. Lee, T. Y. Kim, Y. Yoon, T. Lim, and J. J. Kim, *Journal of The Electrochemical Society*, **166** (12) D514 (2019)
[6] M. Sung, Y. Yoon, J. Hong, M. J. Kim, and J. J. Kim, *Journal of The Electrochemical Society*, **166** (13) D546 (2019)

-Conference Proceedings-

(International)
[1] M. Sung, Y. S. Ham, Y. Yoon, T. Lim, and J. J. Kim, Grain Size-Controlled Filling of Through Silicon Via (TSV), 68th ISE annual meeting (2017)

(domestic)
[1] 성민재, 김회철, 전영근, 이명현, 김재정, Effect of additives on grain growth in Cu electrodeposition, 한국화학공학회 2016년도 봄 총회 및 학술대회 (2016).
[2] 이명현, 함유석, 성민재, 윤영, 김재정, Influence of polyethylene glycol with NH_4I for bottom-up filling of microvia in two additives composition, 한국화학공학회 2017년도 가을 총회 및 학술대회 (2017)
[3] 성민재, 함유석, 윤영, 임태호, 김재정, Grain size-controlled filling of Through

Silicon Via (TSV), 한국화학공학회 2017년도 가을 총회 및 학술대회 (2017)
[4] 강정규, 성민재, 함유석, 김재정, The study for mechanism of cobalt electrodeposition based on pH control, 한국화학공학회 2018년도 봄 총회 및 학술대회 (2018)
[5] 성민재, 윤영, 이명현, 김재정, 할라이드 이온을 이용한 실리콘 관통 전극의 고속 채움 및 메커니즘에 관한 연구, 2019년도 한국표면공학회 춘계학술대회 (2019)
[6] 이명현, 이윤재, 성민재, 김태영, 윤영, 김영규, 김재정, 마이크로 비아 채움에 평탄제로서 암모늄 기반 유기 첨가제의 작용기에 따른 영향, 2019년도 한국표면공학회 춘계학술대회 (2019)

-Patent-

(International)

[1] 김재정, 성민재, 윤영, 이명현, 함유석, The electrolyte solution containing bromide ion for copper electrodeposition and copper electrodeposition method using the same (PCT/KR2019/01507)
[2] 김재정, 성민재, 윤영, 이명현, 함유석, The electrolyte solution containing bromide ion for copper electrodeposition and copper electrodeposition method using the same (대만/108140313)

(domestic)

[1] 김재정, 성민재, 윤영, 이명현, 함유석, 브롬 이온을 포함한 구리 전해도금용 전해질 용액 및 이를 이용한 구리 전해도금 방법 (10-2018-0135570)
[2] 김재정, 윤영, 성민재, 도금액 내 브롬화물 농도 측정방법 (10-2019-0175585)
[3] 김재정, 김영규, 성민재, 이윤재, 비스-아릴 암모늄 화합물을 포함하는 도금용 평탄제 (10-2020-0065048)

감사의 글

지난 소자 공정 연구실에서의 5년은 흘러가듯 살아온 제 삶에 있어 많은 것을 깨닫게 해준 감사한 기간이었습니다. 사실 처음 지도 교수님이신 김재정 교수님께 연락을 드린 것은 실험 한번 제대로 안 해보고 졸업하는 것이 아쉬웠을 뿐, 당시에는 박사 학위에 대한 욕심은 물론 특별한 목표 의식 없이 얼른 취업하고 싶은 마음이었습니다. 하지만 지도 교수님의 말씀을 들으며, 그리고 대학원에서 꿈을 가지고 공부 중인 선배들의 모습을 보며 그동안의 모습에 반성하게 되었고, 앞으로 제가 살아가는 데에 있어 중요한 것이 무엇인지 생각해보게 되었습니다. 그 결과 사회에 나가기에는 아직 부족하다는 생각이 들었고, 새로운 마음가짐으로 대학원 생활을 시작하게 되었습니다. 처음에는 불성실했던 학부 생활로 인해 불규칙한 생활에 길들여져 있었고, 기초 지식은 부족했습니다. 하지만 교수님의 지도아래 스스로 관리하는 법을 익힐 수 있었고, 교수님의 가르침과 연구실 동료들의 도움을 통해 지식을 쌓고, 실험 계획을 세우며, 더 나아가 논문을 작성하는 방법에 이르기까지 박사가 되기 위해 필요한 많은 것들을 배울 수 있었습니다. 그리고 이제, 끝나지 않을 것만 같았던 대학원 생활은 너무나 빠르게 지나 어느 덧 졸업을 앞두고 있습니다. 이러한 과정 속에서 스트레스 한번 받지 않고 즐겁게 졸업까지 달려올 수 있었던 것은 제 주변에 의지할 수 있는 좋은 사람들이 많았기 때문이라고 생각합니다. 이제는 연구 뿐만 아니라 다방면에 걸쳐 인생의 스승이신 김재정 교수님, 언제나 저를 믿고 지지하며, 버팀목이 되어주신 가족들, 항상 위로와 힘이 되어주고, 이제는 함께 미래를 그려나갈 서연이, 항상 웃으면서 있는 그대로의 나를 받아들이고, 편안한 마음으로 즐길 수 있게 해준 친구들, 그리고 가장 많은 시간을 함께하며 배움과 기쁨을 공유한 연구실 동료들까지. 자칫하면 지치고 힘들 수 있었던 대학원 생활을 이 분들과 함께 였기에 즐거움으로 가득 채울 수 있었습니다. 부족했던 제가 이렇게 박사 학위를 받을 수 있는 것은 이 많은 분들의 도움 덕분이라 생각하며 이렇게 짧게나마 진심을 담아 감사의 인사를 드립니다. 감사합니다.

2020년 8월

성 민 재